On the Synthesis and Multifunctional Properties of some Nanocrystalline Spinel Ferrites and Magnetic Nanocomposites

Thesis submitted to

Cochin University of Science and Technology

in partial fulfillment of the requirements

for the award of the degree of

Doctor of Philosophy

by

Veena Gopalan E

Department of Physics
Cochin University of Science & Technology
Cochin- 682 022, India.

June 2009

**On the Synthesis and Multifunctional Properties
of some NanocrystallineSpinel Ferrites and
Magnetic Nanocomposites**

Ph.D. Thesis

Author

Veena Gopalan E
Parayil House
Cherai P.O., Cherai
Ernakulam Dist.
Kerala, India
Pin: 683514
e-mail: veenasreejith@gmail.com

Supervising Guide

Prof. M. R. Anantharaman
Head of the Department
Department of Physics
Cochin University of Science & Technology
Cochin- 682 022, India.
e-mail: mraiyer@gmail.com

June 2009

Cover Page Illustration

Front cover: Strongly Acidic Cation Exchange Resin (Gel type)
Back cover: Working Room Temperature Magnetic Refrigerator

Prof. M R Anantharaman

Department of Physics

Cochin University of Science and Technology

Cochin – 682 022 India

CERTIFICATE

Certified that the work presented in this thesis entitled "**On the Synthesis and Multifunctional Properties of some Nanocrystalline Spinel Ferrites and Magnetic Nanocomposites**" is based on the bonafide research work done by **Mrs. Veena Gopalan E** under my guidance, at the Magnetics Laboratory, Department of Physics, Cochin University of Science and Technology, Cochin – 22, and has not been included in any other thesis submitted previously for the award of any degree.

Prof. M. R. Anantharaman

(Supervising Guide)

Cochin-22

12-06-2009

Ph.No: +91484-2577404 Extn. 30 (Off)

E mail: mra@cusat.ac.in mraiyer@yahoo.com

Declaration

I hereby declare that the work presented in this thesis entitled **"On the Synthesis and Multifunctional Properties of some Nanocrystalline Spinel Ferrites and Magnetic Nanocomposites"** is based on the original research work carried out by me under the guidance and supervision of Prof. M. R. Anantharaman, Head, Department of Physics, Cochin University of Science and Technology, Cochin-22 and no part of the work reported in this thesis has been presented for the award of any other degree from any other institution.

Cochin-22
12-06-2009

Veena Gopalan E

Acknowledgements

With a deep sense of gratitude and profound thankfulness, I express my gratitude towards my supervising guide and Head of the Department of Physics, Prof. M. R. Anantharaman for all the support and persistent encouragement extended to me through out my research period. I am always grateful for him for his competent advice and sustained guidance without which the successful completion of this work would not have been possible. It was really a blessing for me to get to know him and work with him.

I wish to acknowledge all former Heads of the Department, Dr. M. Sabir, Dr. K.P Vijayakumar, Dr. V. C. Kuriakose, Dr. Ramesh Babu. T and Dr. Godfrey Louis for providing the laboratory and library facilities during my research program.

My sincere thanks to all the faculty members of the Department of Physics, Cochin University of Science and Technology for the help and support they have provided for the completion of this research work. I thank all the non-teaching staff of the Department of Physics who helped me in various ways.

I am grateful to the faculty and scientists in various institutions around the world, particularly, Dr. Imad-al-Omari and Dr. George of Sultan Qaboos University Muscat, Dr. P A Joy of National Chemical Laboratory Pune, Dr. D Sakthi Kumar and Dr. Yasuhiko Yoshida of Toyo University, Japan, Dr. K. G Suresh of I.I.T, Mumbai and Dr. Narayanan of Indian Rare Earths, Eloor, for helping me at various stages of my work. I thank the scientists at STIC, CUSAT for their technical help.

Magnetics Laboratory was a great place to work in. I am deeply thankful to its past and present members for creating the cordial atmosphere and for their support and help, without which it would have been difficult for me to complete my project. I remember with gratitude the names of Dr. K A Malini and Dr. Asha Mary John for their expertise advice and affection showered on me. I remember Dr E.M Muhammed, Dr. C. Joseph Mathai, Dr. Solomon, Dr. S. Saravanan, Dr. Santhosh D. Shenoy, Dr. Sajeev U S, Dr. Swapna S Nair, Dr. Mathew George and Dr. Prema K H with deep gratitude and affection. I would always cherish the memories with Mr. E. M. A. Jamal, Mr. Sanoj M. A., Miss. Vinayasree S., Mr. Sagar S., Mr. Hysen Thomas, Mr. Tom Thomas, Mr. Vasudevan Nampoothiri, Anjali C. P. and the neophyte Ram Kumar.

Special love and thanks to my dears Senoy, Narayanan, Vijutha, Reena and Geetha for they have been there with me in every situation I faced, just like my family members.

I thank with love and gratitude all my fellow research scholars of Department of Physics for the affection and support. My thanks are also due to Suni. V and Dally Davis, Department of Chemistry who helped me a lot during initial stages of my research.

I thank, Cochin University of Science and Technology for the university research fellowship. I am thankful to the all the help received from the faculties of Vimala College, Thrissur for making Ph.D work to a completion.

Words are insufficient to express my acknowledgements for my ever loving parents, for they have been the inspiring force behind me. I am deeply indebted to my compassionate in-laws who provided me with all the support for such a long time My thanks are also due to my bother Kannan Chettan, sister Parus, brother in law Sreeraj and all other cousins and relatives in the family for their love and affection towards me. I will never forget the help received from Remani chechi for assisting me in managing my home along with my research.

I will not thank my *Kannettan*, but owe him my life   for all his love, support and inspiration poured on me through out these working years. My sweet little   Appu is always there to make me feel jovial. To them I dedicate this thesis.

Above all, I thank God Almighty for offering me with all these wonders...

Veena Gopalan E

Dedicated to my Dearest Kannettan & Appus...

Preface

Nanotechnology is an all inclusive one and is increasingly playing a lead role not only in material science, but also in areas like biology, information technology, photonics and biotechnology. Nanoscience is growing at a faster pace than anticipated and rapid strides are made in this regime. With the advent of nanoscience and nanotechnology, new devices are emerging and with the help of nanotechnology, the obsolete are replaced. Quantum Mechanics played a very seminal role in understanding the fundamental properties at the nanolevel and so physicists naturally take the lead in exploiting this brand new area of science for the benefit of human kind.

From time immemorial, magnetism and magnetic materials has been playing a significant role in making life more humane and helping scientists to device new gadgets for various applications. The domain of magnetism or more precisely nanomagnetic materials is bound to play a profound role in helping devise newer applications envisaged using nanotechnology. Its common knowledge that together with magnetism and nanotechnology, devices based on giant magneto resistance will soon see the light of the day. With world wide concern for environment, scientists have been scouting for alternatives for gas based refrigeration and in this journey, they have found an answer in nanocrystalline magnetic materials as potential magnetic refrigerants which are eco-friendly and viable.

Ferrimagnetic materials based on ferrites have been contributing their might in various applications like radiofrequency circuits, high quality filters, rod antennas, transformer cores, read/write heads for high speed digital tapes and other devices. The research on ferrites and materials based on ferrites can be traced to the preliminary research carried out by Snoek, Smith and Wijin, Cullity,

Chikazumi and others. These materials are revisited again by physicists and chemists because quantum size effects of these materials are pronounced at nanodimensions. At the nanosize, these materials exhibit superlative magnetic and electrical properties and are now a subject of intense research especially to delve into the fundamental aspects like quantum mechanical effects at the nanosize. With the emergence of nanotechnology there is renewed interest in ferrites since many of the useful properties of these materials can be modified suitably for applications in magnetic storage, as precursors for ferrofluids, as contrast enhancing agents in Magnetic Resonance Imaging (MRI) , as magnetic refrigerant materials in magnetic refrigeration technology and also as magnetically guided drug delivery agents.

The ease with which the structural and magnetic properties of these materials can be tailored has made ferrites an ideal candidate for studying the size effects at the nanoregime from a fundamental perspective. As far as applications are concerned, the properties can be tailored by a judicious choice of cations present in the ferrite materials. Ferrites are also important for magnetic refrigeration applications because at nanodimensions, they exhibit phenomena like superparamagnetism, spin glass behaviour and blocking. Though most of the electrical and magnetic properties of these materials are well understood at the micron regime, there are grey areas where lot of research needs to be carried out. For example, the electrical properties of nanoferrites are not well understood and very little literature exists on the mechanism of conduction. Manganese zinc ferrites belong to the class of mixed spinel ferrites. The equilibrium distribution of cations in the bulk structure is influenced by a number of factors namely ionic radii, ionic charge, lattice energy, octahedral site preference energy and crystal field stabilization energy. In the coarser regime, Zn^{2+} has a strong preference for tetrahedral sites while Ni^{2+} exhibits a strong octahedral preference in spinel ferrites. Cations like Mn^{2+} /Mn^{3+} are found to be influencing the magnetic,

structural and electrical properties considerably. In the nanoregime, in the case of spinel ferrites, there are distinct deviations in magnetic properties with respect to their bulk counterparts. However the role of cations *vis a vis* their occupancy of octahedral sites instead of tetrahedral sites is still not clear as regard their influence in deciding the overall magnetic properties of these materials in the nanoregime. It is in this context that a study of nanosized $MnFe_2O_4$ with varying concentration of zinc assumes significance. Ferrites belonging to the series, $Mn_{1-x}Zn_xFe_2O_4$ (for x=0, 0.1, 0.2 ...1) provide an ideal platform to check various hypotheses. Cobalt ferrite distinguishes itself among ferrites on account of its wide ranging applications in magnetic recording devices, magneto-optical devices, sensors based on magnetostrictive property etc. They exhibit interesting magnetic properties with their major contribution coming from the magnetocrystalline anisotropy of cobalt.

Magnetic metal nanoparticles are also a subject of intense research because of their potential applications. In this context, iron and nickel needs special mention. However, these materials in the nanoregime possesses large surface area and prone to oxidation. Hence passivation of these nanoparticles is a prerequisite and nanocomposites based on these nanosized metal nanoparticles are sought after for various applications in catalysis, bio sensors, spin polarized devices, carriers for drug delivery etc. Template assisted preparation of metal nanoparticles are a viable alternative. Inexpensive methods which can be carried out in ordinary laboratories are often adapted to. Thus the synthesis of nanocrystalline spinel ferrites and metal polymer nanocomposites and the evaluation of their multifunctional properties are significant both from a fundamental as well as from an applied perspective.

This thesis lays importance in the preparation and characterization of a few selected representatives of the ferrite family in the nanoregime. The

candidates being manganese zinc ferrite and cobalt ferrite prepared by co-precipitation and sol-gel combustion techniques respectively. The thesis not only stresses importance on the preparation techniques and optimization of the reaction conditions, but emphasizes in investigating the various properties namely structural, magnetic and electrical. Passivated nickel nanocomposites are synthesized using polystyrene beads and adopting a novel route of ion exchange reduction. The structural and magnetic properties of these magnetic nanocomposites are correlated. The magnetocaloric effect (MCE) exhibited by these materials are also investigated with a view to finding out the potential of these materials as magnetic refrigerants. Calculations using numerical methods are employed to evaluate the entropy change on selected samples. The results are reported in the thesis.

This proposed thesis is entitled **"On the Synthesis and Multifunctional Properties of some Nanocrystalline Spinel Ferrites and Magnetic Nanocomposites"** and consists of eight chapters.

The significance of nanomagnetic materials and their applications in nanotechnology are briefly introduced in *Chapter 1.* The general structural, magnetic and electrical properties of the ferrites in the bulk and nanoregime are briefly discussed. A comprehensive picture of different types of nanocomposite, their synthesis procedure, properties and applications are also included in this chapter. Finally the motivation and objectives of the work are outlined.

Chapter 2 deals with analytical techniques like X-ray diffraction and transmission electron microscopy (TEM), used for the structural characterization of the magnetic nanoparticles. Energy dispersive spectrum (EDS) and inductively coupled plasma analysis (ICP), used for verifying the stochiometry are also provided in the chapter. The details of magnetic measurements and

magnetocaloric measurements are also mentioned. Theoretical and experimental aspects of dielectric and electrical measurements are also explained in this chapter.

Chapter 3 essentially discusses the synthesis, structural and magnetic characteristics of the mixed ferrite series $Mn_{1-x}Zn_xFe_2O_4$ (for x=0, 0.1, 0.2...1). Emphasis is given to the impact of zinc substitution on these characteristics.

A detailed analysis of the electrical properties of manganese zinc mixed ferrites as a function of zinc substitution is given is *Chapter 4*. The various conduction mechanisms for the different compositions are also suggested.

Chapter 5 presents the synthesis and characterization of cobalt ferrite nanoparticles. The particulars of structural magnetic and electrical characteristics are analysed and correlated.

The novel technique of synthesis of metal polystyrene nanocomposites (Nickel-polystyrene and iron-polystyrene nanocomposites) forms the main theme of *Chapter 6.* The effect of cycling (the loading reduction cycle involved in the synthesis) in enhancing the structural and magnetic characteristics is also depicted in this part of the thesis.

In *Chapter 7,* the indirect technique of measuring magnetocaloric effect (MCE) is employed to measure the magnetocaloric properties of cobalt ferrite nanoparticles and Nickel polystyrene nanocomposites. The importance of the measurements is highlighted.

Chapter 8 is the concluding chapter of the thesis and in this chapter the salient observations and the inferences drawn out of these investigations are presented in a nutshell. The scope of further work is also proposed here.

Contents

Chapter 7

Magnetocaloric Effect in Cobalt Ferrite

Nanoparticles and Nickel Nanocomposites:

Chapter 8

Chapter 1

Introduction

Material Science encompasses various disciplines, namely, physics, chemistry and engineering and is truly interdisciplinary in nature. The evolution of material science is always an indicator to man's progress and his urge to improve upon the existing and replace the obsolete with newer and novel materials often results in newer materials and innovations. The emergence of nanoscience and nanotechnology as a leading technology of the 21st century has only accelerated the growth of material science. Today nanoscience and nanotechnology has become synonymous with material technology. Magnetism and magnetic materials has been playing a seminal role in ones life. The magnetic industry is all set to surpass the semiconductor industry with the proliferation of new gadgets based on magnetic materials and new innovations in the area of nanomagnetism. The realm of modern day magnetism and magnetic materials is always a subject of intense research. Newer devices based on magnetism are hitting the markets. For example, we have spintronic devices, giant magnetoresistance based (GMR) sensors, magnetic random access memories and other novel gadgets based on nanomagnetism. So it is only natural that magnetism and magnetic materials at the nanoregime attracts the attention of researchers world wide.

Nanoscience is of central importance in the science world and is now pervasive in technology, popularly known as Nanotechnology. Nanomagnetism is already central to data storage, sensor and device technologies but is increasingly being used in the life sciences and medicine. The significance of nanomagnetic materials and its applications in nanotechnology are briefly introduced in this part of the thesis. The different physical and chemical techniques for the synthesis of ferrite nanoparticles are briefly explained. The general properties of the ferrites at the nanoregime are discussed along with their applications. A comprehensive picture of different types of nanocomposites, properties and applications are also included in this chapter. The principle behind magnetic refrigeration and magnetocaloric effect (MCE) is also incorporated with necessary theory. Finally the motivation and objectives of the work are outlined.

1.1 Nanotechnology and Nanoscience

Nanotechnology, termed as the technology of the century and deals with the design, fabrication and application of nanostructures or nanomaterials [1-3]. It also embraces the fundamental understanding of the relationship between the different physical and chemical properties and material dimensions. The technology has a wide range of applications from nanoscale electronics and optics to nanobiological systems and nanomedicine [4-6]. Basically it is a multidisciplinary subject which essentially requires contributions from physicists, chemists, material scientists, engineers, molecular biologists, pharmacologists for the proper development.

Nanoscience and nanotechnology mainly covers the length scale of 1-100nm. The transition from microparticles to nanoparticles can lead to a number of changes in the physical properties. At the nanometer dimensions, a large fraction of the atoms are at or near the surface resulting in a large surface to volume ratio. The increase in the surface to volume ratio leads to increasing dominance of the behaviour of atoms on the surface of the particle over that of

those in the interior of the particle. This affects the properties of the particles in isolation and its interaction with other particles. This is where quantum size effects starts playing its role [7, 8]. At nanolevel, materials exhibit superlative physico-chemical properties when compared to their nanosized counterparts. With the emergence of nanotechnology in the horizon of research, magnetism at the nanoscale is being probed deeply from a fundamental perspective.

The applications of magnetic spins in solid-state materials have enabled significant advances in current informational and biological technologies including information storage, magnetic sensors, bio separation, and drug delivery [9-12]. Although micron-sized magnetic materials have been utilized for such purposes, researchers are now pursuing further miniaturization of magnetic devices while possessing superior magnetic properties. Magnetic nanoparticles are emerging as a potential candidate for fulfilling such expectations. Being different from their bulk counterparts, they exhibit unique nanoscale magnetic behaviors which are highly dependent on morphological parameters such as size and shape. Such size and shape effects in nanoparticles enable us the possibility to control their properties (e.g. coercivity, H_c and susceptibility, χ) as we desire by synthetically tuning their morphological parameters.

General concepts in magnetism and theory of magnetism in fine particles are briefly discussed in this introduction. The properties of specific nanomaterials: ferrites and nanocomposites are depicted with giving importance to the synthesis techniques and applications. Magnetocaloric effect as the basis of magnetic refrigeration is explained with adequate theory and equations. The objectives undertaken are emphasized along with the motivation.

1.2 Magnetism

1.2.1 Origin of Magnetism

A magnetic field is a force field similar to gravitational and electrical fields that is surrounding a source of potential; there is a contoured sphere of

influence or field. The origin of the magnetic potential is known as magnetic dipoles. Magnetism essentially results from two electronic motion associated with the atom; the orbital motion of the electron and the spin motion of the electron. For macropscopic purposes these tiny currents due to these motions can be treated as magnetic dipoles. Ordinarily they cancel each other out because of the random orientation of the atoms. But when a magnetic field is applied, a net alignment of these magnetic dipoles occurs and the medium becomes magnetically polarized. [13-15]

The strength of magnetic field which magnetises the material is measured by magnetic field (H) The magnetic moment per unit volume of the magnetised material is measured by magnetisation M. B is termed as the magnetic induction or magnetic flux density inside the magnetised material.

The magnetisation M is the sum of the magnetic moments m_i per unit volume

$$M = \sum_{volume} m_i \qquad (1.1)$$

The magnetic properties of magnetic materials are characterised not only by the magnitude and sign of M, but also the way in which M varies with H. The ratio of these two quantities is called magnetic susceptibility.

$$\chi = \frac{M}{H} \qquad (1.2)$$

The magnetisation M of a material is defined by the relation

$$B = \mu_0 (H + M) = \mu_r \mu_0 H = \mu H \qquad (1.3)$$

where $\mu_0 = 4\pi \times 10^{-7}\,\mathrm{Hm^{-1}}$ is the permeability of free space and B and H are measured in Tesla (T) and $\mathrm{Am^{-1}}$ respectively. μ_r is termed as the relative permeability of the material.

Hence from the relations 1.2-1.3, it can be shown that

$$\mu = \mu_0 (1 + \chi) \qquad (1.4)$$

The value of χ and μ_r characterises the magnetic properties of a material

4

Typical curves of M vs H called magnetisation curves are characterised by phenomena like saturation magnetisation and hysteresis (figure1.1). At higher values of H, the magnetisation M becomes constant at its saturation value of M_s. after saturation, a decrease in H to zero does not reduce M to zero which is termed as hysteresis. M_r is the remananent magnetisation and H_c is the coercive field or coercivity of the material.
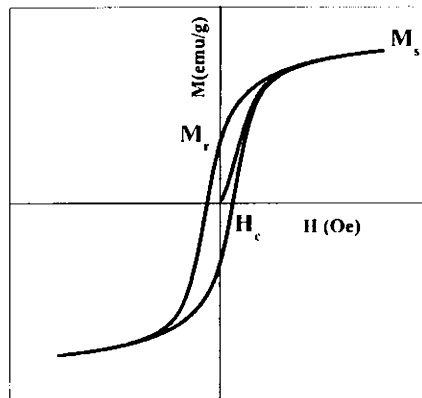
Figure 1.1 Typical Hysteresis Curve

1.2.2 Types of Magnetism

All materials are affected by a magnetic field. Based on the nature of interaction with the magnetic field, materials can be classified mainly into following five types [13- 15]

    a. Diamagnetism

    b. Paramagnetism

    c. Ferromagnetism

    d. Antiferromagnetism

    e. Ferrimagnetism

Materials in the first two groups are those that exhibit no collective magnetic interactions and are not magnetically ordered. Materials in the last three groups exhibit long range magnetic order below a certain critical temperature.

Ferromagnetic and ferrimagnetic materials are usually what we consider as being magnetic. The remaining three are so weakly magnetic that they are usually thought of as "nonmagnetic".

a. Diamagnetism

Diamagnetism is a fundamental property of all matter although it is usually very weak. It is due to the non-cooperative behaviour of orbiting electrons when exposed to an applied magnetic field .Diamagnetic substances are composed of atoms which have no net magnetic moments *i.e.* all orbital shells are filled and there are no unpaired electrons. However, when exposed to a field, a negative magnetisation is produced and thus the susceptibility is negative (figure 1.2).
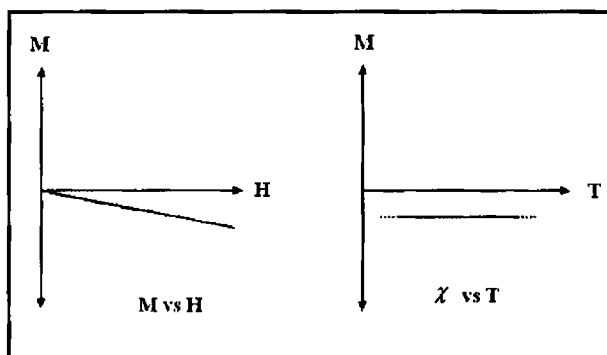
Figure 1.2 Variation of M vs H and χ vs T in a diamagnetic material

The diamagnetism of atoms, ions and molecules can be modeled as if the orbits of the electron were current loops. The induced moment is proportional to the current times the area of the loop. Current will depend upon the passage of electron times the charge on the electron e and on the frequency of the orbital motion, which also depends on the charge e. Thus susceptibility is directly proportional to $Ze^2 <r^2>$ where r is the orbital radius and Z, the atomic number

By Langevin's theory of diamagnetism the susceptibility is predicted as

$$\chi = -\frac{NZe^2}{mc^2}\langle r^2 \rangle \qquad (1.5)$$

where N is the number of atoms per unit volume, m the electron mass, and c is the speed of light. The other characteristic behaviour of diamagnetic material is that the susceptibility is temperature independent figure (1.2).

b. Paramagnetism

In this class of materials, some of the atoms or ions in the material have a non-zero magnetic moment due to unpaired electrons in partially filled orbitals. Then an applied field modifies the direction of the moments and an induced magnetisation parallel to the field appears.
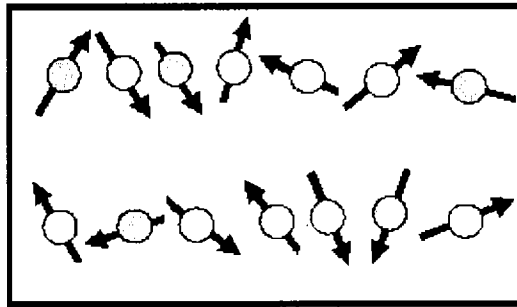
Figure 1.3 Partial alignments of atomic magnets in a paramagnet

However the individual magnetic moments do not interact magnetically and like diamagnetism the magnetisation is zero when the field is removed. In the presence of filed, there is now a partial alignment of the atomic magnetic moments (figure 1.3) in the direction of the field resulting in a net positive magnetisation and positive susceptibility (figure 1.4).
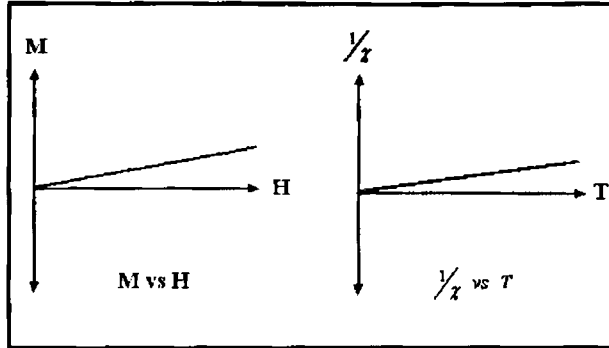
Figure 1.4 Variation of *M vs H* and χ *vs T* in a paramagnetic material

In addition the efficiency of the field in aligning the moments is opposed by the randomizing effects of temperature. This results in a temperature dependent susceptibility (figure 1.4) which is given as the Curie's law developed on the basis of Langevin's theory of paramagnetism.

At normal temperature and in moderate fields, the paramagnetic susceptibility is small, but larger than the diamagnetic contribution. Langevin theory of paramagnetism explains the importance of temperature in governing the magnetic properties.

By Classical Langevin model of paramagnetism, the total magnetic moment is given by

$$M = NmL(x) \tag{1.6}$$

$$L(x) = coth(x) - x^{-1} \tag{1.7}$$

$$x = \frac{mH}{k_B T} \tag{1.8}$$

where *N* is the number of atoms each with magnetic moment *m*, *H* the applied magnetic field k_B the Boltzmanns constant, *T* is the temperature in degree Kelvin and *L(x)* is called the Langevin function.

At small x,

$$L(x) \cong \frac{x}{3} \tag{1.9}$$

Hence the magnetisation

8

$$M \cong \frac{N m^2 H}{3 k_B T} \qquad (1.10)$$

This results in the inverse temperature dependence of the susceptibility known as the Curies law (figure 1.4) given by

$$\frac{M}{H} = \frac{C}{T} \qquad (1.11)$$

Where C is called the Curie's constant given by

$$C = \frac{Nm^2}{3k_B} \qquad (1.12)$$

This equation applies when $k_B T \gg mH$.

At large x, $L(x) \rightarrow 1$, and all moments are aligned. This is known as saturation magnetisation, $M_s = Nm$

Considering the quantum effects in magnetism, the total magnetic moment is written as

$$M = NgJ\mu_B B_J(x) \qquad (1.13)$$

where

$$B_J(x) = \frac{2J+1}{2J} \coth\left(\frac{(2J+1)x}{2J}\right) - \frac{1}{2J} \coth\left(\frac{x}{2J}\right) \qquad (1.14)$$

and

$$x = \frac{gJ\mu_B H}{k_B T} \qquad (1.15)$$

The function $B_J(x)$ is called the Brillouin function .The Brillouin function has two limits with J . When $J = \frac{1}{2}$,

$$M = Nm\,tanh\,x \qquad (1.16)$$

When $J \rightarrow \infty$, the Brillouin function becomes the Langevin function.

The theory of paramagnetism implies that magnetisation data for a paramagnet fall on a universal curve if plotted as a function of H/T. The temperature dependence of χ in a paramagnetic material gives a straight line with a slope. In real materials deviations from Curie's law are often observed, in

particular at low temperature. One of the most usual contributions to these deviations is the Van Vleck's paramagnetisam. In metals, conduction electrons can also give rise to a paramagnetic behaviour called Pauli paramagnetism with a susceptibility that is virtually temperature independent

c. Ferromagnetism

The atomic magnetic moments in magnetic materials like iron, nickel, cobalt etc. exhibit very strong interactions. The interactions are produced by electronic exchange forces and result in a parallel or antiparallel alignment of atomic moments. The positive exchange interactions in favour a parallel arrangement of magnetic moments in neighboring atoms. On account of the magnetic interactions, susceptibility instead of becoming infinite at 0K as in a paramagnet becomes infinite at a characteristic temperature called the Curie temperature T_C. Below this temperature the interactions overcome thermal agitation and a spontaneous magnetisation appears in the presence of an applied magnetic filed. The spontaneous magnetisation reaches its maximum value M_0 at 0K corresponding to parallelism of all the individual moments (figure 1.5).

$\longrightarrow$ **H**
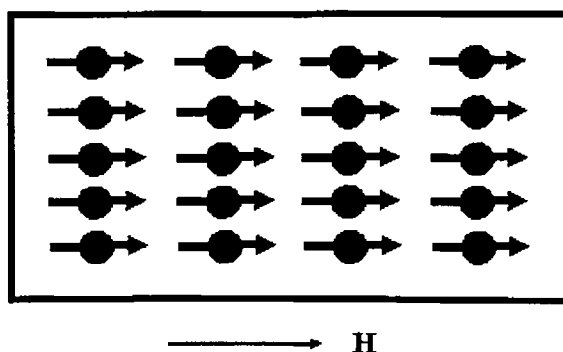
Figure 1.5 Alignment of atomic magnets in a ferromagnet under an applied field H

Thus the ferromagnetic materials are found to display a modified temperature dependence of χ which is described by the equation

$$\chi = \frac{C}{T - \theta} \qquad (1.17)$$

where θ is a critical temperature that can be either positive or negative. This modification is called Curie Weiss Law. In the case of ferromagnetism this ordering temperature is called the Curie temperature (figure 1.6). This law was developed on the basis of Weiss Molecular field theory based on the magnetic interactions between atomic moments.
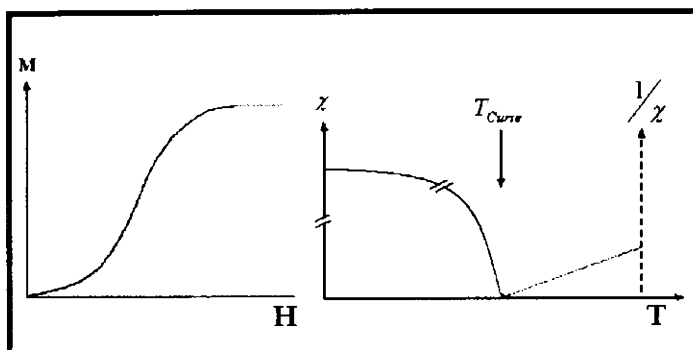
Figure 1.6 Variation of *M vs H* and χ *vs T* in a ferromagnetic material

By Weiss molecular field theory, a molecular field acts in a ferromagnetic material below its curie temperature as well as in the paramagnetic phase above T_c and that this molecular field is strong enough to magnetise the substance even in the absence of an external applied field. To model this interaction he assumed that the net interaction on a given magnetic moment is an effective magnetic field, a mean field due to all other moments. However the temperature dependence of χ yield a unrealistic large values for the molecular field and hence the theory was found to have some serious problems. However more accurate theories consider the only nearest neighbour interactions for the magnetic atomic moments and the

interactions are not magnetic, but rather due to what is called exchange interaction, which is quantum mechanical in origin.

The true physical origin of the exchange coupling was elucidated by Heisenberg. Quantum mechanics provides for an exchange interaction between two atoms based on symmetry, the Pauli's exclusion principle and the coulombic interaction. Heisenberg showed the exchange interaction in a two electron system lead to an exchange energy given by

$$E_{ex} = -2J_{ex}S_i.S_j \qquad (1.18)$$

between neighbouring spins, S_i and S_j, J_{ex} is called the exchange integral. If J_{ex} is positive, the lower energy configuration is that of lower energy and hence parallel magnetic moments as required for ferromagnetism. If J_{ex} is negative, antiparallel configuration results.

Two theories of magnetism were used to explain the ferromagnetism in metals: (i) localized moment theory (ii) band theory in the localized moment theory, the valence electrons are attached to the atoms and cannot move about the crystal. The valence electrons contribute a magnetic moment which is localized at the atom. The localized moment theory accounts for the variation of spontaneous magnetisation with temperature in the ferromagnetic phase and explains the Curie Weiss behaviour above the Curie temperature. In the collective electron model or band theory, the electrons responsible for magnetic effects are ionized from the atoms and are able to move through the crystal. Band theory explains the non integer values of the magnetic moment per atom that are observed in metallic ferromagnets. In real situations neither model can be considered perfectly correct, but rather a good approximation. By far the most successful method currently available for calculating the magnetic properties of solids is density functional theory which includes all the interactions between all the electrons. By this theory it is assumed that the electrons choose the arrangement which will give them the lowest possible total energy. However Density Functional Theory (DFT)

calculations are both intensive and difficult as the exact form of the exchange and correlation part of the interelectronic interaction energy is not known.

d. Antiferromagnetism

In an antiferromagnet, exchange coupling between neighbouring moments that causes the moments to align in an antiparallel fashion: the exact opposite of a ferromagnet (figure 1.7). In terms of Heisenberg Hamiltonian interaction, the exchange integral J_{ex} is negative. This antiparallel alignment causes the system to have small positive susceptibility, because an applied field tends to align the spins and this induced alignment is larger than the diamagnetism of the electron orbitals. Similar to ferromagnetic materials, the exchange energy can be defeated at high temperature and then the system becomes paramagnet.
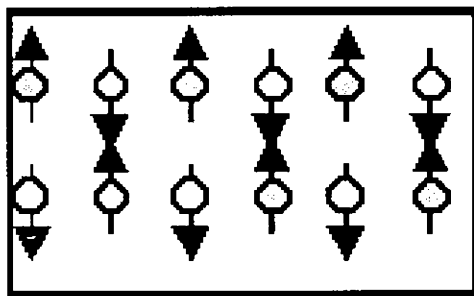
Figure 1.7 Alignment of atomic magnets in an antiferromagnet under an applied field

The thermal variation of the reciprocal susceptibility of an antiferromagnetic material measured exhibit a minimum at a critical temperature termed as Neel temperature (figure 1.8) .When temperature is reduced down to below T_N, the susceptibility decreases as the thermal agitation which works against the antiferromagnetic order of the moment decreases. At higher temperatures the thermal agitation overcomes interaction effects and one observes again a thermal variation of the susceptibility similar to that of a paramagnet. For temperatures greater than T_N, the susceptibility of antiferromagnetic substance

follows Curie –Weiss law with a negative θ. An antiferromagnetic material can be viewed microscopically consisting of two sublattices A and B and an antiparallel interaction occur between these lattices. These equal and opposite interaction compensate each other in nearly zero magnetisation of the antiferromagnetic material. Many antiferromagnetic systems are known, usually ionic compounds such as metallic oxides, sulfides, chlorides etc.
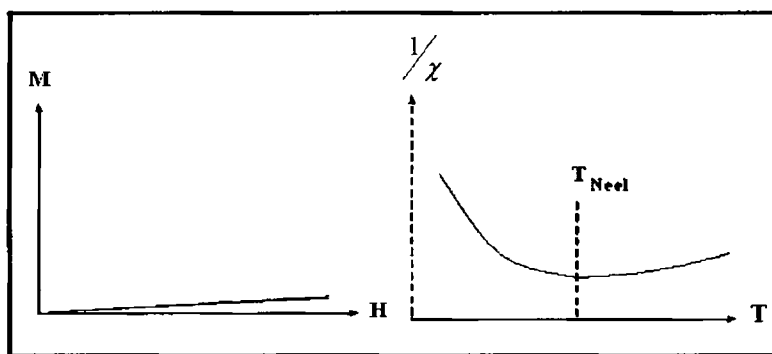
Figure 1.8   Variation of M vs H and $1/\chi$ vs T in a paramagnetic material

e. Ferrimagnetism

Ferrimagnetism characterises a material which microscopically, is antiferromagnetic like, but in which the magnetisation of the two sublattices are not the same. The two sub lattices no longer compensate each other exactly. A finite difference remains to leave a net magnetisation (figure 1.9). This spontaneous magnetisation is defeated by the thermal energy above a critical temperature called the Curie temperature and then the system is paramagnetic. The variation of magnetisation with applied field and susceptibility with temperature is shown in figure (1.10).

14
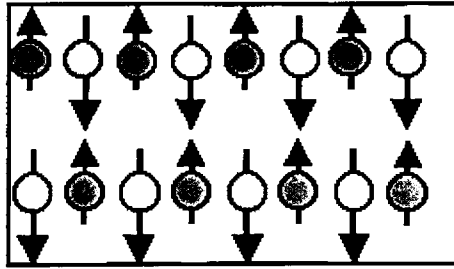
Figure 1.9 Alignment of atomic magnets in a ferrimagnet under an applied field

At high temperatures, Curie Weiss behaviour is seen with χ^{-1} linear with T. Near the Curie temperature, χ^{-1} versus T is curved.

A large number of ferrimagnets are known: ferrites are a major class. Ferrimagnetism in ferrites based on Neel's sublattice model are dealt in detail in the proceeding sections.
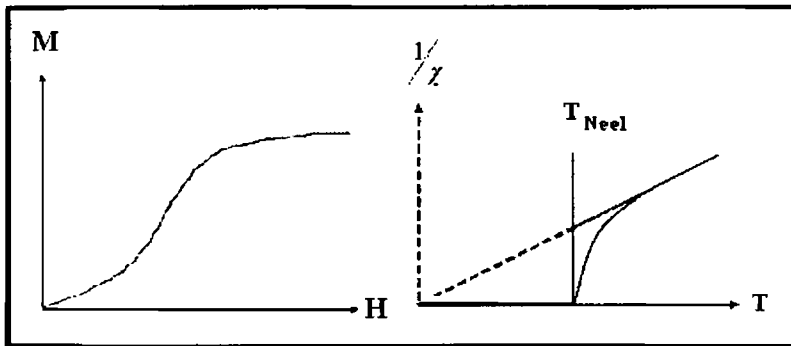
Figure 1.10 Variation of M vs H and $1/\chi$ vs T in a ferrimagnetic material

1.2.3 Magnetic Interactions

The different types of magnetic interactions which allow the magnetic moments in solids to communicate with each other to produce a long range order are descried here[13].

1. Magnetic dipolar interaction

Each magnetic moment of the substance is subjected to a magnetic dipolar interaction with the other moments. The magnetic dipole interactions between two magnetic dipoles separated by a distance r have an energy equivalence given by

$$E = \frac{\mu_0}{4\pi r^3}\left[m_1 \cdot m_2 - \frac{3}{r^2}(m_1 \cdot r)(m_2 \cdot r) \right] \tag{1.19}$$

The dipolar interaction is much weaker than the exchange interaction among near neighbour moments, become dominant only at large distances. The magnetic dipolar interactions are found to be too weak to account for the ordering of most magnetic materials with higher ordering temperatures.

2. Exchange interactions

Exchange interaction is the main phenomenon governing the long range magnetic order in ferro, antiferro and ferromagnetic materials. It is of quantum mechanical origin and electrostatic in nature. It is very strong, but acts between neighbouring spin moments only and falls off very rapidly with distance. The interaction between two atoms having spins S_i and S_j was shown by Heisenberg as in equation 1.18. The major exchange interactions are direct exchange ,indirect exchange or superexchange, RKKY interaction and double exchange [13].

(a) Direct Exchange

In direct exchange interactions, the interaction between neighbouring magnetic proceeds directly without the help of an intermediatory. Often direct exchange is not found to be an important mechanism in controlling the magnetic properties because there is insufficient direct overlap between the neighbouring

magnetic orbitals. Hence direct interactions are not found to be effective in rare earth metals and transition metals.

(b) Indirect Exchange or Super Exchange interactions in ionic solids

Indirect exchange or superexchange interactions between non neighbouring magnetic ions is mediated by a nonmagnetic ion which is placed in between the magnetic ions in the case of ionic solids. Superexchange interactions involves the oxygen orbitals as well as metal atom (in ferrites) and it is a second order process derived from second order perturbation theory. Superexchange interactions could occur in ferromagnetic materials but less common than the usual antiferromagnetic or ferromagnetic superexchange.

(c) Indirect Exchange in metals-RKKY interactions

In metals, the exchange interactions between magnetic ions can be mediated by the conduction electrons. A localized spin magnetic moment polarizes the conduction electrons and this polarization in turn couples to a neighbouring localized magnetic moment a distance r away. The interaction is called RKKY interaction after Ruderman, Kittel, Kasuya and Yosida. The interaction is long range and has an oscillatory dependence on the separation between the magnetic moments. The resulting interaction can be either ferro or antiferromagnetic depending on the separation between the ions.

(d) Double Exchange Interactions

In some oxides, it is possible to have a ferromagnetic exchange interaction which occurs between the magnetic ions showing a mixed valency. The ferromagnetic alignment is due to the double exchange mechanism. Zener preposed this exchange mechanism to account for the interaction between adjacent ions of parallel spins via a neighbouring oxygen ion. Zener's mechanism of double exchange forms a positive interaction which is contributing factor to the observed ferromagnetic interaction in materials like perovskite manganates like $LaMnO_3$, $LaSrMnO_3$ etc.

(e) Anisotropic Exchange Interactions

It has been found that spin orbit interaction result in exchange interactions in a similar manner to that of the oxygen atom in superexchange. There is an exchange interaction between the excited state of one ion and the ground state of the other ion .The excited state is produced by the spin–orbit interaction in one of the magnetic ions. This is known as anisotropic exchange interaction or also as the DZyaloshinsky-Moriya interaction. The form of interaction is such that it tries to force the spins to be at right angles in a plane so that orientation will ensure that the energy is negative. Its effect is therefore to cant the spins by a small angle. The effect is known as weak ferromagnetism. It is found in α-Fe_2O3, $MnCO_2$ etc.

1.2.4 Magnetic Domains

Weiss first proposed that a ferromagnet contains a number of small regions called domains. Ferromagnetic domains are small regions in ferromagnetic materials within which all the magnetic dipoles are aligned parallel to each other (figure 1.11). When a ferromagnetic material is in its demagnetised state, the magnetisation averages to zero. The process of magnetisation causes all
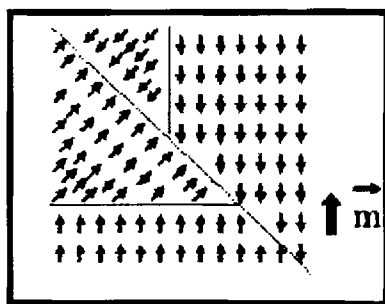

Figure 1.11 Schematic of multidomains in a ferromagnetic material

the domains to orient in the same direction. Domains are separated by domain walls. The formation of domains allows a ferromagnetic materials to minimize its total magnetic energy .The main contribution to the magnetic energy are

18

magnetostatic energy, magnetocrystalline energy and magnetostrictive energy which influence the shape and size of the domains. The magnetisation and hysteresis occurring in a ferromagnetic material can be suitably explained by domain theory [14,16].
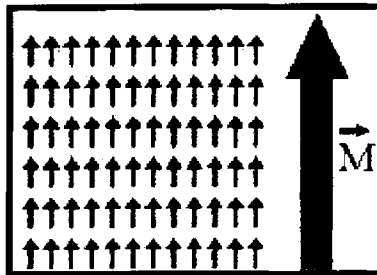
Figure 1.12 Schematic monodomain after the application of the field

In the initial demagnetised state, the domains are arranged that the magnetisation averages to zero. When the field is applied, the domain whose magnetisation is nearest to the field direction starts to grow at the expense of other domains. The growth occurs by domain wall motion is provided by the external magnetic field. Eventually the applied filed is sufficient to eliminate all domain walls from the sample leaving a single domain, with its magnetisation pointing along the easy axis oriented closely to the external magnetic field. Further increase in magnetisation can occur only by rotating the magnetic dipoles from the easy axis of magnetisation into the direction of the applied field. In crystals with large magnetocrystalline anisotropy, large fields can be required to reach saturation magnetisation. So we will now discuss the magnetocrystalline anisotropy associated with magnetic materials.

1.2.5 Magnetic Anisotropy

Magnetic anisotropy generally refers to the dependence of magnetic properties on the direction in which they are measured. The magnitude and type of magnetic anisotropy affect properties such as magnetisation and hysteresis curves

in magnetic materials. The important and common sources of magnetic anisotropy, magnetocrystalline anisotropy, shape anisotropy, surface anisotropy along with induced magnetic anisotropy are discussed here [13].

(a) Magnetocrystalline Anisotropy

Magnetocrystalline anisotropy is the tendency of the magnetisation to align itself along a preferred crystallographic direction. For example, body centered cubic Fe has the (100) direction as its easy axis .In nickel, which is a face centered cubic, the easy is axis is (111). It is observed that the final value of the spontaneous magnetisation is the same, no matter which axis the field is applied along, but the field required to reach that value is distinctly different in each case. The physical origin of magnetocrystalline anisotropy is the spin orbit coupling resulting in orientation of the spins relative to the crystal lattice in a minimum energy direction, the so called easy direction of magnetisation.
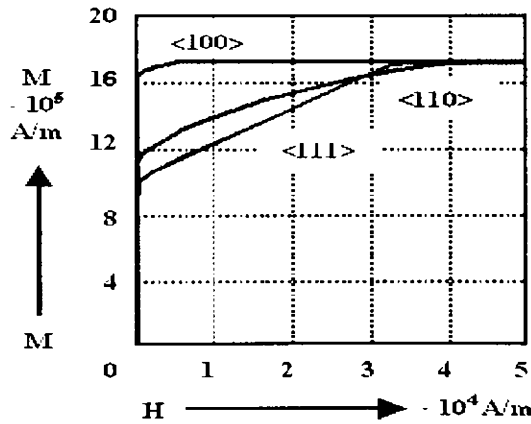

Figure 1.13 Anisotropy of magnetisation in Fe

Aligning the spins in any other direction leads to an increase in energy, the anisotropy energy E_k. For a cubic crystal E_k is related to two anisotropy constants K_1 and K_2 by

$$E_k = K_1 \left(\alpha_1^2 \alpha_2^2 + \alpha_2^2 \alpha_3^2 + \alpha_3^2 \alpha_1^2 \right) + K_2 \alpha_1^2 \alpha_2^2 \alpha_3^2 \qquad (1.20)$$

20

where α_1, α_2 and α_3 are the direction cosines of the magnetisation vector relative to the crystallographic axis. In all materials the anisotropy decreases with increasing temperature and near T_c, there is no preferred orientation for domain magnetisation.

(b) Shape Anisotropy

In a non-spherical piece of material it is easier to induce a magnetisation along the long direction than along the short direction. This is so because the demagnetising field is less along a short direction, because the induced poles at the surface are farther apart. For a spherical sample there is no spherical anisotropy. The magnetostatic energy density can be written as

$$E = \frac{1}{2}\mu_0 N_d M^2 \qquad (1.21)$$

where N_d is the tensor and represents the demagnetised factor (which is calculated from the ratio of the axis). M is the saturation magnetisation of the sample. For example the shape anisotropy energy of a uniform magnetised ellipsoid is

$$E = \frac{1}{2}\mu_0 V \left(N_x M_x^2 + N_y + M_y^2 + N_z M_z^2 \right) \qquad (1.22)$$

where the tensors satisfied the relation: $N_x + N_y + N_z = 1$

(c) Surface Anisotropy

In small magnetic nanoparticles, a major source of anisotropy results from surface effects. The surface anisotropy is caused by the breaking of the symmetry and their reduction of the nearest neighbor coordination. The protective shell or ligand molecules which cover the small particles play an important role as well leading to a change of the electronic environment on the particle surface.

(d) Induced Magnetic Anisotropy

Induced magnetic anisotropy is not intrinsic to the material, but is produced by treatment such as annealing which has directional characteristics.

Both the magnitude of the anisotropy and the easy axis can be altered by appropriate treatments. Techniques such as casting, rolling or wire drawing is used to induce anisotropy in polycrystalline alloys.

1.3 Magnetism in ultrafine nanoparticles: Nanomagnetism

Ultrafine magnetic particles with nanometric dimensions are found to exhibit novel properties compared with their conventional coarse grained counterparts. Magnetic nanoparticles are dominated by unique features like single domain nature, superparamagnetism and sometimes by unusual phenomena like spin glass and frustration. The variation of coercivity in ultrafine particles is also an interesting phenomenon. The unusual behaviour exhibited by nanoparticles is mainly due to two major reasons, finite size effects and surface effects. We will briefly deal with these special features of ultrafine nanoparticles one by one.

1.3.1 Single Domain Particles

In a large body there could be a minimum domain size below which the energy cost of domain formation exceeds the benefits from decreasing magnetostatic energy. This implies that a single particle of size comparable to the minimum domain size would not break up into domains. Qualitatively it is observed that if a particle is smaller than about 100nm, a domain wall simply can't fit inside it, resulting in single domain particles .A single domain particle has high magnetostatic energy, but no domain wall energy, whereas a multidomain particle has lower magnetostatic energy but higher domain wall energy .Before application of an external field, the magnetisation of a single domain particle lies along an easy direction which is determined by the shape and magnetocrystalline anisotropies. When an external field is applied in the opposite direction, the particle is unable to respond by domain wall motion and instead the

magnetisation must rotate through the hard direction, to the new easy direction [14,17,18].

The magnetisation curve for a single domain particle can be calculated using Stoner–Wohlfarth Model [13].The coherent domain rotation concept is considered here. Consider a single domain magnetic field H which is applied at an angle θ to the easy axis of uniaxial anisotropy. If the magnetisation of the particle then lies at an angle ϕ to the magnetic field direction, the energy density of the system

$$E = KSin^2(\theta - \phi) - \mu_0 HM_s Cos\phi \qquad (1.23)$$

The energy can be minimized to find the direction of the magnetisation at any given value of the applied magnetic field. Analytic calculations are possible for this model for $\theta = 0$ to $\theta = \pi/2$. This model demonstrates how the anisotropies present in a system can lead to hysteresis.

1.3.2 Variation of coercivity with particle size in fine particles

Figure 1.14 is a schematic of the variation in coercivity with particle diameter. As the particle size is reduced, it is typically found that the coercivity increases goes through a maximum and then tend toward zero. In multidomain particles, magnetisation changes by domain wall motion .The size dependence of coercivity is experimentally found to be given by [14]

$$H_{ci} = a + \frac{b}{D} \qquad (1.24)$$

where a and b are constants and D is the particle diameter

Below a critical particle size D_c, the particles become single domain and in this range the coercivity reaches a maximum. The particles with size D_c and smaller change their magnetisation with by spin rotation.

As the particle size decreases below D_c the coercivity decreases, because of thermal effects according to

$$H_{ci} = g - \frac{h}{D^{3/2}} \qquad (1.25)$$

where g and h are constants.
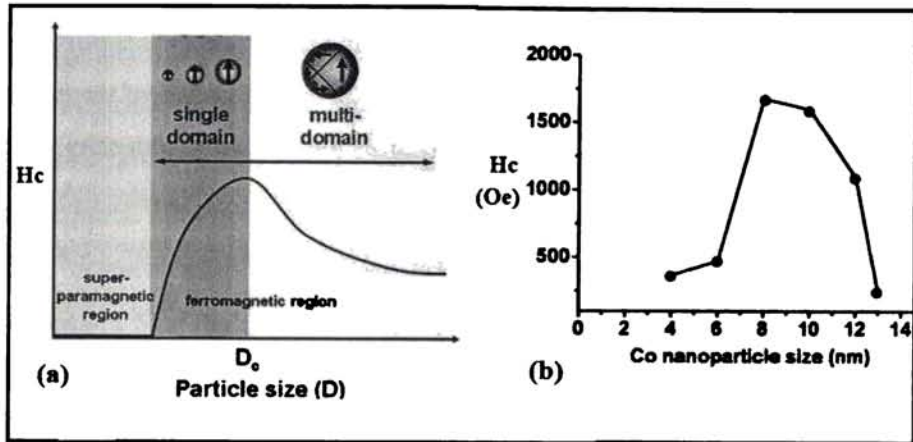
Figure 1.14 Variation of coercivity with particle size

Below a critical diameter D_S the coercivity is zero, because of thermal effects, which are now strong enough to spontaneously demagnetise a previously saturated assembly of particles. Such particles are called superparamagnetic and the phenomenon, superparamagnetism.

1.3.3 Superparamagnetism

If single domain particles become small enough that, KV (where K is the magnetic anisotropy constant and V the volume of the particle) would become so small that the thermal energy fluctuations could overcome the anisotropy forces and spontaneously reverse the magnetisation of a particle from one easy direction to the other even in the absence of an applied field. As a result of the competition between anisotropy and and thermal energies, assemblies of small particles show behaviour similar to paramagnetic materials, but with much larger magnetic moment. This moment is the moment of the particle and is equal to m=M_sV. It can

be quite large thousands of Bohr Magnetons. An applied field would tend to align this giant moment, but k_BT would fight the alignment just as it does in paramagnet. Thus this phenomenon is called superparamagnetism [14].

If the anisotropy is zero or very weak, one would expect that the total moment could point in any direction. Hence Langevin Function can be used to define magnetization $M = NmL(x)$ where $L(x) = Coth(x) - \frac{1}{x}$ as given in equation 1.6 and 1.7.

The two distinct features for superparamagnetic systems are (i) magnetisation curves measured at different temperatures superimpose when M is plotted as a function of H/T. (ii) There is no hysteresis: both remanence and coercivity are zero.

The anisotropy energy KV represents an energy barrier to the total spin reorientation hence the probability for jumping thin barrier is proportional to the Boltzmann factor $\exp\left(-KV/k_BT\right)$. At high temperature, the moments on the particles are able to fluctuate rapidly. The relaxation time τ of the moment of a particle is given by

$$\tau = \tau_0 \exp\left(\frac{KV}{k_BT}\right) \qquad (1.26)$$

where τ_0 is typically 10^{-9} s.

These fluctuations slow down (τ increases) as the sample is cooled and the system appears static when τ becomes much larger than the measuring time of the particular laboratory experimental technique.

The typical experiment with a magnetometer takes 10 to 100 seconds Using $\tau=100$s and $\tau_0=10^{-9}$ s, we can obtain the critical volume as

$$V_{sp} = \frac{25k_BT}{K} \qquad (1.27)$$

A particle with volume less than this act superparamagnetically on the 100s experimental time scale. The equation can be rearranged to yield

$$T_B = \frac{KV}{25k_B}$$
. (1.28)

T_B is called the blocking temperature. Below T_B, the free movement of the magnetic moment is blocked by the anisotropy. Above T_B the system appears superparamagnetic. The blocking temperature can be easily measured FC-ZFC measurements [chapter 2] using a SQUID/ magnetometer.

1.3.4 Frustration

Consider a lattice in which only nearest antiferromagnetic interactions operate. On the square lattice it is possible to satisfy the requirement that nearest neighbour spins must be antiparallel. However on a triangular lattice, if two adjacent spins are placed parallel, naturally there is a dilemma for the third spin. The system cannot achieve a state that entirely satisfies its microscopic state, but does possess a multiplicity of equally unsatisfied states, hence under frustration. Frustrated systems hence show metastability, hysteresis effects and time dependent relaxation towards equvillibrium. In some systems, geometry of the lattice can frustrate the ordering of the spins [13].

1.3.5 Spin glass

Spin glass can be considered as a random yet co-operative freezing of spins at a well defined temperature T_f or T_g below which metastable frozen state appears without usual magnetic long range ordering. This behaviour is normally exhibited in a non magnetic lattice populated within a dilute random distribution of magnetic atoms. The phase transition at the freezing temperature (glass transition) shows a transition to a disordered state which is distinctly different from the high temperature disordered state. The distribution of distances between

moments ina random site spin glass leads to competing interaction of RKKY type and therefore the sign depends on the distance between the ions [19,20].

The competing interaction leads to frustration leading a multi-degenerate ground state which also show a co-operative freezing transition. As a spin glass is cooled from high temperature, the independent spins slow down and build up into locally correlated unit known as clusters. As the temperature cools to $T_f(T_g)$, the fluctuation in the clusters progressively slow down. The interactions between spins become more long range so that each spin becomes more aware of spin in a progressively gray regions amend it. At T_f, the system finds one of its ground states and freezes. Below T_f the ground state appears to be glassy possessing metastability and slow relaxation behaviour. A wide range of relaxation times is also observed below T_f, showing that some free spins of small superparamagnetic clusters are still there. The co-operative spin freezing in spin glasses is still not yet fully understood.

1.3.6 Finite Size Effects and Surface effects

The magnetic properties of fine particles are strongly influenced by finite-size and surface effects, their relevance increase as the particle size decreases. Finite-size effects are due to the nanometric size of the particles, while surface effects are related to the symmetry breaking of the crystal structure at the boundary of each particle. These effects are manifested in nanometric particles through a wide variety of anomalous magnetic properties with respect to those of bulk materials. The nanoparticles are found to exhibit anomalous magnetic properties like enhancement in Curie temperature, change in coercivity, strong decrease in saturation magnetisation etc. These properties are explained on the basis of finite size effect and surface effect. By finite size scaling theory the different magnetic characteristics like T_c, H_c, M_s etc can be assumed to be varying as a function of particle size and the variations can be theoretically modeled

through equations. For example the finite scaling theory predicts a shift in transition temperature from that of a bulk should depend on the size of the system in the following manner

$$\frac{T_C(\alpha) - T_C(D)}{T_C(\alpha)} = \left(\frac{D}{D_o}\right)^{-\frac{1}{\nu}}$$ (1.29)

where $T_C(\alpha)$ is the bulk curie temperature, $T_c(D)$ is the curie temperature as a function of particle size D and n the initial exponent of the correlation length. In order to study finite scaling effect, the samples of different sizes should have same microstructure [20,21].

Like all the magnetic properties T_c can also be affected by surface effect at the nanoregime. For nanoparticles a significant fraction of atoms is on the surface and it is reasonable to expect their magnetic interaction to be different from the core atoms and hence a different average of the magnetic properties results. Early models postulated the presence of a so-called dead magnetic layer induced by the demagnetisation of the surface spins, which causes a reduction in *Ms* because of its paramagnetic response. In more recent works devoted to the study of different ferrimagnetic oxides: γ-Fe_2O_3 , $NiFe_2O_4$, $CoFe_2O_4$,$CuFe_2O_4$, in the form of nanometric particles, a random spin canting at the surface, caused by competing antiferromagnetic interactions, was observed [22]. The origin of this noncollinear arrangement of the spins is attributed to the surface effects occurring in magnetic nanoparticle surfaces.

1.4 Ferrites

Ferrites are one of the most significant magnetic materials which have been extensively used in modern electron technologies. Nanoparticles of spinel ferrites are of practical interest for a wide range of applications like high density magnetic information storage, magnetic resonance imaging, targeted drug delivery etc. Nanosized ferrites are revisited because they serve as ideal template s for

fundamental research in ferrimagnetism at the nanolevel. They also offer immense possibilities of tailoring its various properties for applications [23,24].

1.4.1 Structure of Ferrites

Ferrites are mixed metal oxides with iron (III) oxides as their main component Ferrites crystallize in three crystal types [25-27]

1. *Spinel type* with cubic crystal structure and general formula $M^{2+}Fe_2O_4$ where M = Fe, Mn, Mg, Ni, Zn, Cd, Co, Cu, Al or a mixture of these.
2. *Garnet type* with cubic crystal structure and general formula $Ln_3^{3+}Fe_5O_{12}$ where Ln = Y, Sm, Eu, Gd, Tb, Dy, Ho, Er, Tm, or Lu.
3. *Magnetoplumbite* type with hexagonal crystal structure and general formula $M^{2+} Fe_{12} O_{19}$ where M = Ba or Sr.

Spinel ferrites are the simplest of these three groups. A detailed picture of the spinel ferrites are shown below.

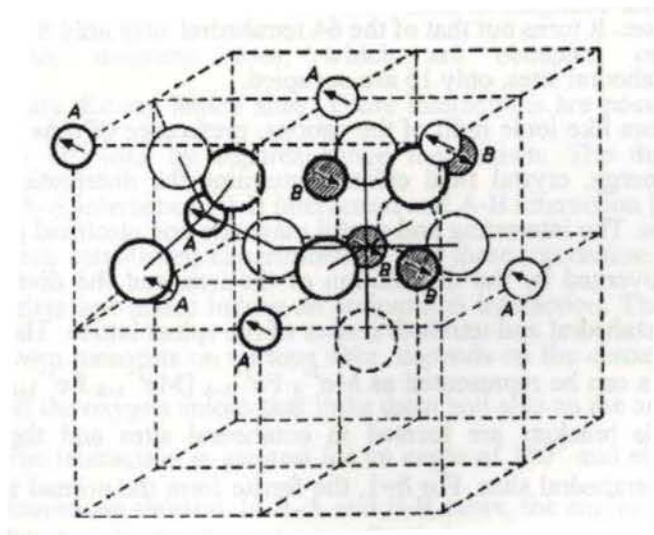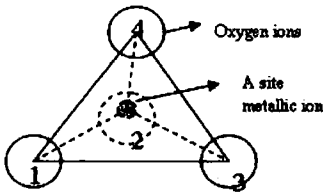Figure 1.15 Unit cell of spinel structure
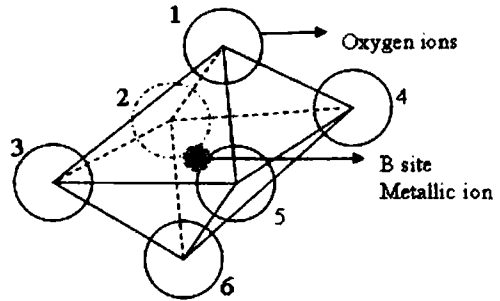
Figure 1.16 Tetrahedral Coordination   **Figure 1.17** Octrahedral Coordination

Spinel ferrites crystallize into the spinel structure, which is named after the mineral spinel, $MgAl_2O_4$. The spinel structure is determined primarily by the oxygen ion lattice (figure 1.15). The oxygen anions are packed in a face centered cubic arrangement such that there are two kinds of interstitial space between the anions-tetrahedrally co-ordinated A sites (figure 1.16) and octahedrally co-ordinated B sites (figure 1.17). There are eight formula units of $M.Fe_2O_4$ in a unit cell. Thus in a unit cell of 32 oxygen anions, there are 64 tetrahedral sites and 32 octahedral sites. It turns out that of the 64 tetrahedral sites only 8 are occupied and out of 32 octahedral sites, only 16 are occupied.

Factors like ionic radii of the cations, preference of ions to specific sites, Madelung energy, crystal field effects determine the distribution of cations in spinel ferrites. The interesting and useful magnetic and electrical properties of the spinel are governed by the distribution of the iron and the divalent metal ions among the octahedral and tetrahedral sites of the spinel lattice. The general cation distribution is can be represented as $Me^{2+}_\delta Fe^{3+}_{1-\delta} [Me^{2+}_{1-\delta} Fe^{3+}_{1+\delta}]O_4$ where the cations inside brackets are located in octahedral sites and the other outside brackets in tetrahedral sites. For $\delta=1$, the ferrite form the normal spinel while for $\delta=0$, it is called inverse spinel. For random distribution $\delta=1/3.ZnFe_2O_4$ and $CdFe_2O_4$ are normal spinels with all the divalent metal cation distributed in the tetrahedral sites. In inverse spinels like $NiFe_2O_4$ and $CoFe_2O_4$, the metallic cation

occupies the octahedral sites only with ferric ions equally distributed in the two sites [27,28].

Coming to the nanolevel a disordered cation distribution compared with the bulk has been observed in a number of ferrite systems. An inversion of degree of 60% (chapter 3) was reported in Manganese ferrite compared with 20% inversion in bulk. Also in Nickel ferrite and cobalt ferrite nanoparticles Ni^{2+}/Co^{2+} ions were experimentally observed in the tetrahedral sites. Most interesting is the cation distribution found in nanoparticles of zinc ferrite, where zinc ions with the highest preference for tetrahedral sites is found in the octahedral sites also. All these redistribution of cations lead to unexpected properties in these ferrites at the nanoregime [29-32].

1.4.2 Magnetic Properties of Ferrites

As the name suggests, ferrites exhibit a ferrimagnetic ordering. Neel explained the spontaneous magnetisation of these ferrites on the basis of Heisenberg's exchange forces. In ferrites three kinds of magnetic interactions are possible between, magnetic ions, which are occupied in the two crystallographically distinct lattice sites. These interactions are possible through the intermediate O^{2+} ions by superexchange mechanism. The three possible interactions are A-A interaction, B-B interaction and A-B interaction [27,28].

It has been established experimentally that these interaction energies are negative for ferrites and hence induce an antiparallel interaction. The strength in interaction between moments on various sites, depends on the distances between the metal ios and the oxygen anions that links them and also on the angle between the three ions.The interaction is greatest for an angle of 180° and also where the interatomic distances are shortest. In A-A and B-B cases, the angles are too small or the distances between the metal ions and oxygen ions are too large. For an undistorted spinel, the A-O-B angles are about 125° and 154°. The B-O-B angles are 90° and 125°. In the A-A interaction the angle is about 80°. Therefore, the

interaction between moments on the A and B sites is strongest. The B-B interaction is much weaker and most unfavourable situation occurs in A-A interaction. Thus with A-O-B interaction predominating the spins will be oppositely magnetised in the sublattices A and B ,with a resultant magnetic moment equal to the difference between those of A and B site ions.

In developing his theory of ferrimagnetism, Neel postulated two separate sublattice magnetisation corresponding to the two sublattices. In general, the value of saturation magnetisation based on Neel's two sublattice model is that the resultant saturation magnetisation is may be written as $M_S = |M_B - M_A|$. The variation of magnetisation with temperature in ferrites depends on the magnitude of sublattice magnetisations at 0 K and the ratios of the magnitudes of exchange interactions between the sublattices. There can be deviations in the net magnetisation which can be attributed to several factors: (i) The cation distribution on various sites may not be as perfect as predicted (eg. $MnFe_2O_4$) (ii) The orbital moment may not be quenched (eg. $CoFe_2O_4$) (iii) The direction of the spins may not be antiparallel in the interactions. They may be canted. Ferrites exhibit hysteresis phenomenon during the magnetisation cycle (figure 1.1). The shape of the loops varies with respect to individual ferrites.

When the particle size is reduced to a few tens of nanometers, ferrite materials exhibit high coercive field, high Curie temperature and low saturation magnetisation as compared to their corresponding bulk values. These phenomenon have been explained on the basis of finite size scaling effects and surface effects occurring in the nanoregime. In addition to this, the presence of a different cation distribution in the nano regime leading to different type of interactions play a significant role in deciding the magnetic properties.

1.4.3 Electrical properties of ferrites

Ferrites can be clubbled along with the class of somewhere between semiconductors and insulators. Spinel ferrites have high electrical resistivities and

low eddy currents and dielectric losses. This is a major advantage over ferromagnetic materials. In ferrites, the temperature dependence of mobility of affects the conductivity and the carrier concentration is almost unaffected by temperature variation. The charge carriers in ferrites are localized at the magnetic atoms .In ferrites the cations are surrounded by close packed oxygen anions and on can be treated as isolated from each other. There will be little direct overlap of the anion charge clouds or orbitals. Alternatively the electrons associated with particular ions cations will remain isolated and hence a localized electron model is more appropriate in the case of ferrites rather than the collective electron band model. The main conductivity mechanism in ferrites is attributed to electrons hopping between Fe^{3+}/Fe^{2+} in octahedral sites. Resistivity in ferrites is very sensitive to preparation techniques, stiochiometry, sintering condition, microstructure etc.

The measurement of electrical properties as a function of frequency and analysis by complex dielectric spectroscopy allow a separation of contribution of grains, grain boundaries and electrode polarization .The electrical studies provide important information on the behaviour of localized electric charge carriers, which give rise to a better understanding the dielectric polarization. It is to be of notice that electrical properties in ferrites are affected by the distribution of cations in the sites, by non magnetic and magnetic substitutions ,by the amount of Fe^{2+} present, sintering conditions, grain size and grain growth effects[28]. In the case of nanostuctured ferrites the electrical behaviour is found to be quite interesting on account of the large number of interfaces formed at the boundaries of the nanocrystallites. As in the case of magnetic properties an unexpected cation distribution has a direct influence on the electrical properties of ferrites at the nanoregime. The electrical properties of ferrites will be dealt in detail in chapter 2.

1.4.4 Synthesis techniques for ferrite nanoparticles.

Ferrites in bulk are usually manufactured using conventional ceramic processing techniques. Since we are particularly interested in nanoparticles of ferrites, the important synthesis techniques are detailed here.

The challenge is to control the nanoparticles size, shape and properties, to assemble the nanoparticles for a given purpose and to make them from a variety of nanomaterials. Generally two main approaches are adapted for the synthesis of nanoparticles: bottom up method and top down method. In bottom-up approach the nanoparticles are built up from atom by atom, or molecule by molecule levels by controlling the reaction parameters. Top down method is most applied in the traditional particle making process. Here the nanoparticles are synthesised by breaking down bulk materials gradually into smaller sizes until they are nanosized. Mechanical breakdown such as high energy ball milling is a simple case of the top down strategy.

Synthesis techniques can be generally classified into chemical and physical methods according to the different scientific process involved. The physical processes involve only changes in the physical state, such as size, shape and phase of the matter. Condensing gaseous metal vapours into nanoparticles is an example. Most of the chemical methods [33-36] can be included in the bottom up method and physical methods like high energy ball milling[37] , lithography or patterning etc. are examples of top down method. Some of the important methods for the preparation of ferrite nanoparticles in the laboratory are sol-gel synthesis [38-40], and chemical co-precipitation techniques [41-43].They will be described in the next chapter 2.

1.4.5 Applications of Ferrites

Ferrites in the bulk have many applications in high frequency devices as an ac field does not induce undesirable eddy currents in an insulating materials. Nickel zinc ferrites are used as deflection yoke core in a television picture tube.

Since ferrites have high resistivity and low eddy current loss, ferrite cores are used for flyback transformers in television sets. This greatly increases the energy received by a receiving antenna. The ferrites combined with their high permeability also make them suitable for filter inductor applications. Ferrites are used in cores for magnetic memories [44, 45]. Ferrites are used at microwave frequencies for somewhat different reasons [46-48]. At these frequencies, they exhibit non-reciprocal properties, i.e., the attenuation and phase shift of microwaves propagating through them have different values for the two opposite directions of propagation in a waveguide. The square loop characteristic along with the fast switching times t, minimal temperature variation, mechanical strength and low magnetostriction make them ideal for memory applications.

The broad applications of ferrite nanoparticles include high density information storage, ferrofluid technology, magnetic resonance imaging enhancement, magnetically guided drug delivery and magnetocaloric refrigeration [49-52]. Using a combination of ferrite nanoparticles as contrast enhancement agents, harmless radio waves and computer technology, magnetic Resonance Imaging creates detailed images of the soft tissue morphology. Nanopowdered ferrites are successfully used for the design of magnetic storage and recording devices. An enhanced magneto-optical effect and large magnetoelestic effect in cobalt ferrite are really promising. The magnetostrictive properties of cobalt ferrite nanoparticles are tailored for stress sensor applications Ferrofluids are stable colloidal suspensions composed of magnetic nanoparticles in organic or inorganic liquid carriers. The biocompatible ferrofluids based on ferrites are really promising for biomedical applications like cell separation and purification and magneto hyperthermia of tumour cells. Most of the biocompatible fluids are based on magnetitie and maghemite. Zinc ferrite nanoparticles have generated a lot of interest owing to their potential applications in gas sensor and semiconductor photocatalysis [53, 54].

1.5 Nanocomposites

The composites are usually designed and fabricated combining two or more different materials or phases to produce a single material that behaves as a homogenous entity and has predictable and reproducible properties. Common composite materials include polymer metal, polymer-ceramic, metal-ceramic and polymer-metal-ceramic components or mixtures of the same class of materials with distinct phases. Mechanical composite materials continue to be an integral part of our daily lives. Composites have wide range of applications from sports equipment to transportation vehicles. They are found in aircraft components, ranging from the seat frames to sections of wings. Automobile tires are made of rubber reinforced with steel thread to extend life and increase performance at high speeds. The emerging fields of nanotechnology and nanoengineering provide a path to design and fabricate multifunctional nanocomposites [55].

1.5.1 Applications of Magnetic Nanocomposites

Magnetic nanocomposites in which magnetic nanoparticles are dispersed within nonmagnetic or magnetic matrices are practically useful. Magnetic recording, giant magnetoresistance and magnetic refrigeration are some important areas in which magnetic nanocomposites have relevance [56-59]. The increase in storage density of hard disk drives and parallel decline in cost per megabyte (MB) of storage is happening rapidly. Co/Pt /C nanocomposite films have been prepared that show the high coercivity and chemical stability required for high density recording media. Magnetic nanocomposites materials find applications in ferrofluids, imaging and separation technologies and as magnetic carriers for drug delivery. The challenge here is to make magnetic nanocomposite particles (eg . silica coated iron oxide) resistant to agglomeration and chemical attack. The magnetic particles are often coated with protective and functional materials such

as silica which can be effectively done and easily by sol-gel synthesis or liquid phase coating processes [56-59].

Magnetic particles embedded in polymer matrices (iron oxides inside a conductive polyaniline matrix) have also been synthesized for the fabrication of conductive superparamagnetic plastic films. The advantages of these composites are an increased sensitivity to detect changes of magnetic field and higher working temperature range, which could be used for the development of miniaturized and energy saving microwave antenna, inductors, sensors or data memories for space applications. In a magnetic ceramic composite the resistivity can be drastically increased leading to a significantly reduced eddy current losses .In addition the exchange coupling between neighboring magnetic nanoparticles can overcome the anisotropy and demagnetising effect ,resulting in much better soft magnetic properties than conventional bulk form materials. It has been found that a Co or Fe nanocomposite system can possess permeability much higher than that obtained from bulk due to the exchange coupling effect. Deposition of conductive polymer chains and magnetic nanoparticles in a layer-by layer fashion may lead to new properties such as giant magnetoresistance (GMR) and novel organic based nanostructured GMR materials[55,56].

A brief account of magnetocaloric effect is provided below since one of the themes of this investigation is in identifying the utility of these nanocrystalline magnetic materials as a magnetic refrigerant

1.6 Magnetocaloric Effect

The magnetocaloric effect is (MCE) simply the remarkable ability of a magnetic material to heat up in the presence of a magnetic field and cool when the magnetic field is removed. The magnetocaloric effect was first discovered in the element iron by Warburg in 1881. For a simple ferromagnetic material near it's magnetic ordering temperature, when a magnetic field is applied, the unpaired

spins are aligned parallel to the magnetic field and this causes the sample to warm up [60,61].

The MCE, which is the cooling and warming of a magnetic material in response to a changing magnetic field is similar to the cooling and warming of a gaseous medium in response to an adiabatic expansion and compression [62]. Thus MCE forms the basis for magnetic refrigeration technology, which operates by magnetising and demagnetising the magnetic material[63]. For continuous magnetic refrigeration, one must reject the heat generated in the magnetic material when the magnetic field is turned on and then on the demagnetisation step a thermal link is used to cool the load. By continued repetition of these two steps, refrigeration is accomplished. Subsequent work for the next four decades showed that magnetic refrigeration could be used to cool near room temperature using gadolinium metal. It was in 1976, that Brown described a near room temperature magnetic refrigerator using gadolinium pellets and a water–ethyl alcohol solution as a regenerator in a 7T field [64,65] A maximum temperature span of 47K was attained after 50 cycles. Thus magnetic refrigeration was used to cool near room temperature using Gd metal or to cool high temperature superconducting magnets using different lanthanide intermetallic compounds.

In the early 1990's there formed a team of scientists from the Ames Laboratory, Iowa University and Astronautics Corporation of America was constituted to design, construct and test a proof of principle of apparatus to show that magnetic refrigeration is a viable alternate technology to vapour–cycle compression cooling. The future for both basic and applied research on magneto caloric materials is quite promising, but a number of technological hurdles need to overcome before magnetic refrigerators or air conditioners start to roll off the production lines. Significant activity has also occurred in the refrigeration community to employ the MCE in cycle in order to construct a magnetic refrigerator operating either at cryogenic temperatures or near room temperatures. These two constitutes the main applications of MCE [65,66].

1.6.1 Theory and equations of Magnetocaloric Effect

MCE, the distinct property of magnetic materials can be perceived either as a change of material's magnetic entropy upon the isothermal application/ removal of a magnetic field (ie, ΔS_m) or as a change of material's temperature when a magnetic field is altered adiabatically (ie, ΔT_{ad}).

The equations of MCE can be derived using Maxwell's thermodynamic relations assuming that the magnetisation (M) and entropy (S) are continuous functions of the temperature (T) and magnetic field (H). Then the infinitesimal isobaric – isothermal magnetic entropy change can be related to M, H and T using one of the Maxwell's relations[67-69]

$$\Delta S_m(T,H)_{\Delta H} = \int_{H_i}^{H_F} \frac{\partial M(T,H)}{\partial T} dH \qquad (1.30)$$

$$\Delta T_{ad}(T)_{\Delta H} = -\int_{H_i}^{H_F} \left(\frac{T}{C(T,H)}\right)_{H()} \left(\frac{\partial M(T,H)}{\partial T}\right)_H dH \qquad (1.31)$$

This is the adiabatic temperature change associated with the adiabatic magnetic field change. Thus, equations (1.30) and (1.31) represent the two basic equations of MCE.

Since both $\Delta S_m(T)_{\Delta H}$ and $\Delta T_{ad}(T)_{\Delta H}$ are proportional to the derivative of the magnetisation with respect to temperature at constant magnetic field , MCE gradually decreases both below and above the magnetic ordering temperature. Thus, conventional ferromagnets typically display a caret like $\Delta S_m(T)_{\Delta H}$ and $\Delta T_{ad}(T)_{\Delta H}$ (e.g., Pure crystalline Gd, which orders ferromagnetically at 294K). A few materials form the ferromagnetically ordered phase from the paramagnetic state through a first order magnetic phase transition. In these cases, since the phase transition is of the first order, $\partial M / \partial T$ is larger than usual and therefore the

magnetocaloric effect is also large. We call this type of MCE as sky -scraper or giant MCE .Giant MCE in materials like gadolinium silicides [70] are studied on account of their potential to be used as magnetic refrigerants near room temperature.

1.7 Motivation of the present work

With the initiation of nanotechnology there is renewed interest in ferrites since many of the useful properties of these materials can be modified suitably. The finite size effects in the nanoregime can be employed to tailor structural, magnetic and electrical properties of nanostructured ferrites. In the nanoregime altogether different mechanisms are responsible for the modified properties. The structural, magnetic and electrical properties of ferrites are found to be sensitive to their composition and microstructure, which in turn are dependent on the processing conditions.

In the nanoregime, in the case of spinel ferrites, there are distinct deviations in magnetic properties with respect to their bulk counterparts. For instance, though zinc ferrite is a normal spinel in the micron regime and nonmagnetic, in the nanoregime it is found to exhibit an inversion and hence exhibit a net magnetisation at room temperature nanosized nickel ferrite is reported to be exhibiting increased magnetisation by some researchers while others have reported reduced magnetisation with respect to their bulk counterparts Core shell model have been invoked to account for the reduced magnetisation of nano nickel ferrite while cation redistribution and the existence of surface spins have been attributed to the case where there is increased magnetisation.

Although the electrical and magnetic properties of ferrites in the micron regime have been well studied and has led to several applications, a thorough understanding of their electrical properties in the nanoregime is lacking. There are numerous reports with regard to the finite size effects on the structural and

magnetic properties of ferrite nanoparticles. However there exist only a few systematic studies on the electrical properties of ferrites in the nanoregime.

The occupancy of zinc ions in octahedral sites in the nanoregime can alter the cation distribution to a great extent and this will modify the structural and magnetic properties in the case of $Mn_{1-x}Zn_xFe_2O_4$ nanoparticles. This is an interesting aspect as far as the magnetic behaviour of these ferrites are concerned. Hence a systematic study on the magnetic properties of manganese zinc ferrite series will be very appropriate. The frequency dependent ac conductivity and temperature dependent dc conductivity are deciding factors for many technological applications involving ferrites. For instance one can obtain information about the mechanism of conduction and evaluate the activation energy for electrical conduction by studying the ac and the dc conductivities A detailed investigation on the transport properties of nanoparticles belonging to a series of the type $Mn_{1-x}Zn_xFe_2O_4$ mixed ferrite can throw light on the mechanism of electrical conduction in nanosized mixed ferrites This is possible by subjecting these materials to conductivity studies both in dc and ac regime over a wide range of frequencies. An investigation on the transport characteristics of these series will be in the right direction in order to develop in order to delve deep into the different mechanism that operate at nanodimensions.

Investigations on cobalt ferrite have shown that it can be a suitable material for developing new devices and technologies in the areas of strategic importance like high density magnetic storage and magneto-optical devices. Metal bonded cobalt ferrite composites have been shown to be promising candidate materials for use in magnetoelastic stress sensors, due to their large magnetostriction and high sensitivity of magnetisation to stress .There has been a growing interest in developing biocompatible magnetic fluids on account of their biomedical applications such as magnetic hyperthermia for tumor cells and drug targeting. Also, recent reports on magnetocaloric properties of the cobalt ferrite nanoparticles has added to the curiosity in the system for possible refrigeration

applications. So nanosized cobalt ferrite is a system where the coercivity can be tuned considerably by manipulating the anisotropy factors and there is a subject of interest for material scientists.

Metal nanoparticles are highly unstable and hence very difficult to synthesise in the nanodimensions. Nickel nanoparticles embedded in a polymer matrix are important not only from a commercial point of view but they are also important from a fundamental perspective. They are ideal template for studying the size effects on the magnetic properties. The optical properties of these particles at the nanolevel also assume significance. Although numerous reports exist on the incorporation of Fe, Ni nanoparticles in functionalized polystyrene membranes /sheets, the incorporation these metal nanoparticles in resinous beads are not yet reported to the best of our knowledge.

Magnetocaloric effect, the magnetothermal phenomenon, associated with any magnetic material may appear to be a simple one. A detailed look over the subject add strength to the belief that it should be studied in an extensive manner considering it's theoretical as well as practical aspects. Magnetocaloric properties in ferrite and metal nanoparticles are least investigated on account of the high ordering temperature (T_c) exhibited by these nanoparticles. The tuning of Curie temperature of these particles is found to be cumbersome. But coming to the nanodimensions the unique property of superparamagnetism along with the blocking phenomenon at lower temperatures is very important as far as the MCE properties are considered. The blocking temperature of the nanoparticles is decided by a horde of factors namely, particle size, shape and distribution, magnetic anisotropy and interparticle interactions. Thus the blocking temperature can be modified in ferrite nanoparticles by altering the particle dimensions and anisotropy. Metal polymer nanocomposites are endowed with the advantage of controlling the interparticle interactions at the metal polymer interface which can result in a near room temperature T_B for these materials. Thus the broad objectives of the present investigations can be listed as follows.

1.8 Objectives of the work

> Synthesis of mixed ferrites in the nanoregime belonging to the series of $Mn_{1-x}Zn_xFe_2O_4$ (for x=0, 0.1, 0.2........1) by chemical co-precipitation technique.

> Evaluate the impact of zinc substitution on the structural and magnetic properties of $Mn_{1-x}Zn_xFe_2O_4$

> Analysis of the electrical properties of the series $Mn_{1-x}Zn_xFe_2O_4$.

> Synthesis, structural, magnetic and electrical characterisation of sol-gel derived cobalt ferrite nanoparticles.

> Synthesis of metal polystyrene nanocomposites containing elemental iron and nickel by a novel ion exchange reduction method.

> Study the effect of cycling on the structural and magnetic properties of the nanocomposites.

> Estimate the characteristic Magneto caloric values, that is, magnetic entropy change associated with the cobalt ferrite nanoparticles and metal nanocomposites.

> Correlation of results.

References

1. Edward L. Wolf, *Nanophysics and Nanotechnology: An Introduction to Modern Concepts in Nanoscience*, 2nd editon ,Wiley, John & Sons, 2006

2. Charles P Poole. Jr., Frank J Owens, *Introduction to Nanotechnology* , Wiley, John & Sons,2003

3. Hari Singh Nalwa *Nanostructured materials and Nanotechnology* , Academic press, London San Diego, *Academic Press*, 2002.

4. Yi Cui, Charles M., Lieber, Science 291(2001) 851

5. Robert A. Freitas, Jr. Journal of Computational and Theoretical Nanoscience , 2 (2005) 1

6. Jena, P. (Editor), Khanna, S. N. (Editor), Rao, B. K. (Editor) *Clusters and Nano-Assemblies: Physical and Biological Systems,* World Scientific Publishing Co., Inc. New Jersey,

7. D Heyes, O.I Micic, T Nenadovic, V Swayambhunathan, D Miesel, J. Phys. Chem, 93 (1989) 4603

8. H. Weller, H.M Schmidt, U. Koch, A. Fojtik, S. Baral, A Henglein, W. Kunath, K. Weiss, E. Diemen, Chem. Phys. Lett, 124 (1986) 557

9. K. Raj, R. Moskowitz and R. Casciari, J. Magn. Magn. Mater., 149 (1995), 174.

10. C.N.R. Rao, A. Muller and A.K. Cheetham, *The Chemistry of Nanomaterials Synthesis, Properties and Applications, Volume-1,* WILEY-VCH Verlag GmbH & Co. KgaA, Weinheim (2004).

11. Q.A. Pankhurst, J. Conolly, S.K. Jones and J. Dobson, J. Phys. D: Appl. Phys., 36 (2003) R167.

12. I. Hilger, R. Hergt and W.A. Kaiser, J. Magn. Magn. Mater. 293 (2005) 314.

13. Stephen Blundell, *Magnetism in Condensed Matter*, Oxford University Press (2001) Oxford

14. B. D. Cullity, *Introduction to Magnetic Materials*, Addison Wesley Publishing Company (1972), London.

15. Soshin Chikazumi, *Physics of Magnetism*, John Wiley and Sons, Inc (1964), New York

16. D. Hadfield, *Permanent Magnets and Magnetism*, John Wiley and Sons (1962), London

17. J. Frenkel, J. Dorfman: Nature, 126 (1930) 274

18. C. P. Bean, J. D. Livingston, J. Appl. Phys, Supplement to 30 (4) (1959) 120S-129S

19. Debashish Chowdhary, *Spin Glasses and Other Frustrated Systems*, World Scientific (1986), London

20. J. Frenkel, J. Dorfman: Nature, 126 (1930) 274

21. R. H. Kodama, Salah A. Makhlouf, and A. E. Berkowitz" Phys. Rev. Lett. 79, (1997) 1393 .

22. R.H. Kodama, J. Mag. Mag. Matr., 200 (1999) 359

23. R.D. McMichael, R.D. Shull, L.J. Swartzendruber and L.H. Bennett, J. Magn. Magn. Mater., 111 (1992) 29.

24. D.G. Mitchell, J. Magn. Reson. Imaging, 7 (1997) 1.

25. J. Smit, and H.P.J. Wijn, *Ferrites*, Philips Technical Library Netherlands (1959).

26. Charles Kittel, *Introduction to Solid State Physics,* 7th Edition, John Wiley & Sons, Inc., Singapore (1996).

27. R. Valenzuela, *Magnetic Ceramics*, Cambridge University Press, (1994) London.

28. V. R. K. Murthy, B. Viswanathan, *Ferrite Materials, Science and Technology,* Narosa Publishing House (1962), New Delhi

29. Sakurai J and Shinjo T. J. Phys. Soc .Jpn 23 (1967)1426

30. H. H. Hamdeh, J. C. Ho, S. A. Oliver, R. J. Wiley, G. Oliveri, G. Busca: J. Appl. Phys 81 (1997) 1851

31. F. K. Lotgering,, J. Phys. Chem. Solids, 27 (1996) 139

32. S. A. Oliver, H. H. Hamdeh, J. C. Ho: Phys. Rev. B 60 (1999) 3400

33. Hironori Iida, Takuya Nakanishi, Harumi Takada and Tetsuya Osaka, Electrochimica Acta, 52 (2006) 292.

34. Shannon A. Morrison, Christopher L. Cahill, Everett E. Carpenter, Scott Calvin, Raja Swaminathan, Michael E. McHenry and Vincent G. Harris, J. Appl. Phy., 95 (2004) 6392.

35. Shu-Hong Yu, Takahiro Fujino and Masahiro, J. Magn. Magn. Mater., 256 (2003) 420.

36. V. Sepelak, D. Baabe, D. Mienert, D. Schultze, F. Krumeich, F.J. Litterst and K.D. Becker, J. Magn. Magn. Mater., 257 (2003) 377.

37. Miha Drofenik, Matjaz Kristal, Andrej Znidarsic, Darko Hanzel and Darja Lisjak, J. Am. Ceram. Soci., 90 (2007) 2057.

38. Mathew George, Asha Mary John, Swapna S. Nair, P.A. Joy and M.R. Anantharaman, J. Magn. Magn. Mater., 302 (2006) 190.

39. Souilah Zahi, Mansor Hashim and A.R. Daud, Materals Letters, 60 (2006) 2803.

40. A.S. Albuquerque, J.D. Ardisson, W.A.A. Macedo, J. L. Lopez, R. Paniago and A.I.C Persiano, J. Magn. Magn. Mater., 226 (2001) 1379.

41. Anjali Verma and Ratnamala Chatterjee, J. Magn. Magn. Mater., 306 (2006) 313.

42. R.M. More, T.J. Shinde, N.D. Choudhari and P.N. Vasembekar, J. Mater. Sci., 16 (2005) 721.

43. C. Caizer and M. Stefanescu, J.Phys. D: Appl. Phys., 35 (2002) 3035.

44. T. Nakamura and E. Hankui, J. Magn. Magn. Mater., 257 (2003) 158.

45. S.A. Ghodake, U.R. Ghodake, S.R. Sawant, S.S. Suryavanshi and P.P. Bakare, J. Magn. Magn. Mater., 305 (2006) 110.

46. Hong-Mei Xiao, Xian-Ming Liu and Shao-Yun Fu, Composites Science and Technology, 66 (2006) 2008.

47. A. Verma, R.G. Mendiratta, T.C. Goel and D.C. Dube, Journal of Electroceramics, 8 (2002) 203.

48. Xiangcheng Li, Rongzhou Gong, Zekun Feng, Junbing Yan, Xiang Shen and Huahui He, J. Am. Ceram. Soc., 89 (2006) 1450

49. R.H. Kodama, A.E. Berkowitz, E.J. McNiff Jr. and S. Foner, Phys. Rev. Lett., 77 (1996) 394.

50. Sun S, Murray C B, Weller D, Folks L, Moser A, Science 287 (2000.) 1989

51. Pankhurst Q A,Connolly J,Jones S K,Dobson J, J.Physics D: Appl Phy. 36, (2003),R167

52. M. H. Kryder, MRS Bull., 21(1996) 17

53. C.C. Berry, A.S.G Curtis, J. Phys. D :Appl. Phys. 36 (2003), R198

54. S. Gubbala, H. Nathani, K. Koizol and R.D.K. Misra, Physica B, 348 (2004) 317.

55. Pulickel M Ajayan, Linda S. Schadler, Paul V. Braun, *Nanocomposite Science and Technology, Wiley CH Publischers Verlag,* GmbH &Co. KGaA, Weinhein.

56. Ron Dagani, Nanostructured Materials Promise To Advance Range of Technologies, Science/Technology, 1992, 18

57. R. F.Ziolo, E.P.Giannelis, B.A Weinstein, Michela P. O'Horo, B.N.Gaguly, V.Mehrotra, M.W.Russel, D.R.Huffman. Science 257, (1992) 219

58. D.Chakravorty *Bull. Mat. Sci.* 15 (1992)411

59. R.D.Shull and L.H.Bennet, Nanocomposite magnetic materials, J. Nanostructured Materials 1(1992), 83

60. E Warburg Ann.Phys.Chem.13 (1881)141

61. P.Debye, Ann.Physik.81(1926)1154

62. A. M Tishin , Cryogenics 30 (1990) 720.

63. V. K Pecharsky and Karl A Gschneidner, Jr, Adv. Cry. Eng.42, (1996) 423

64. G.V Brown, Journal of Applied Physics 47 (1976) 3673

65. C.Zimm, A .Jastrab, A. Sternberg, M. Osborne, V. K Pecharsky, K. A.Gschneidner Adv. Cry. Eng . 43 (1998) 1759-1766

66. J R Hull and K L Uherka,Energy,14(1989)177

67. A H Morrish, *The Physical Principles of Magnetism*, Wiley &Sons ,NewYork (1965)

68. R P Hudson, *Principles and Applications of Magnetic Cooling*, North Holland Publishing company, Amsterdam, London (1972)

69. Herbert B Callen, *Thermodynamics* (Wiley , New York)

70. V. K Pecharsky and Karl A Gschneidner, Jr, Adv. Cry. Eng,43 (1998)1729

Chapter 2

Experimental Techniques

The advent of nanoscience and nanotechnology demands novel preparative techniques for ensuring monodispersibility and purity. Subsequently, proper characterisation using modern analytical techniques is a prerequisite before these results are interpreted. This leads to a better understanding of the physics of these materials at nanodimensions. This chapter is mainly concerned with the experimental techniques which include the methods of synthesis of the ferrite nanopowders and metal nanocomposites and the experimental techniques employed for characterising these samples at different intermediate stages. The synthesis methods for ferrite nanopowders involve sol-gel and co-precipitation techniques while for the synthesis of metal nanocomposites an ion exchange method has been employed. Analytical techniques namely X-Ray Diffraction (XRD), Fourier Transform Infrared Spectroscopy (FTIR), Transmission Electron Microscopy (TEM), Energy Dispersive X-Ray Spectroscopy (EDS), Scanning Electron Microscopy (SEM), Inductively Coupled Plasma Analysis (ICP), Vibrating Sample Magnetometer (VSM) and LCR meter were utilised to characterise the materials. Cole-Cole plots were plotted to extract information on the dielectric properties of mixed ferrites. So the technique of Cole-Cole plot is also described. Magnetic entropy change is a measure of the cooling capacity of magnetic materials if there are to be deployed as a magnetic refrigerant. So the estimation of ΔS_m values are also described in this chapter.

2.1 Synthesis Techniques

Nanomagnetic materials are very sensitive to processing conditions and impurity levels because small contents of non magnetic impurities can alter the properties substantially. Hence the choice of technique for the preparation of nanosized ferrites and composites is very vital. This ensures single phasic materials of high purity.

2.1.1 Chemical Co-Precipitation

Co-precipitation of various salts (nitrates, sulphates, chlorides, perchlorates etc.) under a fine control of pH by using NaOH or NH_4OH solutions yields corresponding spinel oxide nanoparticles [1-3]. Particle size of the co precipitated material is strongly dependent on the pH of the precipitation medium and molarity of the starting precursors. Consequently, control over the particle size can be easily achieved. The reaction and transport rates are affected by the concentration of reactants, temperature, pH, the order in which the reagents are added to the solution and mixing. The structure and crystallinity of the particles can be influenced by reaction rates and impurities. Particle morphology is influenced by factors such as supersaturation, nucleation, and growth rates. At low supersaturation, the particles are small, compact and well formed and the shape depends on crystal structure and surface energies. At high supersaturation levels, large and dendritic particles are formed. Nanoparticles of mixed ferrites belonging to the series of $Mn_{1-x}Zn_xFe_2O_4$ (x=0 to 1) were synthesized by wet chemical co-precipitation. Chlorides of manganese, zinc and iron are used as precursors for the precipitation [4]. Sodium hydroxide was used as the precipitating agent. The precipitation was done under specific conditions of temperature and pH. However, homogenous and monodispersed nanoparticles were precipitated. Co-precipitation method offers distinct advantages [5] like simple and rapid preparation, easy control of particle size and composition and

50

various possibilities to modify the particle surface state and overall homogeneity over other preparative methods. The detailed procedure is given in chapter3.

2.1.2 Sol-gel Synthesis

Sol-gel method was employed for the synthesis Cobalt ferrite nanoparticles. In sol-gel process, chemical methods are used to turn solutions of metal compounds into gels. Sol-gel process can be used to prepare metal oxides via hydrolysis of reactive metal precursors in an alcoholic solution resulting in corresponding hydroxides [6-8]. Condensation of the hydroxide molecules by elimination of water leads to the formation of a metal hydroxide. When all hydroxides species are linked to one another in a network, gelation is achieved and a dense porous gel is obtained. Further heating of the gel at higher temperature leads to the ignition of the gel to form ultrafine powders of metal oxides. Though sol gel methods yield ultrafine particles and proper homogeneity, contamination of the end product is sometimes a drawback of this method [9].

For the preparation of cobalt ferrite nanoparticles, Nitrates of cobalt (Co^{2+}) and iron (Fe^{3+}) were dissolved in ethylene glycol to form a sol. The heating of sol to gel and further heating at higher temperature lead to the ignition of the gel. The product is nanopowders of cobalt ferrite. A descriptive account is provided in   chapter 5.

2.1.3 Ion Exchange Reduction Method

Metal nanoparticles were found to be highly unstable on account of their high reactivity at the surfaces. The development of metal nanoparticles in a host matrix is found to be very promising for minimizing this stability problem. A combination of complementary properties of the metal nanoparticles and the host matrix contribute to the properties of nanocomposite making it multifunctional. Polymers have been considered to be excellent host matrix for composite materials [10-11]. Several advanced polymer composites have been synthesized

with a wide variety of inclusions like metals, semiconductors, carbon nanotubes and magnetic nanoparticles. Ziolo *et al.* [12] have used the special features of ion exchange resins based on polystyrene to prepare γ-Fe$_2$O$_3$ polymer nanocomposite with magnetic functionality. Mesoporous ion exchange resins are characterized by permanent percolated porosity formed by phase separation occurring during polymerization and have a large amount of functional groups at the pore surface which can load a variety of metal ions. These metal ions are subsequently reduced in the matrix to form metal polymer nanocomposites.

A cross-linked polymer of styrene and divinyl benzene (in the case of strong acid cationic exchange resin) or a cross-linked polymer of styrene and acrylic acid (in the case of weakly acid cationic exchange resin) is a hard, insoluble resin which may be formed into tiny beads. Since the molecular network contains pendant phenyl groups (from the styrene group) these may undergo electrophilic substitution reactions and thus produce functionalised polymers [13]. Many chemical reactions may in fact be carried out on these functional groups which are attached to the cross linked net of polymers. Such a substance is called ion exchange resin. Typical examples are strongly acidic cation exchange resins (SAC). Here the polymer is sulphonated and an insoluble resin is resulted with sulphonyl group attached to it. Similarly, there are weak acid cation exchange resin, the acrylic polymers, cross-linked with divinyl benzene are functionalised with carboxylic exchange groups. The gel type resins are characterized by interstitial nanochannels while macroporous resins possess discrete open pores. The availability of exchange sites within the matrix is an added attraction and hence insitu preparation of these particles within the pores /channels is possible.

Metal nanoparticles of nickel and iron were incorporated in the ion exchange resin matrix by reducing the exchanged metal cations in the ion exchange resins. Two types of ion exchange resins, gel type strongly acidic cation exchange resin and macroporous weakly acidic cation exchange resin were employed for the production of composites. The synthesis procedure is long since

it involves repeated loading-reduction cycles so that yield of the metal can be enhanced by repeating the process under similar conditions [14-15]. The preparation of these composites is illustrated with appropriate schematic diagram in chapter 6.

2.2 Structural Characterisation

2.2.1 X-Ray Diffraction Analysis

X-ray diffraction patterns have been widely used in nanoparticle research as a primary characterisation technique for obtaining features like crystal structure, crystallite size, lattice constants and strain.

In XRD a collimated beam of X-ray with a wavelength of 1.5406Å is incident on a specimen and is diffracted by the crystalline planes in the specimen according to the Bragg's law [16]

$$n\lambda = 2dSin\theta \qquad (2.1)$$

where λ is the wavelength of the X-radiation, n is an integer, d is the spacing between atomic planes in the crystalline planes and θ is known as diffraction angle. The intensity of the diffracted x-rays was measured and plotted as a function of diffraction angle 2θ. From the 2θ values of the peaks, the lattice spacing (d) values are calculated using the equation (2.1). The lattice parameter 'a' was then computed by assuming cubic symmetry and combining equations (2. 1) and (2. 2).

$$d_{hkl} = \frac{1}{\sqrt{\frac{h^2}{a^2} + \frac{k^2}{b^2} + \frac{l^2}{c^2}}} \qquad (2.2)$$

when a = b = c, $\qquad d_{hkl} = \frac{a}{\sqrt{h^2 + k^2 + l^2}} \qquad (2.3)$

Sample identification can be easily done by comparing the experimental pattern to that in the International Centre for Diffraction Data (ICDD) file. Except

for single crystalline particles, the randomly oriented crystals in nanoparticles cause broadening of the diffraction patterns The effect becomes more pronounced, when the crystallite size is of the order of few nanometers. The simplest and most widely used method for estimating crystallite size is from the Full Width at Half Maximum (FWHM) of a diffraction peak by Debye-Scherrer formula [17].

$$D = \frac{0.9\lambda}{\beta \cos\theta}$$
(2.4)

where 'D' is the crystallite size, λ is the wavelength of the X-radiation, β is the angular width (in radians) which is equal to the (FWHM). Rigaku Dmax– C, X-ray Powder Diffractometer was used here to obtain the X-ray diffraction pattern of the samples using Cu Kα lines.

2.2.2 Transmission Electron Microscopy (TEM)

Transmission Electron Microscopy is a straight forward technique to determine the size and shape of the nanostructured materials as well as to obtain structural information. In TEM, electrons are accelerated to 100KeV or higher projected on to a thin specimen by means of a condenser lens system, and penetrate in to the sample [18]. TEM uses transmitted and diffracted electrons which generates a two dimensional projection of the sample. The principal contrast in this projection or image is provided by diffracted electrons. In bright field images the transmitted electrons generate bright regions while the diffracted electrons produce dark regions. In dark field image the diffracted electrons preferentially form the image. In TEM, one can switch between imaging the sample and viewing its diffraction pattern by changing the strength of the intermediate lens. The greatest advantage that TEM offers are the high magnification ranging from 50 to 10 [6] and its ability to provide both image and diffraction information from a single sample.

The high magnification or resolution of TEM is given by

$$L = \frac{h}{\sqrt{2mqV}} \qquad (2.5)$$

where m and q are the electron mass and charge, h the Planck's constant and V is the potential difference through which the electrons are accelerated.

The schematic of a transmission electron microscope is shown in figure (2.1). From the top down, the TEM consists of an emission source, which may be a tungsten filament, or a lanthanum hexaboride (LaB_6) source.
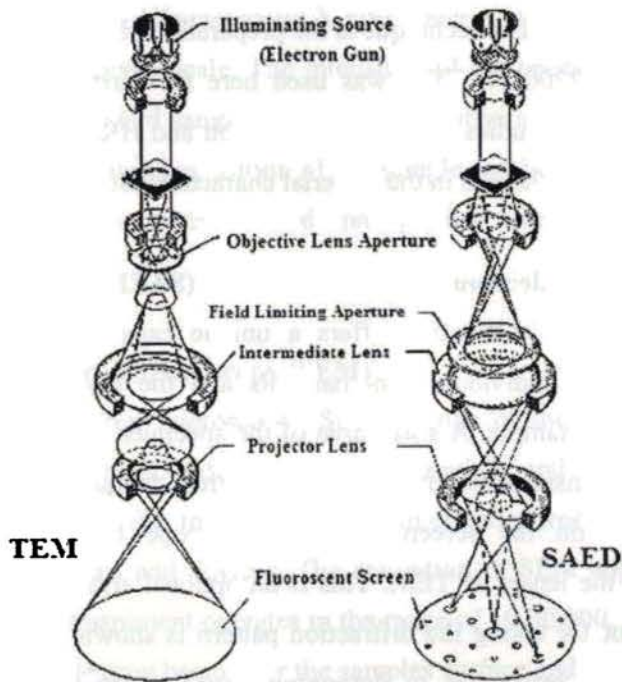

Figure 2.1 Transmission Electron Microscope for imaging and Selected Area Diffraction Pattern

Typically a TEM consists of three stages of lensing. The stages are the condenser lenses, the objective lenses, and the projector lenses. The condenser lenses are responsible for primary beam formation, whilst the objective lenses focus the beam down onto the sample itself. The projector lenses are used to

expand the beam onto the phosphor screen or other imaging device, such as film. The magnification of the TEM is due to the ratio of the distances between the specimen and the objective lens' image plane imaging systems in a TEM consist of a phosphor screen, which may be made of fine (10-100μm) particulate zinc sulphide, for direct observation by the operator. Optionally, an image recording system such as film based or doped YAG screen coupled CCD's. High resolution transmission electron microscope (HRTEM) [19] can generate lattice images of the crystalline material allowing the direct characterisation of the samples atomic structure. The resolution of the HRTEM is 1nm or smaller. However, the most difficult aspect of the TEM technique is the preparation of samples.

Joel JEM-2200 FS TEM was used here for carrying out the different electron microscopic studies. Electron Diffraction and HRTEM images obtained along with the images helped in the material characterisation to great extent.

2.2.3 Selected Area Electron Diffraction Pattern (SAED)

Selected area diffraction offers a unique capability to determine the crystal structure of individual nanomaterials and the crystal structure of the different parts of a sample. A small area of the specimen can be selected from a high resolution transmission image and its electron diffraction pattern (rings or spots) produced on the screen of the microscope by making appropriate arrangement in the lenses of TEM. This is an optional arrangement in HRTEM. The arrangement for taking the diffraction pattern is shown in figure (2.1). The SAED allows the researcher to determine lattice constant of the crystalline material which can help in species identification. Basically diffraction patterns are distinguishable as spot patterns resulting from single crystal diffraction zones or ring patterns are obtained from the randomly oriented crystal aggregates (polycrystallites). For nanocrystallites, the diffraction patterns will be a diffused ring patterns. The 'd' spacing between lattice planes can be estimated radius r of the diffracted rings from the relation $\lambda L = rd$, if the camera constant λL is

known .The estimation of d values enable us to describe the crystal structure of the crystalline specimen [20-21].

2.2.4 Energy Dispersive X-ray Spectroscopy (EDS)

Energy dispersive X-ray spectrometer (EDS) attached to the transmission electron microscope analyses characteristic X-ray radiation emitted from the specimen when the electron beam interact with the specimen. The main use of EDS is to accurately determine the composition of the sample under investigation. Upon exposing the samples to high energy electron beams the various atoms present in the sample emit characteristic X-rays which can be observed as several distinct peaks on an energy scale. The intensities of the peaks can be compared with the peaks of a standard sample to obtain the relative amounts of each atomic species, whereby accurate composition of the sample can be determined. The use of EDS has been demonstrated in oxide nanoparticle research in a number of reports [22-23].

2.2.5 Scanning Electron Microscopy (SEM)

Scanning electron microscopy (SEM) is one of the most widely used techniques used in characterisation of nanomaterials and nanostructures. It provides the image of the morphology and microstructures of the bulk and nanostructured materials and devices. The resolution of SEM approaches a few nanometers and the instrument operates in the range of 10-30,000. SEM is carried out by scanning an electron beam over the samples surface and detecting the yield of low energy electrons (secondary electrons) and high energy electrons (backscattered) according to the position of the primary beam. The secondary electrons which are responsible for the topological contrast provide mainly information about the surface morphology. The backscattered electrons which are responsible for the atomic number contrast carry information on the samples composition [18, 24]. A new generation of SEM has emerged and is an important

tool to characterize nanostructured materials. In this SEM, Field Emission Gun provides the electron beam and the resolution is as high as 1 nm.

JSM-6335 FESEM Scanning Electron Microscope was employed to check the morphology of our samples.

2.2.6 Fourier Transform Infrared Spectroscopy (FTIR)

Vibrational motion of chemical bonds occurs in the infrared region of the energy beam. The Fourier Transform Infrared Spectroscopy exploits this phenomenon. When a sample is exposed to IR energy, this energy couples with the energy of the sample. If the impinging IR energy is in resonance with the energy of the chemical bond in the sample the intensity of the beam is measured before and after it interacts with the sample. The incident radiation can be detected in transmission or reflection experiments. The intensity is then plotted as a function of the frequency in the IR spectrum [25]. Thus infrared spectroscopy is a useful technique for characterizing materials and obtaining information on the molecular structure, dynamics and environment of a compound. In an infrared spectrum, the absorption or transmittance peaks correspond to the frequencies of vibrations between the bonds of the atoms making up the material. From the characteristic peaks, different functional groups present in the compound can be identified. This aspect makes infrared spectroscopy quite useful in material characterisation. FTIR spectra of the samples were taken using Thermo Nicolete Avatar DTGS model spectrophotometer.

2.2.7 Inductively Coupled Plasma-Atomic Electron Spectroscopy (ICP-AES)

Elemental analysis of the samples was carried out with the help of Inductively Coupled Plasma-Atomic Electron Spectroscopy. Thermo Electron Corporation, IRIS INTREPID II XSP model was used for ICP measurement. This is a very powerful tool for elemental analysis up to the parts per million (ppm) levels. In this method, a plasma or gas consisting of ions, electrons and neutral

particles are formed from an Argon gas. The plasma is used to atomize and ionize the elements in a sample. The resulting ions are then passed through a series of apertures (cones) into the high vacuum mass analyzer. The elements are identified by their mass-to-charge ratio (m/e) and the intensity of a specific peak in the mass spectrum is proportional to the amount of that element in the original sample [26].

2.2.8 Atomic Force Microscopy (AFM)

In atomic force microscopy, the microscope can image surfaces with atomic resolution by scanning a sharp tip across the surface at forces smaller than the forces between atoms. A cantilever with the attached stylus is sandwiched between the AFM sample and the tunneling tip. It is fixed to a small piezoelectric element called the modulating piezo which is used to drive the cantilever beam at its resonant frequency. Commercially available silicon tip was used in all studies [27]. The interatomic forces between the tip and the sample surface atoms cause the cantilever to deflect. The AFM sample is connected to a three dimensional piezoelectric drive. A feedback loop is used to keep the force acting on the stylus at a constant level. The cantilever displacement is measured by a deflection sensor. Typically sensors can detect deflections as small as 1 Å. Measuring the deflection of the cantilever while the tip is scanned over the sample allows the surface topography to be mapped [28-29]. The evident advantage of AFM is that it is applicable for studying all types of surfaces, conducting, semiconducting and insulating.

Tapping mode AFM is of particular interest in determining topography and phase morphology of materials. Three types of tapping mode data are height data mode, phase data mode and amplitude data mode. Height data is a good measure of the height of surface features but does not show distinct edges of these features. Phase data mode monitors the change in phase offset, or phase angle, of the input drive signal [to the drive piezo] with respect to the phase offset of the oscillating cantilever. The phase offset between the drive signal and detector

signal is defined as zero for the cantilever oscillating freely in air. The changes in phase offset due to differing amounts of damping experienced by the probe tip as it rasters across the sample surface are plotted as the so-called 'phase image'. In the amplitude mode the amplitude of the cantilever is monitored by the photo diode detector. These values are plotted as an amplitude map of the sample surface [29].

2.3 Magnetic Characterisation

2.3.1 Vibrating Sample Magnetometer (VSM)

A vibrating sample magnetometer (VSM) operates on Faraday's Law of induction, which tells us that a changing magnetic field will produce an electric field. This electric field can be measured and provides us information about the changing magnetic field. A VSM is used to measure the magnetic behaviour of magnetic materials. Using VSM the hysteresis loop parameters namely saturation magnetisation (M_s), coercive field (H_c), remanence (M_r) and squareness ratio (M_r/M_s) can be derived. The schematic of a vibrating sample magnetometer is given in figure (2.2).

In a VSM, the sample to be studied is placed in a constant magnetic field. If the sample is magnetic, this constant magnetic field will magnetize the sample by aligning the magnetic domains or the individual magnetic spins, with the field. The stronger the constant field, the larger the magnetisation. The magnetic dipole moment of the sample will create a magnetic field around the sample, sometimes called the magnetic stray field. As the sample is moved up and down, this magnetic stray field change as a function of time and can be sensed by a set of pick up coils. A transducer converts a sinusoidal ac drive signal provided by a circuit located in the console in to a sinusoidal vertical vibration of the sample rod and the sample is thus made to undergo a sinusoidal motion in a uniform magnetic field. Coils mounted on the pole pieces of the magnet pick up the signal resulting from the sample motion.

60
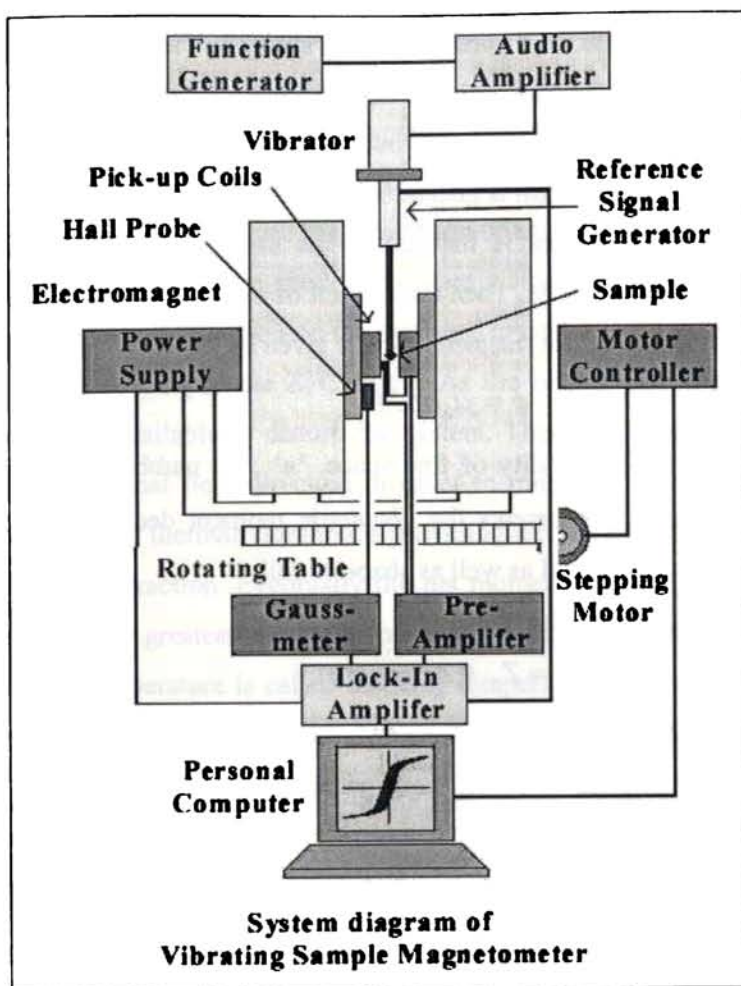
Figure 2.2 Vibrating Sample Magnetometer

The alternating magnetic field will cause an electric field in the pick up coil as according to Faradays law of induction, the current will be proportional to the magnetisation of the sample. The greater the magnetisation, the greater the induced current. The induction current is amplified by a transimpedence amplifier and a lock-in amplifier. The various components are interfaced via a computer. Controlling and monitoring software, the system can tell you how much the

sample is magnetized and how magnetisation depends on the strength of the constant magnetic field. For particular field strength, the corresponding signal received from the probe is translated into a value of magnetic moment of the sample. When the constant field varies over a given range, a plot of magnetisation versus magnetic field strength is generated.

The dipole moment is induced in the sample when it is placed in a uniform magnetic field be M. Then the amount of magnetic flux linked to the coil placed in the vicinity of this magnetic field is given by

$$\phi = \mu_0 n \alpha M \tag{2.6}$$

where 'μ_0' is the permeability of free space, 'n' the number of turns per unit length of coil and $\propto$ represents the geometric moment decided by position of moment with respect to coil as well as shape of coil.

Anharmonic oscillator of the type,

$$Z = Z_0 + A \exp(j\omega t) \tag{2.7}$$

induces an emf in the stationary detection coil. The induced emf is given by

$$V = -\frac{d\phi}{dt} = -j\omega\mu_0 n M A \left(\frac{\partial \alpha}{\partial z}\right) e^{j\omega t} \tag{2.8}$$

If amplitude of vibration (A), frequency ω and $\frac{\partial \alpha}{\partial z}$ are constant over the sample zone then induced voltage is proportional to the magnetic moment of the sample. A cryogenic setup attached to the sample permits low temperature measurements. This is the basic idea behind VSM [30-32]

The magnetisation measurements (hysteresis loop) were carried out employing DMAX VSM. The magnetisation isotherms over a wide temperature range were taken for MCE measurements.

2.3.2 Field Cooled and Zero Field Cooled Measurements

Zero Field Cooled (ZFC) measurements provide a means of investigating various magnetic interactions. First a sample is cooled to liquid helium

temperatures under zero applied magnetic fields. Then small uniform external filed is applied and the net magnetisation is measured while heating the sample at a constant rate. For small magnetic particles, this curve has a characteristics shape. As the particle cools in a zero applied magnetic field, they will tend to magnetise along the preferred crystal directions in the lattice, thus minimizing the magneto-crystalline energy. Since the orientation of each crystallite varies, the net moment of the systems will be zero. Even when a small external field is applied the moments will remain locked into the preferred crystal directions, as seen in the low temperature portion of the ZFC curve. As the temperature increases more thermal energy is available to disturb the system. Therefore more moments will align with the external field direction in order to minimize the Zeeman energy term. In other words, thermal vibration is providing the activation energy required for the Zeeman interaction. Eventually the net moment of the system reaches a maximum where the greatest population of moments has aligned with the external field. The peak temperature is called blocking temperature T_B which depends on particle volume. As temperature rises above T_B, thermal vibrations become strong enough to overcome the Zeeman interaction and thus randomize the moments [33].

Field cooled measurements proceed in a similar manner to ZFC except that the constant external field is applied while cooling and heating. The net moment is usually measured while heating. However, the FC curve will diverge from the ZFC curve at a point near the blocking temperature. This divergence occurs because the spins from each particle will tend to align with the easy crystalline axis that is closest to the applied field direction ad remain frozen in that direction at low temperature. Thermal Remnant Magnetisation (TRM) curves are obtained by cooling field to the measurement start temperature. The field is then removed and the magnetisation is recorded as a function of temperature while the sample is heated. It is important to note that ZFC, FC and TRM are non equilibrium measurements [34-35]. Care must be taken to ensure the same heating

rate is used during the measurements in order to properly compare the measurements.

In the present investigation, FC-ZFC modes of the VSM (Oxford Instruments) were employed for the measurements. In the ZFC mode, the sample was cooled in the absence of a field and the magnetisation was measured during warming, by applying a nominal field of 200Oe- 500 Oe. In the FC mode, the sample was cooled in presence of a field and the magnetisation was measured during warming, under the field of 200Oe- 500Oe.

2.4 Electrical Characterisation

2.4.1 DC Conductivity Measurements

The dc conductivity of the sample was measured using a Keithley 236 Source meter. In this set up the sample is considered as a resistance. Across the sample a voltage was applied and corresponding current was noted. Using Ohm's law the resistance was calculated. From the resistance R, the resistivity was found out using the expression,

$$R = \frac{\rho l}{A} \tag{2.9}$$

where ρ is the resistivity, l is the thickness of the pellet and A is the area of cross section of the pellet[34]. But conductivity σ is the reciprocal of resistivity. Thus dc conductivity was calculated. The same procedure was repeated for currents corresponding to different temperatures. The data acquisition was automated with the help of, a virtual instrumentation package. This package is called LabVIEW, a base software package developed by National Instruments for implementing virtual instrumentation and G programming. LabVIEW is a programming language for data acquisition, analysis, simulation or computer control of instruments and techniques or processes. Appropriate modifications were incorporated in the software so as to enable the data acquisition automatic and visual observation of the graphs on the computer screen. The characteristic feature of this automatic data acquisition is that it has been possible to acquire 20,000

data points or more in a matter of 5 to 10 minutes. By using the modified package, the data can be plotted and analysed.

2.4.2 Dielectric Measurements

The samples for dielectric measurement were pressed by applying a pressure of 5 tones to get compact circular pellets with dimensions 12mm in diameter and approximately 0.5mm to 2 mm in thickness. The LCR meter is compactable with such dimension of the pellets.
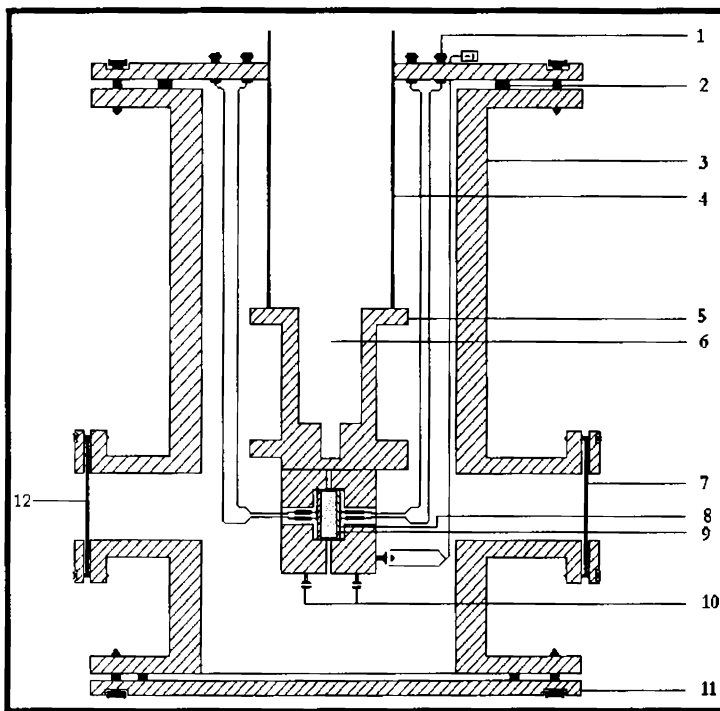
1. BNC	2. Neoprene O ring
3. MS Chamber	4. SS Pipe
5. Sample Holder	6. Liquid Nitrogen Cavity
7. Glass Window	8. Metal Electrodes
9. Sample	10. Heating Filament
11. MS Flange	12. To Vacuum Pump

Figure 2.3 Cell for the dielectric and conductivity measurements

The capacitance, loss factor, dielectric constant and ac conductivity were measured with frequency ranging from 100 KHz to 8 MHz. This was repeated at different temperature from 30°C to 120°C in steps of 10°C. The sample temperature is controlled by a temperature controller and the temperature on the sample is sensed by an Iron-Constantan (Fe-K) thermocouple on the sample. The schematic design of the cell employed for the electrical measurements is given in figure (2.3).

The cell is made up of mild steel with a cylindrical stem having provisions for fixing various attachments such as electrical connections and vacuum gauges. The cell is connected to a rotary pump to maintain a pressure of 10^{-2} Torr inside the chamber. The inner diameter of the cell is about 18cm, and has a length of 30cm. The sample holder is fixed at the bottom of a one-end closed metallic tube to be embedded to the top flange. For the electrical conductivity and dielectric measurements, pellets are mounted on the sample holder consisting of two copper disc electrodes in between which the palletized samples are loaded. The sample holder can be heated using a temperature-controlled heater.

The dielectric constant measurements of the samples at low and high frequencies, *viz*, from a few Hz to 8MHz were carried out by a Hewlett Packard 4192A LCR meter which is automated and controlled by a virtual instrumentation package called LabVIEW. The temperature variation studies are also carried out. The dielectric constant of the sample can be calculated using the equation,

$$\varepsilon_r = \frac{Cd}{\varepsilon_0 A} \qquad (2.10)$$

where d is the thickness of the pellet, C is the capacitance measured by LCR meter, A is the area of sandwiched structure and ε_0 is the absolute permittivity of air.

The theory involved for the evaluation of ac conductivity from dielectric constant values may be briefed as follows. Any capacitor when charged under an ac voltage will have a loss current due to ohmic resistance or impedance by heat absorption.

For a parallel plate capacitor of area of cross section A and separation d, the ac conductivity is given by the relation

$$\sigma_{ac} = \frac{J}{E} \qquad (2.11)$$

Here J is the current density and E is the field density. But we know that the electric field vector

$$E = \frac{D}{\varepsilon} \qquad (2.12)$$

where D is the displacement vector of the dipole charges, ε is the complex permittivity of the material. Also the electric field intensity (E) for a parallel plate capacitor is the ratio of potential difference between the plates of the capacitor and the inter plate distance.

$$E = \frac{V}{d} \qquad (2.13)$$

where V is the potential difference between the plates of the capacitor, d is the inter plate distance.

Since the current density $J = \frac{dq}{dt}$ and q is given by $\frac{Q}{A} = \frac{V\varepsilon}{d}$, where Q is the charge in coulombs due to a potential difference of V volts between two plates of the capacitor.

$$J = \frac{dq}{dt} = \frac{d}{dt}\left(\frac{V\varepsilon}{d}\right) = \frac{\varepsilon}{d}\frac{dV}{dt}$$

$$J = \frac{\varepsilon}{d}\frac{dV}{dt} = \frac{\varepsilon}{d}.Vj\omega \qquad (2.14)$$

Substituting for E and J from the equations (2.13) and (2.14) we get

$$\sigma_{ac} = \frac{J}{E} = \varepsilon j\omega \ ,$$

Considering ε as a complex entity of the form $\varepsilon^* \approx \left(\varepsilon' - j\varepsilon''\right)$ and neglecting the imaginary term in the conductivity we can write

$$\sigma_{ac} = \omega\varepsilon'' \qquad (2.15)$$

But the loss factor or dissipation factor in any dielectric is given by the relation

$$tan\delta = \frac{\varepsilon''(\omega)}{\varepsilon'(\omega)} \qquad (2.16)$$

Hence from the dielectric loss and dielectric constant, ac conductivity of these samples can be evaluated using the relation

$$\sigma_{ac} = 2\pi f \tan\delta\varepsilon_0\varepsilon_r \qquad (2.17)$$

where f is the frequency of the applied field and tanδ is the loss factor [35].

The ac electrical conductivity of powder samples calculated utilizing the dielectric parameters. The ac conductivity is calculated by using the relation $\sigma_{ac} = 2\pi f \tan\delta\varepsilon_0\varepsilon_r$. After obtaining capacitance and dielectric loss from the instrument, LabVIEW software first calculates the dielectric constant and then evaluates the ac conductivity.

2.4.3 Cole-Cole Plot

In order to study the dielectric behaviour, it is customary to plot $\varepsilon', \varepsilon''$ or $tan\delta$ against frequency. A more convenient method is the Argand diagram or complex locus diagram in which the imaginary part of the complex dielectric constant is plotted against the real part at the same frequency. Kenneth S. Cole and Robert H. Cole applied this method to dielectric and hence it is often called Cole-Cole plot [36-39]. For a dielectric with single relaxation time, the Cole-Cole plot is a semicircle with its center on the real axis and intercepts at ε_0 and ε_∞ on this axis.

From figure 2.4, we can write

$$u + v = \varepsilon_s - \varepsilon_\alpha \qquad (2.18)$$

where the quantities u, v considered as vectors in the complex plane are perpendicular, their vector sum being the constant real quantity $(\varepsilon_s - \varepsilon_r)$.
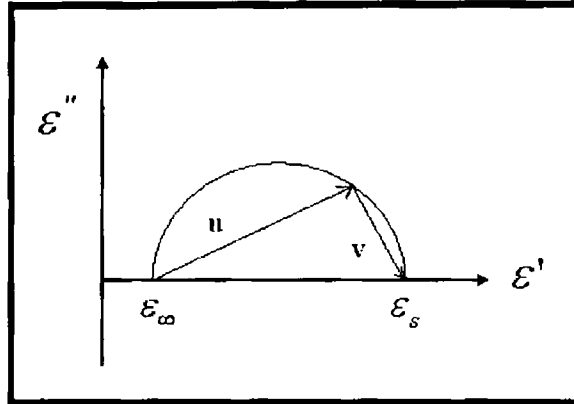
Figure 2.4 Cole-Cole Plot

The right angle included by these vectors is therefore inscribed in a semicircle of diameter ($\varepsilon_s - \varepsilon_\infty$) as shown in the figure (2.4). This semicircle is then the locus of the dielectric constant as ω varies from 0 to ∞.

But,

$$\varepsilon^* - \varepsilon_\infty = \frac{(\varepsilon_s - \varepsilon_\infty)}{(1 + j\omega\tau)} \qquad (2.19)$$

and therefore,

$$u + v = (\varepsilon^* - \varepsilon_\infty)(1 + j\omega\tau) \qquad (2.20)$$

Many materials, particularly long chain molecules and polymers shows a broader dispersion curve and lower maximum loss than would be expected from the Debye's relationship. K.S Cole and R.H Cole suggested that in this case the permittivity might follow the empirical relation,

$$\varepsilon^* - \varepsilon_\infty = \frac{(\varepsilon_0 - \varepsilon_\infty)}{1 + (j\omega\tau_0)^{1-\alpha}} \qquad (2.21)$$

69

where τ_0 is the average relaxation time and α is the spreading factor $(0 \leq \alpha \leq 1)$ of actual relaxation time τ about its mean value τ_0.

For $\alpha = 0$ the above equation reduces to Debye's equation. The center of the circular arc lies below the real axis and when $\alpha = 0$ the above expressions become consistent with Debye's model. From the expression for ε'', it is clear that at $\omega = 1/\tau$, it becomes maximum and the value is given by

$$\varepsilon''_{max} = \frac{(\varepsilon_0 - \varepsilon_\infty)\tan[(1-\alpha)\pi/4]}{2} \qquad (2.22)$$

From the Cole-Cole plot, the dispersion parameters like static dielectric permittivity, optical dielectric permittivity, the spreading factor α can be evaluated [40].

2.5 Magnetocaloric Measurements

The characteristic magnetocaloric (MCE) values, the isothermal magnetic entropy change (ΔS_m) and adiabatic entropy change (ΔT_{ad}) can be measured using a number of techniques. The adiabatic temperature change can be measured both directly and indirectly. But ΔS_m can be measured by indirect methods only [41-44]. The indirect technique of measuring MCE from the magnetisation data involves the numerical integration given in the equation, [45- 47]

$$\underline{\Delta S_m}(T,H) = \int_0^H \left(\frac{\partial M}{\partial T}\right)_H dH \qquad (2.23)$$

If we examine the above equation, we can find that this equation relates the entropy change with the application of an external magnetic field H, in terms of measurable quantities M, T, H. If one measures the magnetisation as a function of field at various temperatures, then ΔS_m can be approximated as [48-50].

$$\Delta Sm = \frac{1}{\Delta T}\left[\int_0^H M(T+\Delta T,H)dH - \int_0^H M(T,H)dH\right] \qquad (2.24)$$

The above equation shows that the change in entropy of a system is equivalent to the area between the two magnetic isotherms divided by the temperature difference between the isotherms. This formulation is useful for graphical or numerical calculations of ΔS_m from the magnetisation data. Thus, the magnetocaloric effect can be estimated without employing calorimetric techniques. The error involved in the measurement is found to be 3-10% [51].

References

1. J. Park, V. Privman, E. Matijevic, J. Phys. Chem. B, 105 (2001) 11630.

2. D.K. Kim, Y. Zhang, W. Voit, K.V. Rao, M. Muhammed, J. Magn. Magn. Mater. 225 (2001) 30.

3. L. Vayssières, C. Chanéac, E. Tronc J. P. Jolivet, J. Colloid Interface Sci. 205 (1998) 205

4. E. Auzans, D. Zins, E. Blums, R. Massart, J. Mater. Sci. 34 (1993) 1253.

5. R Massart, E. Dubois, V Cabuil, E Hasmonay, J. Magn. Magn. Mater. 149 (1995) 1

6. A. C. Pierre, Ceram. Bull. 70 (1991)1281

7. B. Stahl, N.S Gajbhiye, G. Wilde, D.Kramer J.Ellrich, M.Ghafari, H Hahn, H.Gleiter, J.Weibmuller, R. Wurshum, P.Schlossmacher, Adv. Mater. 14 (2002) 24

8. D.H Chen, X.R He, Mater. Res. Bull. 36 (2001)1369

9. K P Jayadevan, T.Y.Tseng, *Encyclopedia of Nanoscience and Nanotechnology*, H.S Nalwa (editor) 8 (2004) 333

10. Pomogailo. A.D, Dzhardimalieva. G.I, Rozenberg. A.S, Muraviev. D. J. Nanopart Res. 5 (2003) 497.

11. Santini.O, Mosca. D.H, Schreiner. W.H, Marangoni. R.; Guimaraes. J.L, Wypych. F; A.J.A. Oliveira , J. Phys. D: Appl. Phys. 36 (2002) 428.

12. Ziolo. R.F, Giannelis. E.P, Weinstein. B.A, O'Horo. M.P; Ganguly.B.N, Mehrotra. V, Russell. M.W, Huffman. D.R, Science 257 (1992) 219.

13. http://www.sigmaaldrich.com/aldrich/brochure/al_pp_ionx.pdf

14. Malini K.A, Anantharaman. M.R, Sindhu. S, Chinnasamy. C.N, Ponpandian. N, Narayanasamy. A, Balachandran. B, Shivasankarapillai. V.N, J. Mater. Sci. 36 (2001) 821.

15. Swapna Nair S, Mercy Mathews, Joy. P.A, Kulkarni. S.D, Anantharaman.,M.R, J. Magn. Magn. Mater. 283 (2004), 344.

16. Charles Kittel, *Introduction to Solid State Physics*, John Wiley and Sons, New York (1997).

17. B.D. Cullity, *Elements of X-ray diffraction*, Philippines, Addison-Wesley Publishing Company, Inc., 2nd Edition. California (1978).

18. M. Watt, *The Principles and Practice of Electron Microscopy*, 2nd Edition, Cambridge University Press, Cambridge (1997).

19. A. Subramanian, L.D. Marks, Ultramicroscopy, 98 (2004) 151.

20. C.T. Schamp, W.A. Jesser, Ultramicroscopy, 103 (2005) 165

21. Lawrence E Murr, *Electron and Ion Microscopy and Microanalysis, Principles and Applications*, Mc.Graw Hill Inc.New York,1982.

22. C.H. Lin, P.C. Kuo, J. L. Pan, D. R. Huang, J. Appl. Phys. 79(1996) 6035.

23. X. Xu, G. Freidman, K. D. Humfeld, S. A Majetich,S A. Asher, Chem. Mater.14 (2002)1249.

24. Linda C. Sawyer and David T. Grubb, *Polymer Microscopy*, 2nd Edition. Chapman and Hall, London (1987).

25. Brian Smith, *Infrared Spectral Interpretation-A systematic Approach*, CRC Press, Boca Raton, London, New York, Washington D C, (1999).

26. Joachim Nölte, *ICP Emission Spectrometry: A Practical Guide*, Wiley-VCH Verlag GmbH & Co, KGaA, Weinheim (2003)

27. Jamshid. K. Avlyanov, Jack. Y. Josefowicz,, Alan G Mac Diamid, Synthetic Metals 73(1995) 205.

28. G. Binning, C.F Quate , Ch. Gerber, Phy. Rev. Lett. 56 (1986) 930

29. K. Oura, V.G Lifshits, A. A Saranin, A.V Zoto, M Katayama, *Surface Science-an Introduction*, Springer Verlag, Berlin, Heidelberg, Germany (2003)

30. Simon Foner, Rev. Sci. Instrum., 30 (1959) 548.

31. Joseph A. Pesch, Rev. Sci. Instrum., 54 (1983) 480.

32. R.V. Krishnan and A. Banerjee, Rev. Sci. Instrum., 70 (1999) 85.

33. J. C. Denardin, A. L. Brandl, M. Knobel, P. Panissod, A. B. Pakhomov, H. Liu, X. X. Zhang; Phys. Rev. B 65, 064422 (2002)

34. Aparna Roy ,V. Srinivas, S. Ram, J. A. De Toro, J. Appl. Phys. 100 (2006) 094307

35. J.L Dormann, D Fiorani, J. Magn. Magn. Mater. 140-144 (1995) 415.

36. Debye P 1929, *Polar Molecules* (New York: Dover)

37. Cole K.S and Cole R.H, J. Chem. Phys. 9 (1941) 34

38. Veera V. Daniel, *Dielectric Relaxation* (London: Academic) 1967

39. Hill N.E, Vaughan W. E, Price A. H and Mansel Davies, *Dielectric properties and Molecular Behavior*, London: Van Nostrand Reinhold,1969

40. S Sagar S Saravanan S Suresh Kumar S Venkatachalam M R Anantharaman J. Phys. D: Appl. Phys. 39 (2006) 1678

41. K. A. Gschneidner, Jr. and V. K. Pecharsky , Annu. Rev. Mater. Sci. 30(2000) 387.

42. M. Foldeaki W. Schnelle, E. Gmelin, P. Benard, J. Appl. Phys. 82, 309 (1997);

43. J. R. Sun, F. X. Hu, B.G. Shen, Phys .Rev. Lett 85 (2000) 4191.

44. M. Földeàki, R. Chahine, T. K. Bose , J. App. Phys.77 (1995)3528

45. A H Morrish, The Physical Principles of Magnetism, Wiley &Sons ,NewYork (1965)

46. R P Hudson, *Principles and Applications of Magnetic Cooling*, North Holland Publishing company, Amsterdam, London (1972)

47. Herbert B Callen, *Thermodynamics* (Wiley , New York)

48. K. A. Gschneidner, Jr., V .K. Pecharsky, Mater. Sci. Eng. A 287, (2000), 301.

49. R. D.McMichael, J J Ritter, R D shull, J. App. Phys. 73 (1993) 6946

50. K .A. Gschneidner, Jr. , V. K. Pecharsky, Phys. Rev. Lett. 78 (1997)4494

51. V. K. Pecharsky, K .A. Gschneidner Jr., J. Mag. Mag. Mater. 200 (1999) 47

Synthesis of $Mn_{1-x}Zn_xFe_2O_4$ Nanoparticles and Evaluation of the Magnetic and Structural Parameters

$Mn_{1-x}Zn_xFe_2O_4$ nanoparticles (x=0 to 1) were synthesized by wet chemical co-precipitation techniques. X-Ray Diffraction, Transmission Electron Microscopy and High resolution Transmission Electron microscopy were effectively utilized to investigate the different structural parameters. The elemental analysis was conducted using Energy Dispersive Spectrum and Inductively Coupled Plasma Analysis. The magnetic properties such as magnetization and coercivity were measured using Vibrating Sample Magnetometer. The observed magnetization values of the nano particles were found to be lower compared to the bulk counterpart. The maximum magnetization values showed a gradual decrease with zinc substitution except for a small increase from x=2 to x=0.3. The Curie temperature of the compositions was evaluated from the temperature dependence of magnetization. The Curie temperature was found to be enhanced in the nanoparticles in comparison with bulk. The zero field cooled (ZFC) curve showing a blocking at 53K for $MnZnFe_2O_4$ proclaims the superparamagnetic nature of the composition. The magnetic anisotropy in the superparamagnetic nanoparticles is also analysed. The variation in lattice constant, reduced magnetization values, variant of maximum magnetization with zinc substitution, the presence of a net magnetic moment for the zinc ferrite and the enhancement in Curie temperature in $Mn_{1-x}Zn_xFe_2O_4$, all point to the existence of a metastable cation distribution together with surface effects at the nanoregime.

Manganese zinc ferrites belong to the class of spinel ferrites. The equilibrium distribution of cations in the bulk structure is influenced by a number of factors namely ionic radii, ionic charge, lattice energy, octahedral site preference energy and crystal field stabilization energy [1]. For example, in the coarser regime, Zn^{2+} has a strong preference for tetrahedral sites while Ni^{2+} exhibits a strong octahedral preference in spinel ferrites. Cations like Mn^{2+}/Mn^{3+} are found to be influencing the magnetic, structural and electrical properties considerably. In the nanoregime, in the case of spinel ferrites, there are distinct deviations in magnetic properties with respect to their bulk counterparts [2- 5]. However the role of cations *vis a vis* their occupancy of octahedral sites instead of tetrahedral sites is still not clear as regards their influence in deciding the overall magnetic properties of these materials in the nanoregime. It is in this context that a study of nanosized manganese zinc mixed ferrites with varying concentration of zinc assumes significance. Ferrites belonging to the series $Mn_{1-x}Zn_xFe_2O_4$ (for x=0, 0.1, 0.2...1) provides an ideal platform to check various hypotheses. Moreover the role of Jahn-Teller ions like Mn^{3+}/Mn^{4+} can also be investigated in influencing the overall magnetic properties of mixed ferrites.

When ascertaining the role of cations, the knowledge of exact stoichiometry is important in the case of mixed ferrites belonging to a series of this type. The exact and prior determination of various ions in the compositions also provides valuable inputs in ascertaining the distribution of cation between sites. So compositional analysis using techniques like ICP/EDS enables one to determine the exact composition of the synthesised series. This will enable to determine deviations from expected stiochiometry and is vital in arriving at the exact cation d' 'ribution in the case of nanosized manganese zinc ferrites. Many researchers have ignored this aspect and their conclusions are often misleading and erroneous, especially, if cation distribution is the deciding factor in determining the overall magnetic properties of the materials in the nanoregime.

In the bulk, $MnFe_2O_4$ is found to be 20% inverse with a stoichiometry of $Mn_{0.8}Fe_{0.2}[Mn0.2\ Fe_{0.8}]O_4$ where cations in brackets occupy octahedral sites [6]. A higher inversion up to 60% has been reported in nanosized manganese ferrite [7]. When zinc is substituted for manganese in $Mn_{1-x}Zn_xFe_2O_4$, the zinc ions are expected to occupy the tetrahedral sites. In ceramic samples the zinc ions were found to exist only in the tetrahedral sites (A sites) as expected. However zinc is found to occupy octahedral sites in the case of nanosized manganese zinc ferrites when they are prepared by co-precipitation methods, or pulsed laser deposition method or high energy ball milling method [8-9]. The occupancy of zinc ions in octahedral sites in the nanoregime can alter the expected cation distribution to a great extent and will result in modified structural and magnetic properties in the case of $Mn_{1-x}Zn_xFe_2O_4$ nanoparticles.

3.1 Synthesis

Mixed ferrites belonging to the series $Mn_{1-x}Zn_xFe_2O_4$ (x=0 to 1) nanoparticles were synthesized by wet chemical co-precipitation. Aqueous solutions of (1-x) M manganese chloride ($MnCl_2.4H_2O$) and x M (x is the molar concentration of zinc) zinc chloride ($ZnCl_2$.anhydrous) and 2M solution of ferric chloride ($FeCl_3$.anhydrous) were mixed to form a solution. This mixture solution was poured quickly into boiling 10M NaOH solution diluted in 1800 ml of water under vigorous stirring. The formation of precipitate was found to be in the pH range, of 12.5-13. The solution was kept at 90^0C for 40 minutes under vigorous stirring. The precipitate was washed several times with distilled water, then filtered and dried in oven.

3.2 Structural Properties

The X-ray diffraction patterns of all the compounds belonging to the series $Mn_{1-x}Zn_xFe_2O_4$ (for x=0 to 1) series is shown in figure (3.1). The patterns are characteristic of an inverse spinel structure without any traces of detectable

impurity (figure 3.2). The size of the particles as evaluated by Debye Scherer's equation lies within the range 7-29 nm.
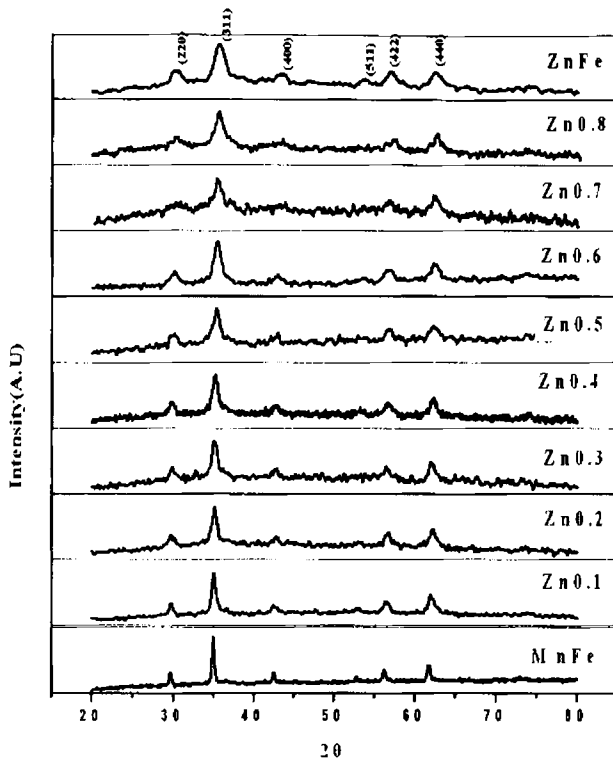
Figure 3.1 XRD Patterns of the series $Mn_{1-x}Zn_xFe_2O_4$ for different Zn substitution (x)

(a)

(b)
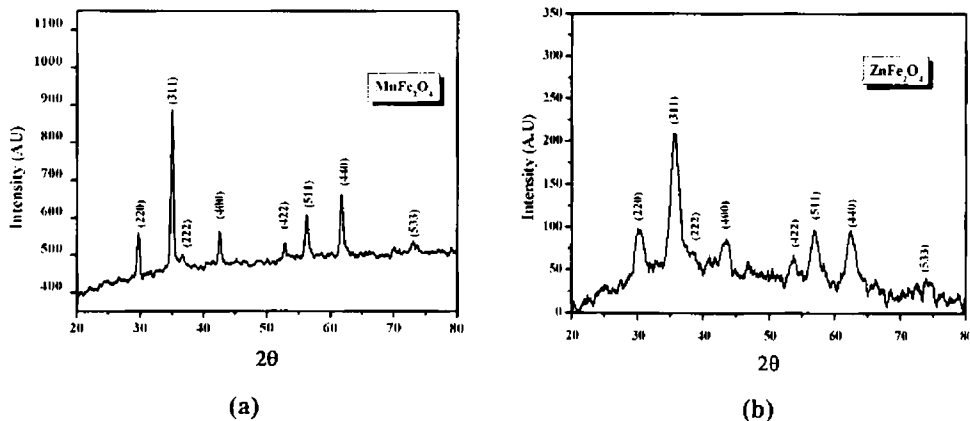
Figure 3.2 XRD Patterns of $MnFe_2O_4$ and $ZnFe_2O_4$

Further the variation of particle size with zinc substitution (x) was analysed and it is depicted in figure 3.3.
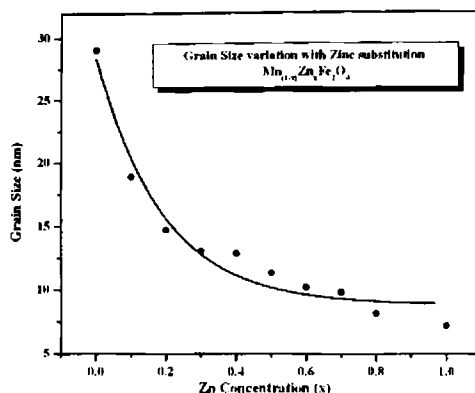
Figure 3.3 Variation of Grain Size with Zinc Concentration

It can be seen that for small amounts of zinc incorporation there is a sharp and significant decrease in particle size while for higher concentration of zinc, the decrease in particle size is less pronounced. It may be noteworthy that Arulmurugan *et.al.* [10] noticed a linear trend in the variation of particle size and lattice parameter of nanosized $Mn_{1-x}Zn_xFe_2O_4$ mixed ferrites. It is to be construed here that an increase in zinc concentration in the solution during synthesis increases the reaction rate which favours the formation of ultrafine particles of mixed ferrites. The difference in average particle size between the extremes (for x=0 and x=1) was found to be approximately 20nm which is quite significant. This accounts the role of zinc substitution in reducing the particle size of the series.

The lattice parameter of all the compositions in the series $Mn_{1-x}Zn_xFe_2O_4$ mixed ferrites was evaluated after assuming cubic symmetry. The variation of lattice parameter with zinc concentration is depicted in figure 3.4. A similar type of variation is also observed in bulk $Mn_{1-x}Zn_xFe_2O_4$ which is attributed to the substitution of bigger sized Mn^{2-} cations (0.091nm) by Zn^{2+} cations having

smaller radii (0.082nm) for bigger. However a relative contraction of the lattice is observed with respect to bulk for the same composition(x) [11].
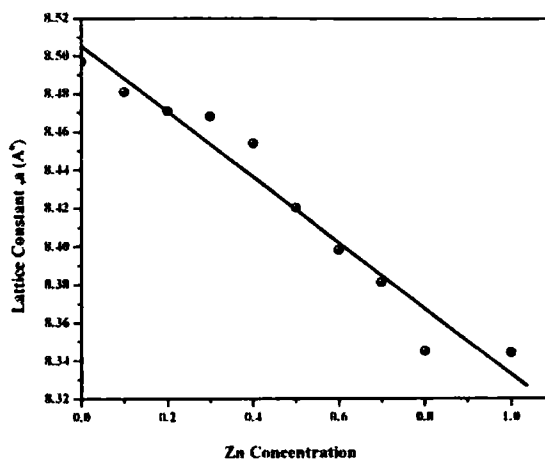
Figure 3.4 Variation of lattice constant with zinc concentration

In the case of bulk $Mn_{1-x}Zn_xFe_2O_4$, the presence of Mn^{2+}/Mn^{3+} ions and the volatilization of zinc were believed to be contributing to the contraction of the lattice [12]. However, chances of zinc evaporation are virtually nil since the methods adopted for the synthesis are based on co-precipitation techniques. But the chances of formation for the formation of Mn^{3+} cations during the precipitation process cannot be ruled out since Mn^{2+} is easily oxidized in a highly basic solution [13]. Since Mn^{3+} ion has a preferential occupancy for octahedral geometry, it may be accommodated in the B site. In the process, in order to maintain charge neutrality of the B Site, some Fe^{3+} ions may be converted into Fe^{2+} ions. The presence of Mn^{3+} and Fe^{2+} in octahedral site can result in the Jahn-Teller distortion of the octahedral symmetry of B sites which might lead to a lattice distortion in these mixed ferrites. This type of lattice distortion was observed in co-precipitated manganese ferrite nanoparticles [13].

High resolution transmission electron microscopy was employed to confirm the findings arrived through XRD studies (Figure 3.5-3.7). TEM images of $MnFe_2O_4$ (figure 3.5) particles exhibited truncated cubo-octahedral shapes along with spherical particles while the other two samples formed spherical nanoparticles. The reduction in particle size with zinc concentration is evident in the TEM images. The HRTEM images of the three compositions have lattice spacing which confirms the crystalline nature of the sample. The particle sizes determined from TEM were found to be in agreement with that obtained from X-ray diffraction studies. The electron diffraction pattern of $ZnFe_2O_4$ particles are depicted in figure 3.8.
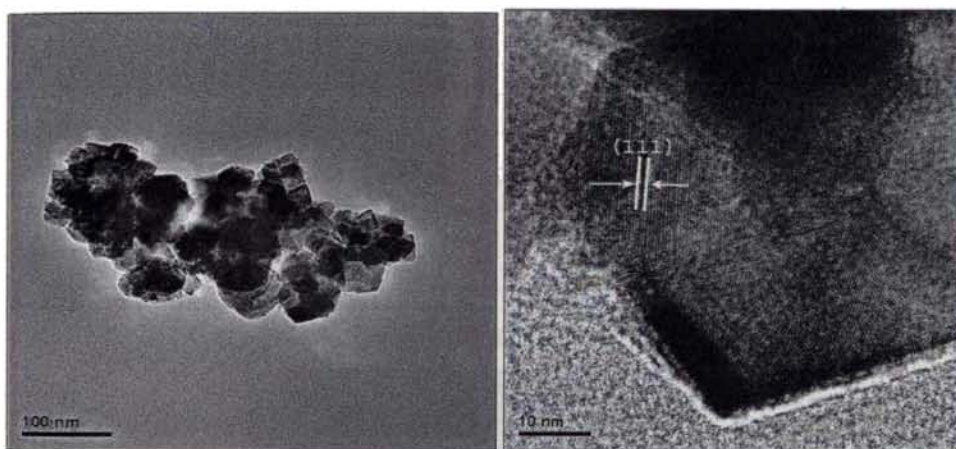
Figure 3.5 TEM and HRTEM images of $MnFe_2O_4$
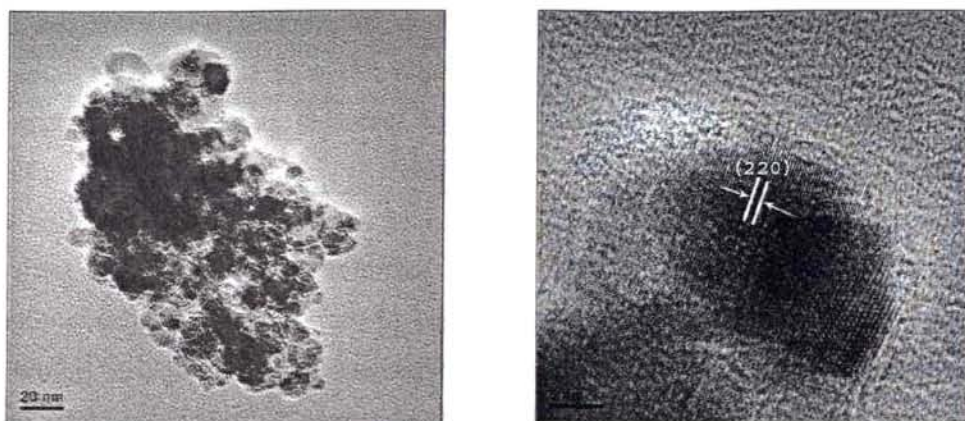
Figure 3.6 TEM and HRTEM images of $Mn_{0.5}Zn_{0.5}Fe_2O_4$
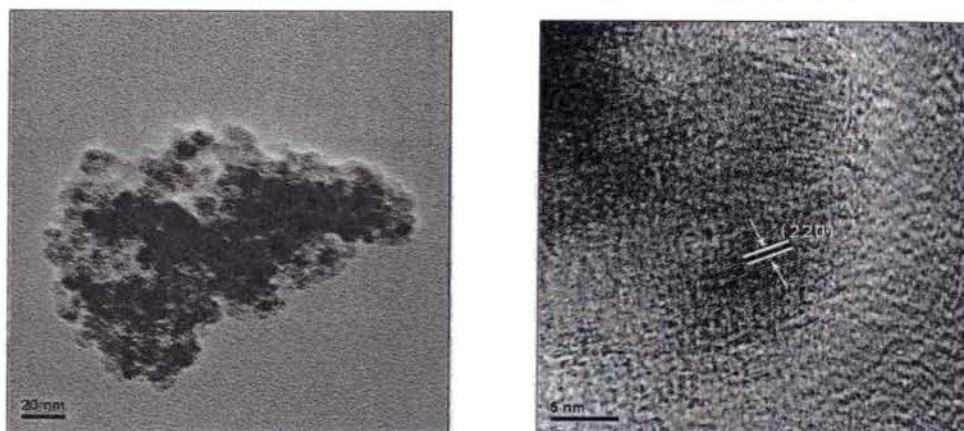
Figure 3.7 TEM and HRTEM images of $ZnFe_2O_4$
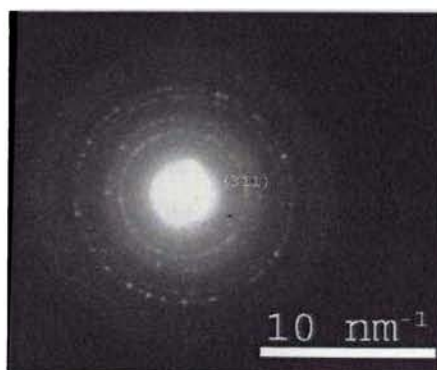
Figure 3.8 Diffraction patterns of the crystallites of
$ZnFe_2O_4$ nanoparticles

Elemental analysis employing EDS and ICP is carried out on these compositions (figure 3.9).The compositions as determined by both EDS and ICP are compared and they are shown in table (3.1).

The ICP analysis of representative samples of $Mn_{1-x}Zn_xFe_2O_4$ was carried out for the samples whose EDS have been measured. The estimated stiochiometry is shown in table (3.1). It can be seen that the stiochiometry is very close to the anticipated values and there is agreement with the results obtained via two different techniques.

(a)

(b)

(c)
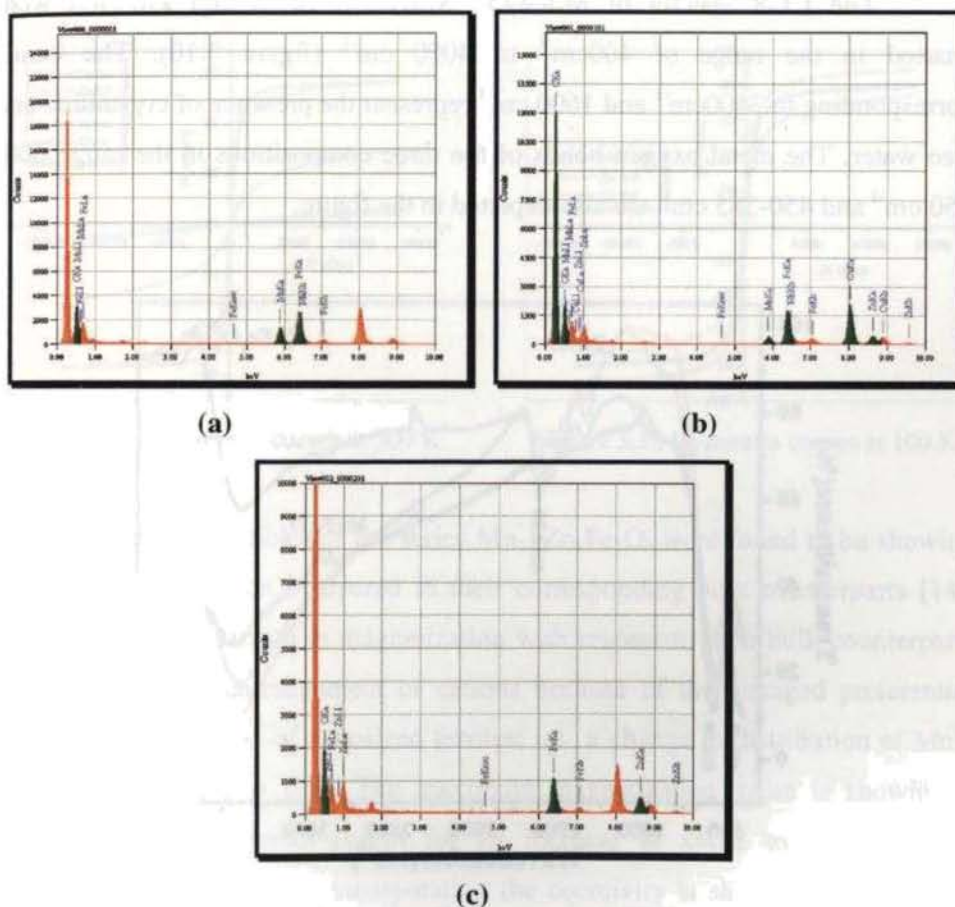
Figure 3.9 EDS of (a) $MnFe_2O_4$, (b) $Mn_{0.4}Zn_{0.6}Fe_2O_4$ and (c) $ZnFe_2O_4$

Sample	Molar Ratio	Expected	EDS	ICP
$MnFe_2O_4$	Mn:Fe	0.5	0.496	0.491
$Mn_{0.4}Zn_{0.6}Fe_2O_4$	Mn:Fe	0.2	0.189	0.191
	Zn:Fe	0.3	0.276	0.281
$ZnFe_2O_4$	Zn:Fe	0.5	0.465	0.468

Table 3.1 Estimated Stiochiometry from EDS and ICP measurements

The FTIR spectra of $MnFe_2O_4$, $Mn_{0.5}Zn_{0.5}Fe_2O_4$ and $ZnFe_2O_4$ were charted in the range of 400cm^{-1} to 4000 cm^{-1} (figure 3.10). The bands corresponding to 3400cm^{-1} and 1600 cm^{-1} represent the presence of crystalline and free water. The metal oxygen bonds of the three compositions in the range 600-550 cm^{-1} and 450-385 cm^{-1} are also depicted in the figure.
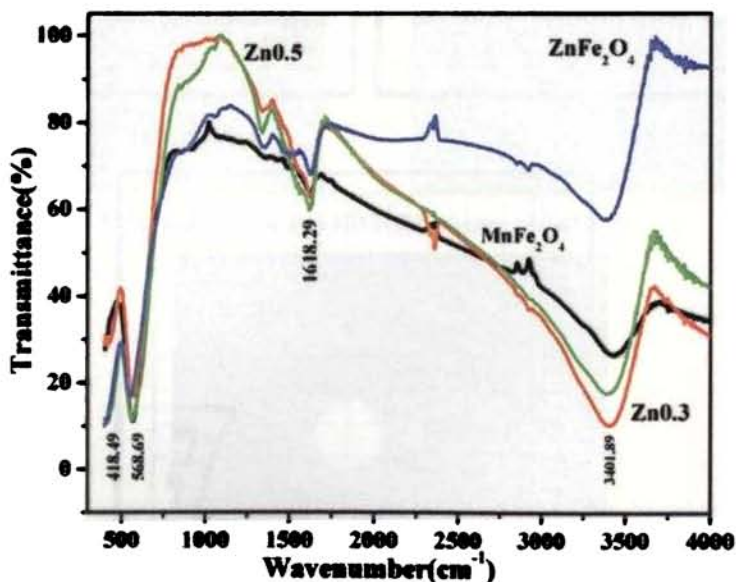
Figure 3.10 FTIR Spectrum of different compositions in the series

However a shift in the peak positions and intensity is observed. This may be due to the difference in the zinc concentration in the different compositions.

Hence the effect of zinc in determining the different structural characteristics of the series is evident in every analysis we have carried out.

3.3 Magnetic Properties

3.3.1 Vibrating Sample Magnetometer Measurements

Hysteresis loop parameters, namely specific magnetisation and coercivity (at 300K and 100K) were evaluated from the representative loops shown in figure 3.11 and figure 3.12. They are tabulated and shown in table 3.2
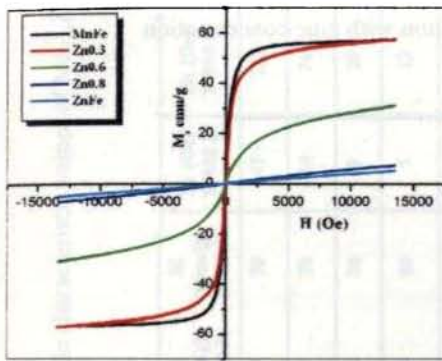
Figure 3.11 Hysteresis curves at 300 K   **Figure 3.12** Hysteresis curves at 100 K
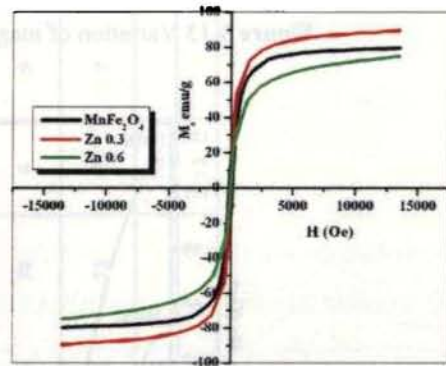
The nanoparticles of the series $Mn_{1-x}Zn_xFe_2O_4$ were found to be showing reduced magnetization compared to their corresponding bulk counterparts [14]. The respective reduction in magnetization with respect to their bulk counterparts can be due to a rearrangement of cations because of the changed preferential occupancy in the case of nanosized ferrites; i.e., a change in distribution of Mn^{2+} and Zn^{2+} on the two sites. The maximum magnetization value is showing a general decreasing trend except for an increase at x=0.2 to x=0.4 (figure 3.13).With increasing zinc incorporation the coercivity is showing a continuous decrease at 300K and 100K (figure 3.14).

85
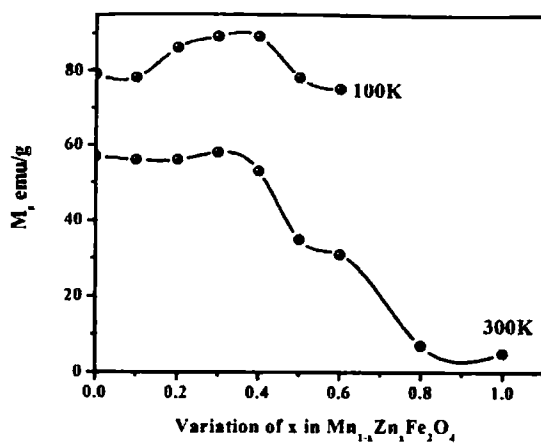
Figure 3.13 Variation of magnetisation with zinc concentration
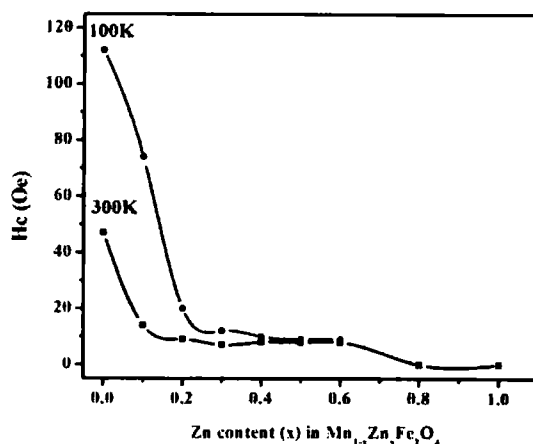
Figure 3.14 Variation of coercivity with zinc concentration

In the case of $Mn_{1-x}Zn_xFe_2O_4$ prepared by standard ceramic techniques, the saturation magnetization value is found to increase with zinc substitution upto x=0.5 and for further increase a decrease is obtained. This variation was qualitatively explained by the assumption that as the zinc content increases, the relative number of ferric ions on the A sites diminishes and this reduces the A-B interaction [15].

Table 3.2 Structural and magnetic characteristic values of $Mn_{1-x}Zn_xFe_2O_4$

$Mn_{1-x}Zn_xFe_2O_4$	Particle Size (nm)	Lattice Parameter (Å)	M (emu/g) T=300 K	M (emu/g) T=100 K	Hc (Oe) T=300 K	Hc (Oe) T=100 K	Tc °C	n_B at 0K μ_B
0	29.1	8.497	57	79	47	112	525	3.67
0.1	18.9	8.487	56	78	14	74	510	3.71
0.2	14.7	8.471	56	86	9	20	490	4.23
0.3	13.1	8.468	58	89	7	12	485	4.39
0.4	12.9	8.454	53	89	8	10	435	4.5
0.5	11.4	8.420	35	78	8	9	275, 480	4.26
0.6	10.3	8.398	31	75	8	9	255, 430	4.01
0.8	8.2	8.354	8.2		7.5			
1	7.2	8.414	7.2		5.2			

The variation of maximum magnetisation values with zinc concentration (at 300K and 100K) in the co-precipitated $Mn_{1-x}Zn_xFe_2O_4$ (figure3.14) was found to deviate from the corresponding variation in bulk [14]. The lower magnitudes of magnetisation is indicative of the presence of Zn^{2+} ions on the octahedral sites. The presence of Mn^{3+} ions together with its preference for octahedral sites can also result in a remarkable change in the cation distribution. The magnetic moments of Mn^{2+} /Fe^{3+} and Mn^{3+} / Fe^{2+} ions are $5\mu_B$ and $4\mu_B$ respectively. Hence the presence of Mn^{3+} / Fe^{2+} pairs in the B lattice reduces the net magnetic moment of the octahedral lattice .This will create a decline in the net magnetization. Also the Jahn-Teller distortion was found to affect the magnetic properties in manganese containing ferrite [15]. The existence of random canting of particle surface spins, surface effects and the occurrence of a glassy state were reported to be playing an active role in the decline of magnetization values [16, 17].

The temperature dependence of magnetization (M vs. T) is depicted in figure 3.15. The Curie temperature (T_c) was estimated by extrapolating the linear section of the temperature dependence of magnetization to the temperature axis. The T_C values of the nanoparticles were found to be larger than that observed for their bulk counterparts. This type of enhancement in T_C was observed in a number of nanoparticles of ferrites [18].

A reduction, rather than an increase in T_c is expected in finite size systems based on theoretical grounds [19]. Hence the increase in T_c can be mainly attributed to the non equilibrium cation redistribution as reported by Kulkarni *et.al.* in ultrafine $MnFe_2O_4$ particles [8]. Higher degree of inversion was found to be associated with higher T_c values in ultra fine ferrite systems. The surface effect should also be considered while discussing the increase in T_c in nanoparticles. For smaller particles, a significant fraction of atoms is on the surface and hence a

different type of interaction can be expected leading to a different average Curie temperature.
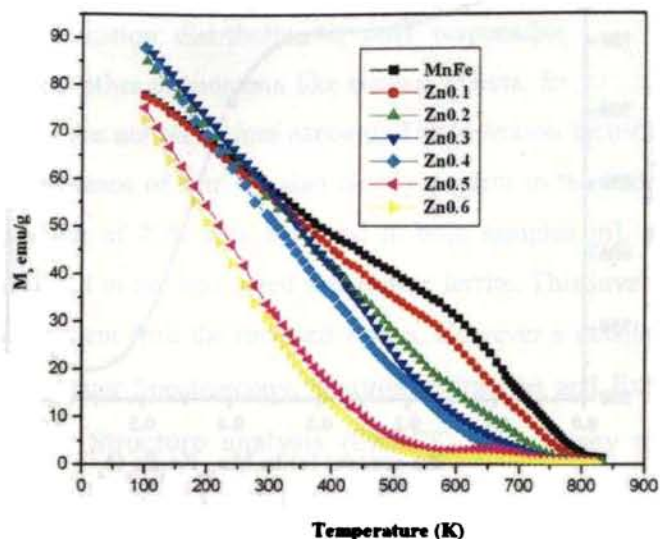
Figure 3.15 M-T curves of $Mn_{1-x}Zn_xFe_2O_4$

The M-T curves of two samples x=0.5 and 0.6 are exhibiting a cusp like behaviour before approaching zero magnetization or T_c. This cusp is absent for all compositions below x=0.5. A similar cusp has been reported by Gajbhhiyee *et al.* [20] in $NiFe_2O_4$ nanoparticles. Wolski *et al.* [21] also attributed the cusp they observed in nanoparticles of $MnFe_2O_4$ to the transformation of one ferrimagnetic phase to another. Rath *et al.* [22] reported similar cusp like behaviour in Mn rich compositions of the MnZn series and explained it as a result of a phase transition occurring at this temperature. The appearance of cusp in the case of $Mn_{0.5}Zn_{0.5}Fe_2O_4$ and $Mn_{0.4}Zn_{0.6}Fe_2O_4$ arises out of a transition from a metastable state to a stable state which is a result of the reorganization of cations between A and B sites.
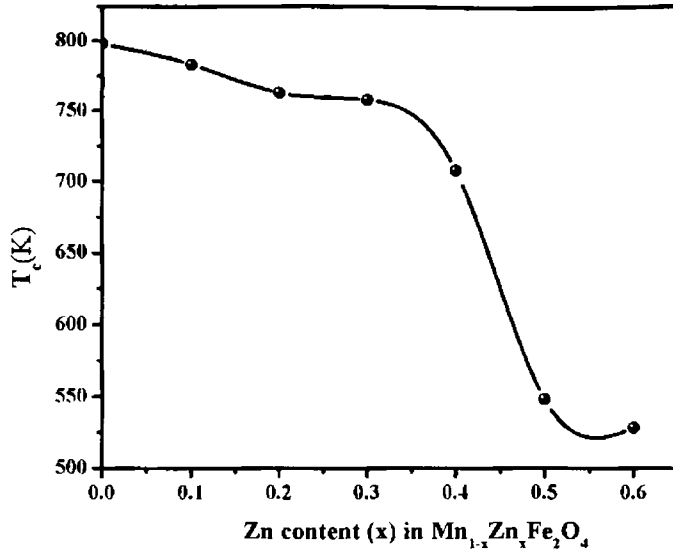
Figure 3.16 Variation of T_c with zinc content

With zinc substitution there is a general decrease in T_c values similar to bulk MnZn series (figure 3.16). This can be mainly attributed to weakened A-B exchange interaction which directly affects the Curie temperature. The anomalous features observed in the compositions for $x \geq 0.5$ is unique and interesting.

The specific magnetization σ_s of the different compositions at 0K are estimated by extrapolating the M-T graph to the Y-axis at 0 K (table 3.2). Magnetic moment in units of Bohr magnetons can be calculated as [23]

$$n_B = \frac{Mol.Wt \times \sigma_s}{5585} \qquad (3.1)$$

where n_B is the magnetic moment (number of Bohr magnetons) and σ_s is the saturation magnetisation per gram at 0K.

The calculated values were found to be lower than their corresponding cousins in the bulk [16] (table 3.2). For manganese ferrite nanoparticles the calculated magnetic moment was 3.67 μ_B (4.6 μ_B for bulk). Based on the calculated μ_B from magetisation values a tentative cation distribution is

90

formulated and is as follows. $Mn_{0.3323}Fe_{0.6677}[Mn_{0.6597}Fe_{1.3403}]$. This is based on Neel's two sublattice [24] model and Chikazumi's approach [6]. Here it is assumed that the cation distribution is only responsible for the decrease in magnetisation and other phenomena like surface effects, formation of dead layer, finite size effects are not taken into account. The inversion factor is calculated to be 66.5%.The presence of Mn^{3+} is also clearly evident in the cation distribution. While an inversion of 20% was observed in bulk samples [6], an inversion of 66.5% was obtained in our nanosized manganese ferrite. This inversion factor was found to be consistent with the reported values. However a detailed investigation employing Mossbauer Spectroscopy, Neutron diffraction and Extended X-Ray Absorption Fine Structure analysis (EXAFS) is necessary to arrive at the cation distribution for the other compositions.

3.3.2 ZFC Measurement of Manganese Zinc Ferrite ($Mn_{0.5}Zn_{0.5} Fe_2O_4$)

Zero field cooled experiments provide a means of investigating the effects of the various magnetic interactions [25]. For the ZFC measurements, the sample was cooled from room temperature to 12K without any external magnetic field and the magnetization was recorded while warming the sample in the applied field. The ZFC magnetization increases continuously as the temperature is increased and then decreases after reaching a maximum value at the blocking temperature, T_B. This is typical of superparamagnetic particles [26]. Below T_B, the spins are successively locked at their sites and do not contribute to the overall magnetization. Above T_B, the magnetization decreases with temperature. The blocking temperature is a function of the experimental measurement time scale, external magnetic field, particle volume, anisotropy constant and particle interactions.

Assuming the particles to be superparamagnetic, monodispersed and non interacting , the anisotropy constant(K) can be calculated from the relation [27]

$$K_{eff}V = kT_B \, ln(\tau_m/\tau_0) \tag{3.2}$$

where V is the volume of the particle, k_B the Boltzmaan's constant T_B the blocking temperature τ_m the measuring time and τ_0 superparamagnetic relaxation time.

The ZFC curve for Zn=0.5 shows typical magnetic behaviour of a superparamagnetic material with a characteristic spin freezing or blocking temperature. The blocking temperature is estimated to be 53K for the manganese zinc ferrite particles of size 11nm. The width of the peak depends upon the distribution in effective anisotropy energy due to shape and size distribution. The sharpness of the peak reflects the highly monodispersed nature of the manganese zinc ferrite nanoparticles (as evident from TEM measurements).
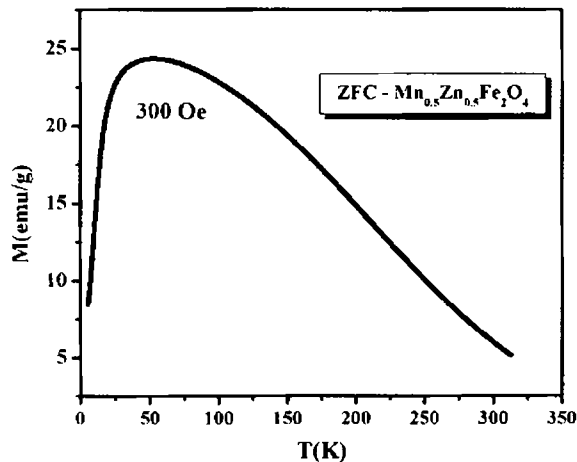
Figure 3.17 ZFC curve for $Mn_{0.5}Zn_{0.5}Fe_2O_4$

Employing the equation 3.2 with the measuring time $\tau_m = 100s$ and $\tau_0 = 10^{-10}s$, diameter=11nm and T_B=53K, at 300Oe the effective anisotropy constant is calculated to be 2.906×10^5 erg/cm^3. The value of K for bulk Manganese zinc ferrite is 7.79×10^4 erg/cm^3 [6]. The actual value of τ_0 depend on whether the particles are interacting with each other or not and this can vary from 10^{-8} to 10^{-13}. Similar deviation in the value of K has been observed in nanoparticles of manganese zinc ferrite [27].

Both structural and magnetic characterization provides sufficient evidence for the existence of a metastable cation distribution at the nanoregime. Enhancement of T_c values together with lower magnetization and coercivity values of the series were found to depend on zinc substitution directly. Consequently by only varying the zinc concentration ratio we can tune the compositions with required structural and magnetic properties for various applications.

3.3 Conclusion

Nanocrystalline manganese zinc ferrite particles for x=0 to x=1 were prepared using wet chemical co-precipitation technique. The particles were found to be exhibiting a spinel structure with sizes varying from 7nm - 29nm. The decrease in particle size and the lattice contraction with increasing zinc concentration in the nanoparticles were due to the occurrence of a metastable cation distribution different from their bulk counterpart. The compositional analysis confirmed the stoichiometry of the sample to be on expected lines. The deviation in the variation of magnetisation with zinc concentration along with the lower magnetization values compared with the bulk is additional evidences for the existence of the metastable cation distribution. Enhanced T_c values obtained are indicative of a non equilibrium cation distribution in the different compositions. The magnetic moment at zero Kelvin was estimated from the temperature dependence of magnetization and a tentative cation distribution for manganese ferrite is proposed. The presence of Mn^{3+}, an inversion of 66.5% and deviation in cation distribution was evident in the proposed cation distribution.

References

1. Raul Valenzuela, *Magnetic Ceramics*, Cambridge University Press, (1994), Great Britain.
2. R H Kodama and A E Berkowiz ,Phy.Rev.B,77 (1996) 394

3. S. D. Shenoy, P. A. Joy, M R Anantharaman, J. Magn. Magn. Mater., 269 (2004),217

4. D J Fatemi,V G Harris,M X Chen,S K Malik, W B Yelon G J Long A Mohan Journal of Applied Physics, 85, (1999), 5172

5. A H Morrish and K Haneeda, J. Appl. Phy., 52,(1981), 2496

6. Soshin Chikazumi, *Physics of ferromagnetism*,(1997)Clarendon Press ,Oxford 200.

7. Sakurai J and Shinjo T, J. Phys. Soc .Jpn, 23 ,(1967) ,1426.

8. C Rath, N C Mishra, S Anand, R P Das, K K Sahu, C Upadhyay and H C Verma , Appl. Phys. Lett ,76, (2000) 475

9. F. K. Lotgering , J. Phys. Chem. Solids, 27,(1996), 139

10. R Arulmurugan, B Jayadevan G Vaidyanathan and S.Sendhilnathan, J .Magn. Magn. Mater. ,288,(2005), 470

11. C Rath ,K K Sahoo,S Anand, S K Date, N C Mishra and R P Das J .Magn. Magn. Mater. 202,(1999), 77

12. K Majima, M Hasegawa, S Katsuyama, H Nagai, S Mishima, J. Mater. Sci. Lett.,12, (1993),185

13. Mellisa. A Denecke, W Gun Ber, G Buxbaum, P Kuske, Mater. Res. Bull., 27, (1992), 507

14. K J Standley , *Oxide Magnetic Materials*,,(1972) ,Clarendon Press Oxford

15. D J Craik, *Magnetic oxides- Part1*, (1975),John Wiley & Sons

16. J M D Coey , Phys Rev. Lett., 27, (1971), 1140

17. M Garcia del Muro, X Batlle and A Labarta , Phys. Rev.: B 59, (1999) ,13584

18. Z X Tang J P Chen C M Sorenson K J Klabunde and G C Hadjipanayis Phys Rev. Lett., 68, (1992), 3114

19. P V Hendriksen S Linderoth and P A Lindgard Phys.Rev. B, 48, (1993), 7259

20. N S Gajbhiye Met. Mater. Processes,10, (1998), 247,

21. W Wolski E Wolska J Kaczmarek and P Piszora Phys. Status Solidi : A., 152, (1995), K19

22. C Rath, N C Mishra, S Anand, S K Date, R P Das, S D Kulkarni and K K Sahu J. Appl. Phys. 91, (2002), 2211

23. J Smit and H P J Wijn, *Ferrites*, (1959) Philips Technical Library, Eindhoven, Netherlands.

24. L Neel ,Ann. de Physics 12,(1948), 137

25. J. C. Denardin, A. L. Brandl, M. Knobel, P. Panissod, A. B. Pakhomov, H. Liu, X. X. Zhang; Phys. Rev. B 65, 064422 (2002).

26. Aparna Roy ,V. Srinivas, S. Ram, J. A. De Toro, J. Appl. Phys. 100 (2006) 094307

27. P. Poddar, J L Wilson, H Srikanth, S A Morrison and E E Carpentar, Nanotechnology, 15, (2004), 5570-5574.

Chapter 4

On the Electrical Properties of Nanostructured Manganese Zinc Mixed Ferrites

Temperature and frequency dependence of dielectric permittivity and dielectric loss of nanosized $Mn_{1-x}Zn_xFe_2O_4$ (for x=0, 0.2, 0.4, 0.6, 0.8, 1) were investigated. Maxwell -Wagner theory together with Koop's phenomenological theory was effectively used to explain the dielectric behaviour of ferrites. The impact of zinc substitution on the dielectric properties of the mixed ferrite is elucidated. Strong dielectric dispersion and broad relaxation were exhibited by $Mn_{1-x}Zn_xFe_2O_4$. The variation of dielectric relaxation time with temperature suggests the involvement of a multiple relaxation processes. Cole-Cole plots were employed as an effective tool for studying the observed phenomena. The activation energies calculated from relaxation peaks and Cole- Cole plots were found to be consistent with each other and indicative of a polaron conduction. The electrical properties, dc conductivity and ac conductivity of nanosized $Mn_{1-x}Zn_xFe_2O_4$ were investigated as a function of frequency, temperature and composition. The activation energy for dc conduction and the mobility of the charge carriers were estimated. The dc conductivity is then explained based on the small polaron conduction process. The frequency dependence of ac conductivity is studied by the power law $\sigma_{ac}(\omega)=B\,\omega^n$ which is typical for charge transport by hopping or tunneling processes. The temperature dependence of n is investigated to understand the conduction mechanism in the different compositions. The conduction mechanisms are mainly based on polaron hopping conduction. The activation energies for ac and dc conduction were calculated.

The electrical properties of materials in the nanoregime are totally different when compared to their bulk counterparts in the micron regime. The modification of dielectric properties when the particle size is reduced is attributed to a variety of reasons namely particle size, shape, boundaries and inclusions. This unique dielectric properties of nanosystems have been effectively used in various dielectric based applications such as capacitors, electronic memories and optical filters [1-3]. In addition, intensive studies on further exploitation of their dielectric properties in futuristic high tech devices are also being pursued. Yet the level of understanding of the dielectric properties of nanosystems is far from being satisfactory both from a qualitative and quantitative outlook.

Ferrite materials enjoy special significance in the field of electronic and telecommunication industry because of their novel dielectric and electrical properties which makes them useful in radiofrequency circuits, high quality filters, rod antennas, transformer cores, read/write heads for high speed digital tapes and other devices [4-6]. The electrical and dielectric properties of ferrites provide information necessary for the selection of these materials for specific applications. The properties of ferrites are sensitive to their composition and microstructure, which in turn are sensitive to their processing conditions. Nanoparticles of spinel ferrites by virtue of their unique electronic and physical structure display enhanced properties which may be harnessed for technological applications.

In ferrites, the dielectric properties are explained assuming that a heterogeneous structure consisting of grains and grain boundaries exist [7-9]. Dielectric relaxation was reported in micron sized particles in the frequency regime of 1-100 kHz. Dielectric dispersion and dielectric relaxation was found to change with grain size. In the case of nanometer sized particles the existence of a large number of interface dipoles can give rise to different relaxation processes

resulting in a broader relaxation. Sharp dispersion and relaxation effect with multiple relaxation times are reported in ferrites in the nanoregime [10]. Dielectric properties are expected to be modified substantially because of the presence of nanosized grains and grain boundaries.

The dielectric permittivity of a material is found to depend on the frequency of measurement. It decreases from static permittivity (ε_s) at low frequencies to a smaller limiting value of (ε_α) at higher frequencies. This has been explained by Debye [11] and the difference in the values of ε_s and ε_α has been attributed to dipolar polarization and generally a single relaxation time is associated with the dielectric relaxation. In real dielectrics, different types of dipole species are present and these may give rise to several relaxation times instead of a single one. Hence R H Cole and K S Cole [12] modified Debye's equations to incorporate the effects of multiple relaxation times. These Cole-Cole plots based on these modified equations can be effectively used for studying the dielectric relaxation at the molecular level and for evaluation of the dispersion parameters [chapter2].

The frequency dependent ac conductivity and temperature dependent dc conductivity are the deciding factors for technological applications of ferrites. It is thought that electrical conduction in ferrites results from the thermal activation of electrons or positive holes along chains of neighbouring cations in the ionic lattice. The activation energy for transport mechanism is greatly reduced if the crystal lattice intrinsically contains cations of one element in more than one valence state. In the case of manganese zinc ferrites, electron hopping between $Fe^{3+} \leftrightarrow Fe^{2+}$ ions and hole hopping between $Mn^{2+} \leftrightarrow Mn^{3+}$ ions are found to be responsible for electrical conduction [13]. Thus conductivity is found to depend on the availability of Fe^{2+}/Fe^{3+} ions and M^{2+}/M^{3+} pairs in octahedral sites In micron sized particles prepared by solid state reactions, sintering gives rise to the

of Fe^{2+} and Mn^{3+} ions. However in the nanoregime where no high temperature sintering is involved, presence of Fe^{2+}/Fe^{3+} and Mn^{3+}/Mn^{2+} will be dependent on the preparative conditions. A cation redistribution which is different from that of their bulk cousins is observed in nanoparticles of ferrites [14]. These factors are bound to play a major role in deciding the overall electrical properties of the nanosized manganese zinc ferrite. Nanoparticles of the series belonging to $Mn_{1-x}Zn_xFe_2O_4$ (where x=0.0, 0.2, 0.4...1) were found to be exhibiting different structural and magnetic properties with respect to their bulk counterparts [chapter 3]. A reduction in lattice parameter, accompanied by reduced magnetization values, enhanced Curie temperature and a metastable cation distribution are all hall marks of nanosized manganese zinc ferrites.

It is in this situation that a detailed investigation on the electrical properties of a series belonging to $Mn_{1-x}Zn_xFe_2O_4$ assumes significance. The employment of Cole-Cole plot to evaluate various parameters namely, ε_s (static dielectric constant), ε_o (optical dielectric constant), α (spreading factor), τ_0 (average relaxation time) and τ (molecular relaxation time) will definitely lead to an understanding of the phenomenon of dispersion occurring in the nanosized mixed ferrites. In this investigation manganese zinc ferrites belonging to the series $Mn_{1-x}Zn_xFe_2O_4$ (for x=0, 0.2, 0.4, 0.6, 0.8 and 1) are synthesized by employing low temperature methods. In order to gain an insight into the phenomenon of dielectric dispersion and absorption, the dielectric properties of these ferrites in the frequency regime of 100 kHz - 8MHz are evaluated and the results are correlated. One can obtain information about the mechanism of conduction and evaluate the activation energy from the analysis of ac and dc conductivities. All these can lead to a good explanation and understanding of the electrical behaviour in ferrites.

4.1 Experimental

Manganese zinc ferrites belonging to the series $Mn_{0.6}Zn_{0.4}Fe_2O_4$ were prepared by using low temperature co-precipitation technique [chapter 3]. The powder samples were pressed in to pellets having a diameter of 12mm and 2mm thickness. These pellets were then heat treated at $200^{O}C$ before being subjected to different studies. Uniformity in heat treatment and pressure applied was ensured for all the samples in the series. The porosity of these samples (all compositions) was determined after evaluating their X-ray densities using the structural parameters derived from XRD measurements. The samples were found to be having a porosity of around 30% and we observed consistency in the values for all the compositions.

The dc conductivity of the sample was measured using a Keithley 236 Source meter and dielectric measurements were carried out on samples in the series using a home made dielectric cell and an HP 4285 LCR meter in the frequency range of 100 kHz - 8MHz over a temperature of 303 K-393 K. The data acquisition was automated by interfacing the LCR meter with a virtual instrumentation package called LabVIEW (National Instruments). Copper discs of same diameter as the pellets were used as contact electrodes and the measurements were carried out under rotary vacuum. Lead and fringe capacitance were eliminated before every run of the sample. Cole-Cole plots for different temperatures were drawn by the circle least square method utilizing the real and imaginary values of dielectric permittivity [15]. Dispersion parameters were evaluated from the Cole –Cole plots [chapter 2].

4.2 Scanning Electron Microscopy Analysis

Scanning electron micrographs of the samples are depicted in figure 4.1(a-d). It can be seen that the grains are uniformly sized and are in the

nanoregime. The micrographs show the presence of a large number of interfaces which have a direct bearing on the dielectric properties of these ferrites.

(a)

(b)

(c)

(d)
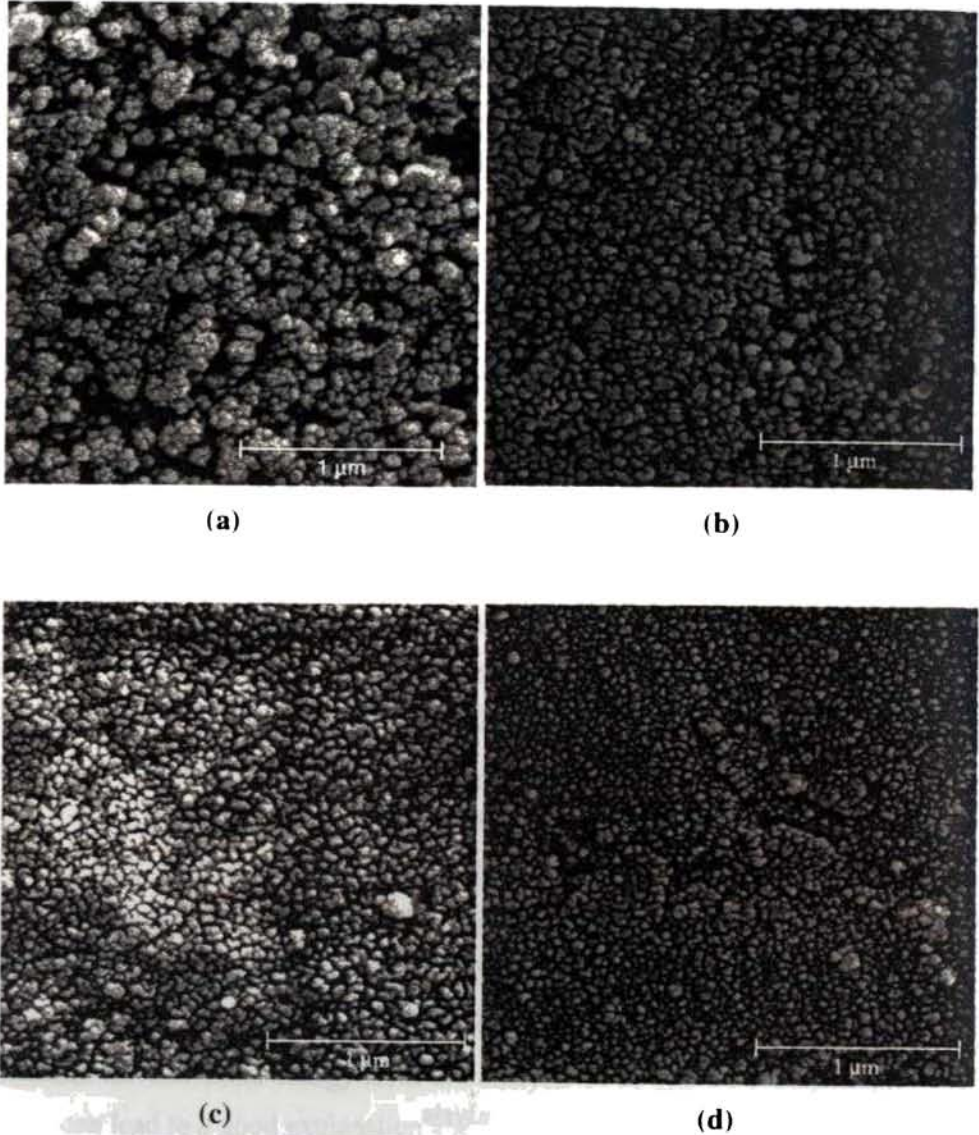
Figure 4.1 SEM images of (a) $MnFe_2O_4$ (b) $Mn_{0.8}Zn_{0.2}Fe_2O_4$ (c) $Mn_{0.2}Zn_{0.8}Fe_2O_4$ and (d) $ZnFe_2O_4$

4.3 Dielectric Properties

4.3.1 Dielectric Dispersion

The variation of dielectric properties with frequency is depicted in figure 4.2 (a-f). It can be seen that the relative dielectric permittivity, ε' exhibits an inverse dependence with frequency as reported in a number of ferrite compounds. It decreases with increase in frequency and remains a constant at higher frequencies. In our frequency regime of measurements (100 kHz -8 MHz), it is the polarization due to interface dipoles which contribute to the overall dielectric properties of the sample [16, 17]. Earlier, theories like Maxwell Wagner theory of dielectric dispersion were employed to study the dispersion [7, 8]. It was assumed that the dielectric polarization had its origin in the heterogeneous structure of ferrites with grains and grain boundaries [18]. The effect of grain interfaces are more pronounced at lower frequencies where we observe relatively large values of ε'. The space charge polarization occurring at the interfaces at lower frequencies can also contribute to the dielectric permittivity at lower frequencies.

Many researchers have reported a similarity between conduction process and dielectric polarization in ferrites [10]. Normally, for Manganese zinc ferrites, the conduction process is explained on the basis of electron hopping between Fe^{2+} and Fe^{3+} and hole hopping between Mn^{2+} and Mn^{3+} on the octahedral sites. In the Rezlescue Model, the hopping of electrons/holes results in the local displacements of the electrons/ holes which collectively contribute to the total polarization [19]. Denecke et $.al$ observed the presence of Mn^{3+} ions in octahedral sites in co-precipitated manganese zinc ferrite nanoparticles prepared using highly basic solution [20]. The electrons exchanging between Fe^{2+} and Fe^{3+} ions and the holes that transfer between Mn^{3+} and Mn^{2+} ions are responsible for electric conduction and dielectric polarization in manganese zinc ferrites. At higher frequencies, the frequency of electron / hole exchange will not be able to follow
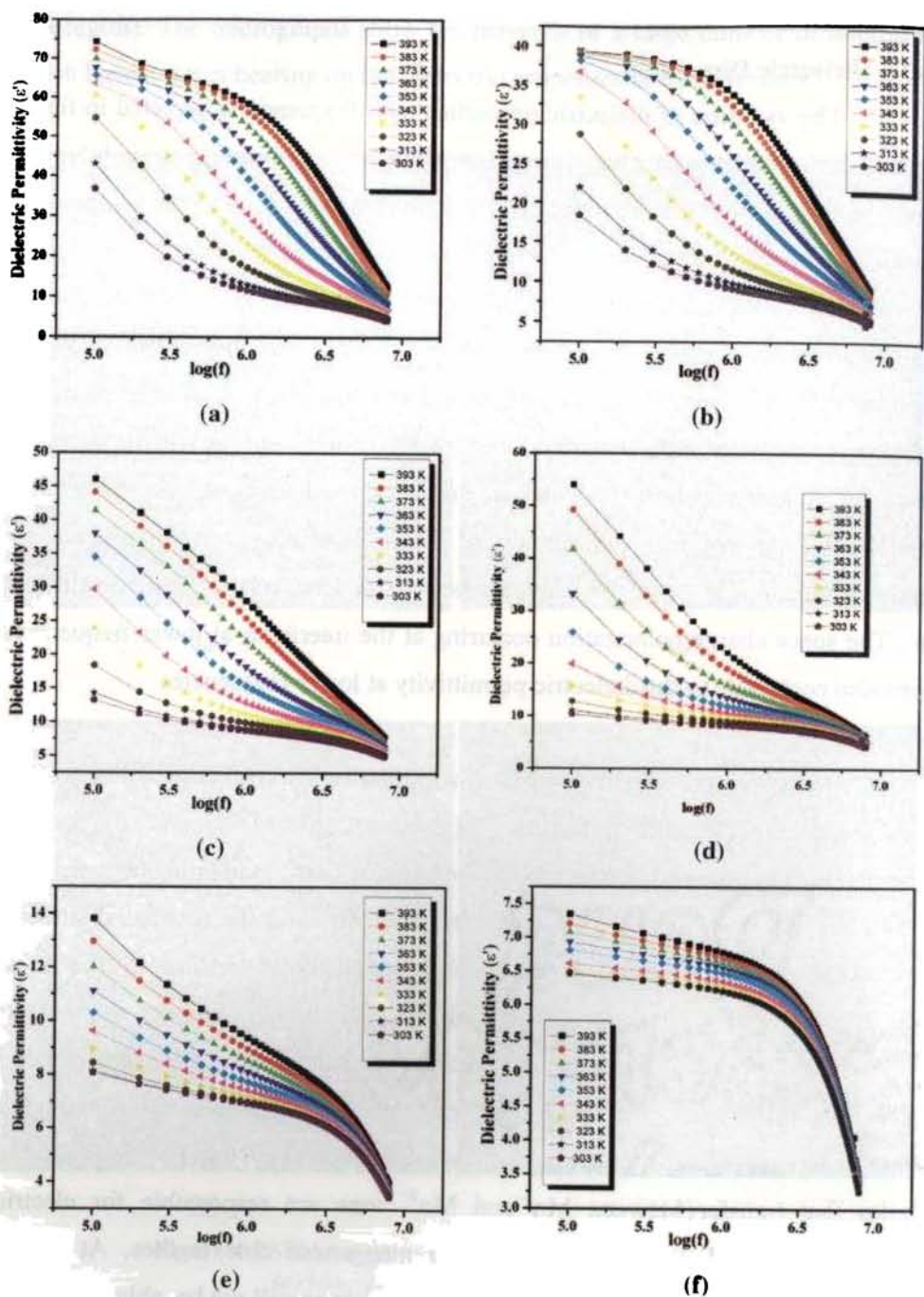
Figure 4.2 Dielectric Permittivity vs. Frequency plot of (a) $MnFe_2O_4$
(b) $Mn_{0.8}Zn_{0.2}Fe_2O_4$ (c) $Mn_{0.6}Zn_{0.4}Fe_2O_4$ (d) $Mn_{0.4}Zn_{0.6}Fe_2O_4$
(e) $Mn_{0.2}Zn_{0.8}Fe_2O_4$ and (f) $ZnFe_2O_4$
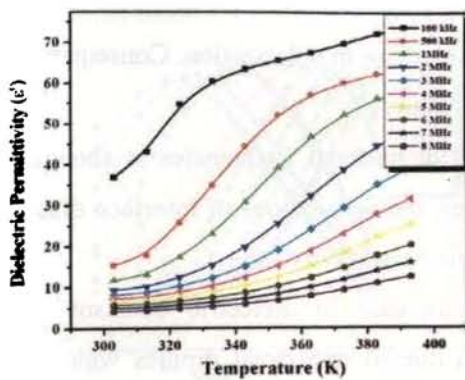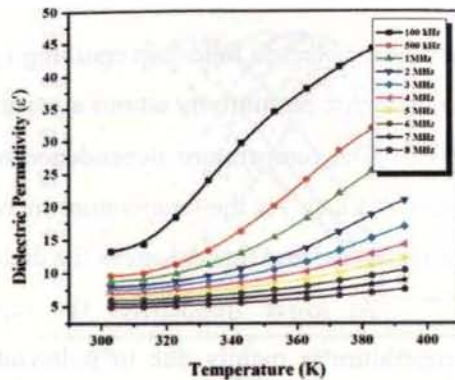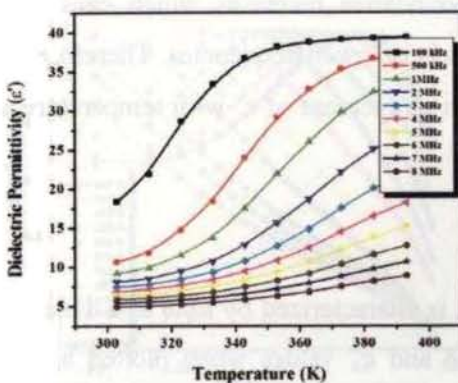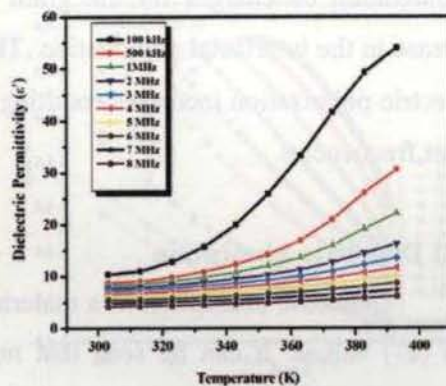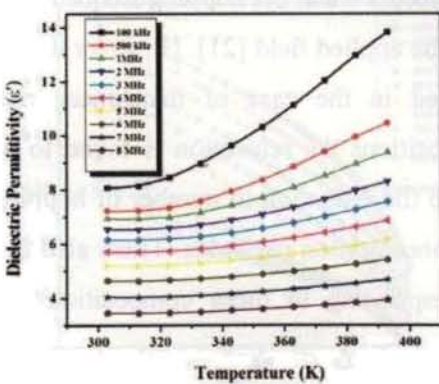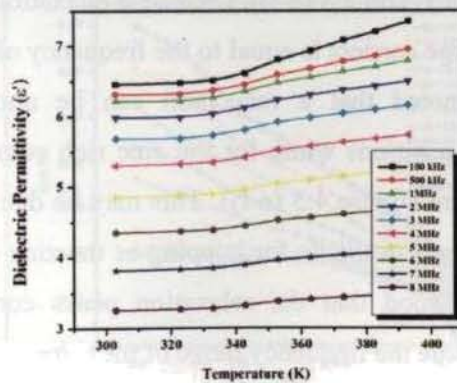
Figure 4.3 Dielectric Permittivity vs. temperature plot of (a) $MnFe_2O_4$
(b) $Mn_{0.8}Zn_{0.2}Fe_2O_4$ (c) $Mn_{0.6}Zn_{0.4}Fe_2O_4$ (d) $Mn_{0.4}Zn_{0.6}Fe_2O_4$
(e) $Mn_{0.2}Zn_{0.8}Fe_2O_4$ and (f) $ZnFe_2O_4$

the applied electric field thus resulting in a decrease in polarization. Consequently the dielectric permittivity attains a constant value.

The temperature dependence of ε' at selected frequencies is shown in figure 4.3(a-f). As the temperature increases, the orientations of interface dipoles are facilitated and this enhances the dielectric permittivity.

At lower frequencies the rapid increase in dielectric constant with temperature is mainly due to polarization due to interfacial dipoles which are strongly dependent on temperature [17]. As temperature increases, the accumulation of charges on the grain boundaries increases which causes an increase in the interfacial polarization .This is at lower frequencies. Therefore the dielectric polarization increases resulting in an increase of ε' with temperature at lower frequencies.

4.3.2 Dielectric Absorption

Dielectric absorption in a material is characterized by $tan\delta$ and dielectric loss (ε") values. It can be seen that $tan\delta$ and ε" values when plotted against frequency exhibit relaxations at specific frequencies and temperatures (figure 4.4(a-f) and 4.5 (a-f)). Dielectric relaxation occurs when the hopping frequency of charge carriers is equal to the frequency of the applied field [21]. However it is to be noted that a relaxation can be noticed in the case of manganese rich compositions while for the zinc rich compositions the relaxation is found to be absent (figure 4.5 (e-f)). This may be due to the reduction in number of hopping charges available for hopping as the zinc concentration increases. There also is a likelihood that the relaxation peaks corresponding to these compositions lie outside the frequency range of measurement.
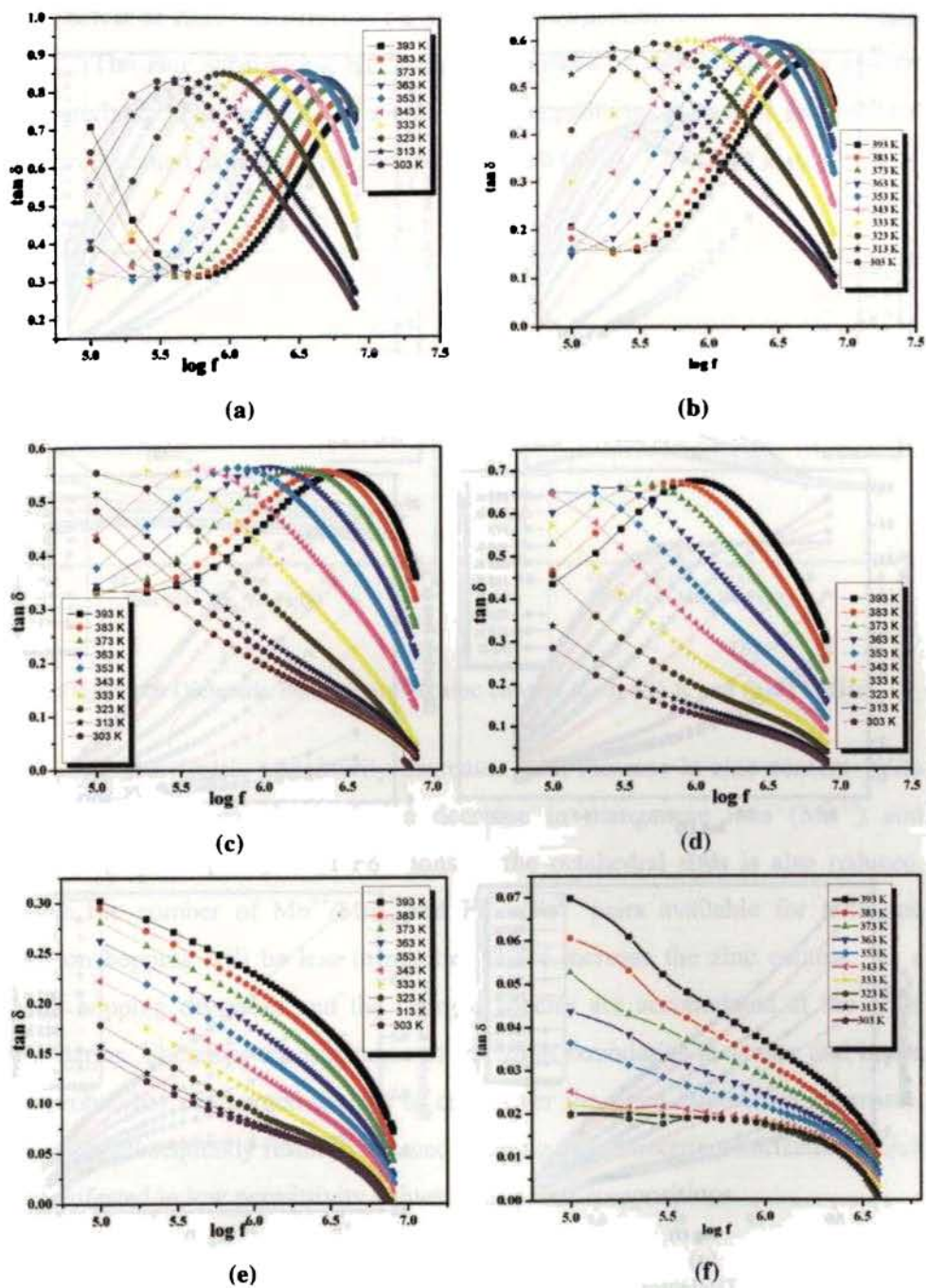
Figure 4. 4 Tan δ vs. Temperature plot of (a) $MnFe_2O_4$ (b) $Mn_{0.8}Zn_{0.2}Fe_2O_4$ (c) $Mn_{0.6}Zn_{0.4}Fe_2O_4$ (d) $Mn_{0.4}Zn_{0.6}Fe_2O_4$ (e) $Mn_{0.2}Zn_{0.8}Fe_2O_4$ and (f) $ZnFe_2O_4$
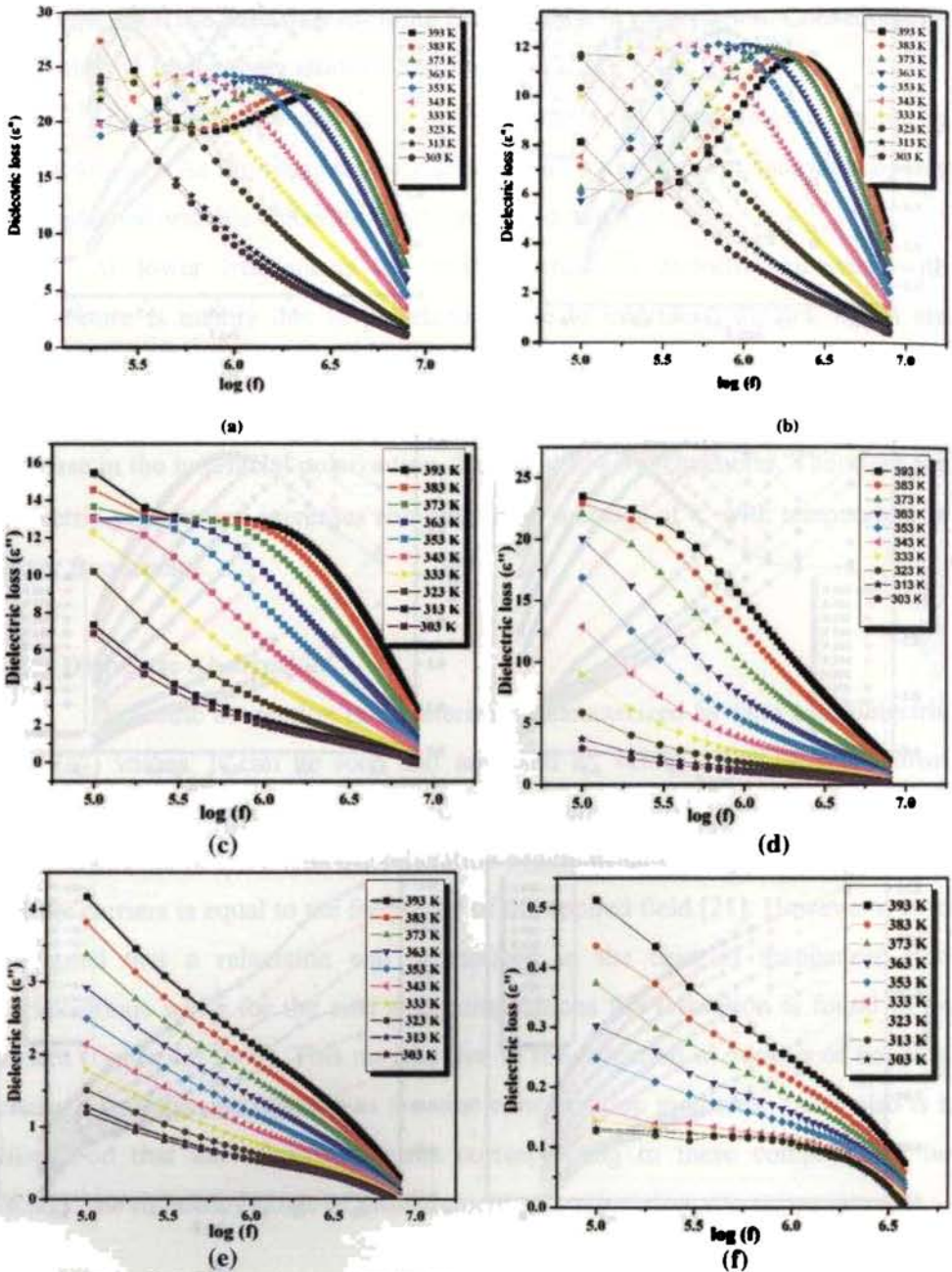
Figure 4. 5 Dielectric loss vs. Log(f) plot of (a) $MnFe_2O_4$ (b) $Mn_{0.8}Zn_{0.2}Fe_2O_4$
(c) $Mn_{0.6}Zn_{0.4}Fe_2O_4$ (d) $Mn_{0.4}Zn_{0.6}Fe_2O_4$ (e) $Mn_{0.2}Zn_{0.8}Fe_2O_4$ and (f) $ZnFe_2O_4$

4.3.3 Effect of Zinc Substitution on dielectric properties

The zinc substitution has a direct influence in modifying the dielectric characteristics. The variation of ε with zinc compositions is studied for different temperatures and different frequencies (figure 4.6 (a-b)).

(a)   **(b)**
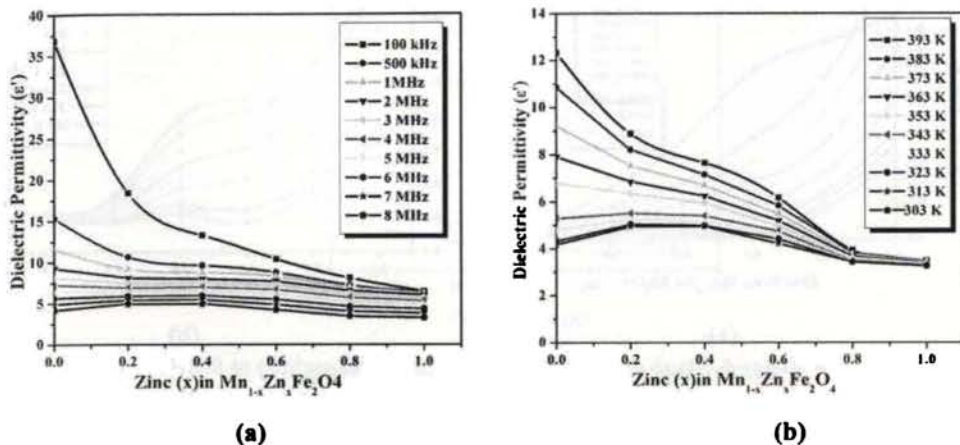
Figure 4.6 Dielectric Permittivity vs. zinc content (a) at 303 K and (b) at 8MHz

The dielectric permittivity decreases with increase in zinc content. With increasing zinc content there is a decrease in manganese ions (Mn^{3+}) and consequently the presence of Fe^{2+} ions in the octahedral sites is also reduced. Hence the number of Mn^{3+}/Mn^{2+} and Fe^{3+}/Fe^{2+} pairs available for hole and electron hopping will be less in number as we increase the zinc content. As a result hopping decreases and the charged species are accumulated at the grain boundaries. Therefore the resistance of the grain boundaries increases and hence the probability of charged species to cross over the grain boundaries decreases. This will subsequently result in reduced hopping and dielectric polarization which is manifested in low permittivity values in zinc rich compositions.

Figure 4.7 (a-b) depicts the effect of zinc substitution on the *tan δ* of the $Mn_{1-x}Zn_xFe_2O_4$ series. A reduction in dielectric absorption values is seen with an

increase in zinc concentration. A decrease in the Fe^{2+}/Fe^{3+} and Mn^{2+}/Mn^{3+} pairs available for conduction with increase in zinc concentration can be thought of as one of the reasons for this type of behaviour in manganese zinc ferrites

(a) **(b)**
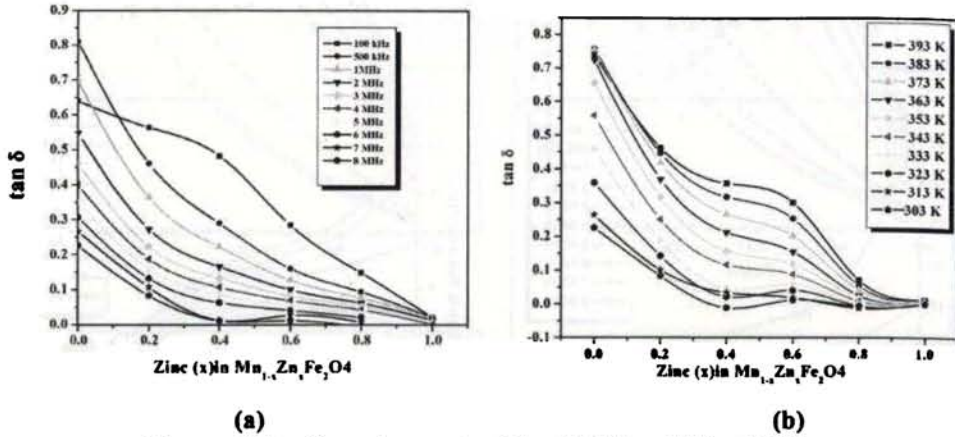
Figure: 4.7 tanδ vs. zinc content (a) at 303 K and (b) at 8MHz

We have suggested that the dielectric polarization can be explained based on the hopping of charge carriers. A relaxation occurs when the hopping frequency equals the applied frequency. The evaluation of the activation energy can provide more insight on the transport properties of ferrites [22].

4.3.4 Activation Energy from relaxation peaks

The condition for observing a maximum in the dielectric loss of a dielectric material is given by the relation [21],

$$\omega\tau'=1$$

where τ' is the relaxation time and

$$\omega = 2\pi f_{max}$$

(4.1)

The value of f_{max} can easily be observed from figure 4.4(a-f). The relaxation time τ can be determined from equation (4.1). Then τ can be written as,

$$\tau' = \tau_0 \, exp\left(\frac{E_d}{k_B T}\right)$$

(4.2)

where τ_0 is the pre exponential constant which equals the relaxation time at infinitely high temperatures, k_B is the Boltzmann's constant, T is the temperature in degree absolute and E_d the activation energy for dielectric relaxation.
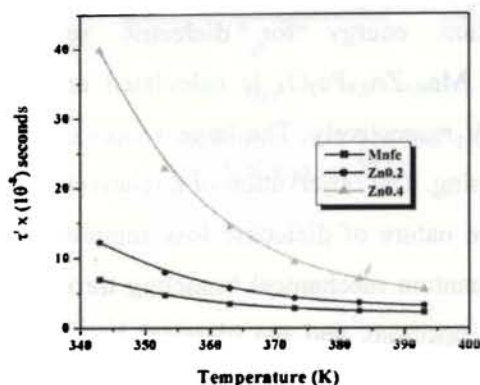
Figure 4.8 Relaxation time (τ) vs temperature

The variation of τ' with temperature is shown in figure (4.8) which showed a decrease in relaxation time with temperature. This point towards the possibility of existence of multiple relaxation mechanisms with a distribution of relaxation times in the nanosystems.

From the slope of the graph between $ln\tau'$ vs. $1000/T$, E_d the activation energy for dielectric relaxation can be determined (figure 4.9).
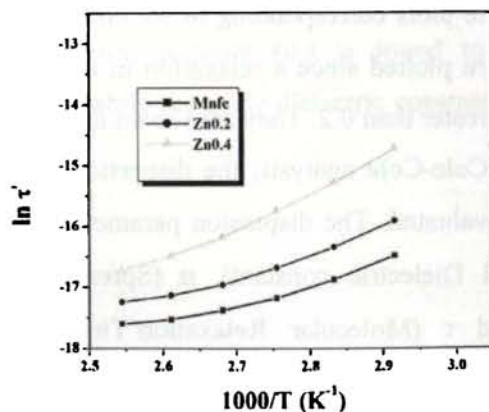
Figure 4.9 $ln\tau'$ vs. $1000/T$ (K^{-1})

The hopping depends on the activation energy which is associated with the electrical energy barrier experienced by the electrons during hopping. Since $\tau = 1/2P$ where P is the hopping probability, the decrease in relaxation time with temperature results in an increase in hopping probability with temperature.

The activation energy for dielectric relaxation for $MnFe_2O_4$, $Mn_{0.8}Zn_{0.2}Fe_2O_4$ and $Mn_{0.6}Zn_{0.6}Fe_2O_4$ is calculated and found to be 0.329eV, 0.412eV and 0.497eV respectively. The large values of activation energy points towards polaron hopping. The observation of a relatively large value of activation energy and relaxation nature of dielectric loss suggests two distinct conduction processes namely Quantum mechanical tunneling through the barrier separating the two equilibrium positions and the classical hopping of a carrier over the barrier or some combination or a variant of the two[23-24].

The presence of a strong dielectric dispersion and broad relaxation peaks in the dielectric loss spectra are indicative of multiple relaxations. Therefore Cole-Cole plots were employed as an effective tool for studying the observed phenomena [26]. Knowledge of dispersion parameters can help reveal the dynamics of the relaxation phenomena in these materials.

4.3.5 Cole-Cole Analysis

The Cole-Cole plots corresponding to the compositions of $MnFe_2O_4$ and $Mn_{0.8}Zn_{0.2}Fe_2O_4$ were plotted since a relaxation in ε" was found absent for all composition with x greater than 0.2. They are shown in figure 4.10(a-c) and figure 4.11(a-c). From the Cole-Cole analysis, the dispersion parameters of these two compositions were evaluated. The dispersion parameters like ε_s (static dielectric constant), ε_α (Optical Dielectric constant), α (Spreading factor), τ_0 (Average Relaxation Time) and τ (Molecular Relaxation Time) of the two samples are evaluated and they are tabulated and their variation with temperature is analyzed.

112
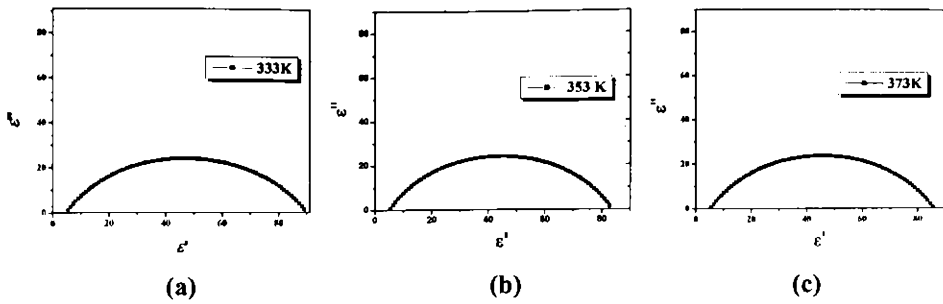
Figure 4.10 Cole-Cole plots (ε' vs. ε") of $MnFe_2O_4$ (a) 333K, (b) 353K and (c) 373K
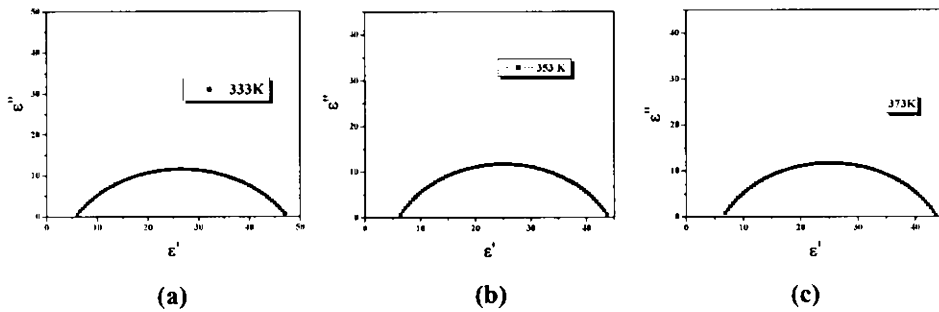
Figure 4.11 Cole-Cole plots (ε' vs. ε") of $Mn_{0.8}Zn_{0.2}Fe_2O_4$ (a) 333K, (b) 353K and (c) 373K

The optical dielectric constant (ε_α) is found to be increasing with temperature (figure 4.12), while the static dielectric constant is found to decrease (figure 4.13).
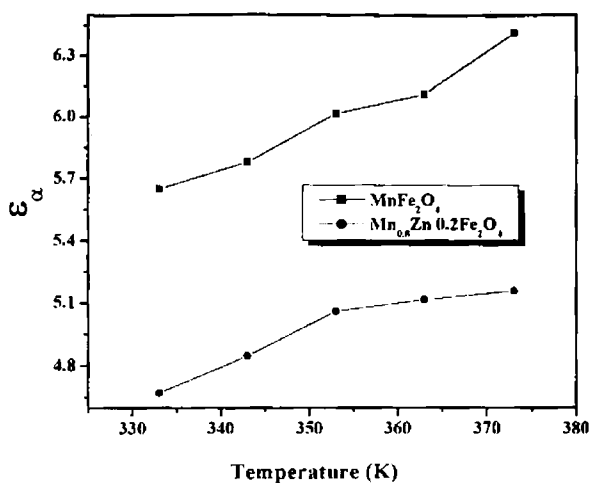
Figure 4.12 Variation of ε_α with temperature

However the variation of the two limiting values of dielectric permittivity within the measured temperature range was not very large. The spreading factor is a measure of the broadening of the relaxation time (figure 4.14).
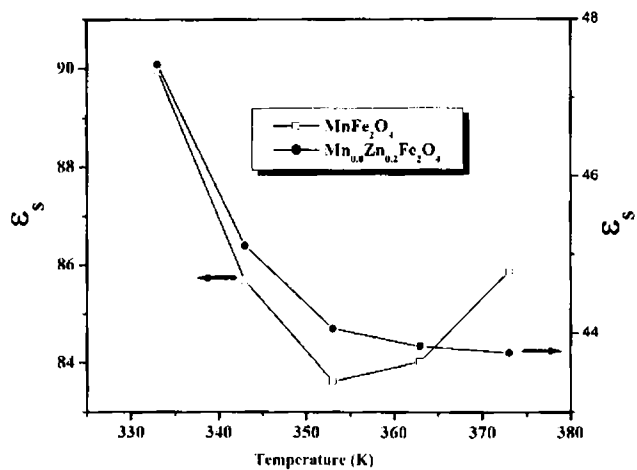
Figure 4.13 Variation of ε_s with temperature

The average relaxation time is the effective time constant for the relaxation involved while molecular or intrinsic relaxation time is the time constant for the immediate molecular dipole relaxation.
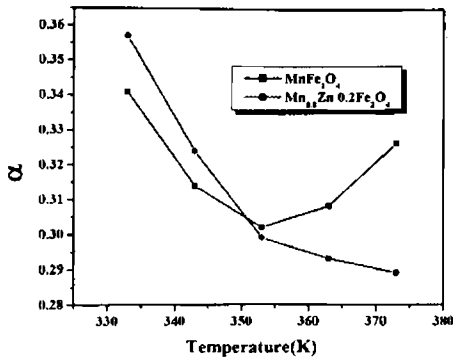
Figure 4.14 Variation of α with temperature
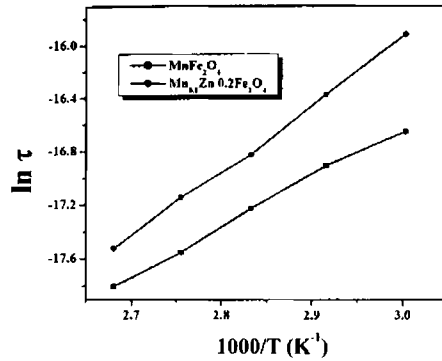
Figure 4.15 ln τ vs 1000/T (from Cole-Cole plot)

Both average relaxation time and molecular relaxation time decreases with increasing temperature (table 4.1). The rise in temperature causes a reduction in the mean time of stay of dipoles resulting in a decrease of relaxation time with temperature. Hence, as relaxation time decreases with temperature there is a decrease in spreading factor. Activation energy for dielectric relaxation can be calculated from the slope of *ln τ vs. 1000/T* plot (figure 4.15). The activation energy calculated for the $MnFe_2O_4$ and $Mn_{0.8}Zn_{0.2}Fe_2O_4$ are 0.315 eV and 0.426 eV respectively. These values were found to be in very good agreement with those calculated from relaxation peaks (0.329eV for $MnFe_2O_4$ and 0.412eV for $Mn_{0.8}Zn_{0.2}Fe_2O_4$) The activation energy is found to be increasing with zinc substitution.

T(K)	ε_s		ε_α		α		ε''		τ_0 10^8 sec		τ 10^8 sec	
	MnFe	ZnO.2	MnFe	ZnO.2	MnFe	ZnO.2	MnFe	ZnO.2	MnFe	ZnO.2	MnFe	ZnO.2
373	85.85	43.75	6.41	5.16	0.326	0.289	24.28	11.66	3.43	2.70	1.86	2.45
363	84.02	43.83	6.11	5.12	0.308	0.293	24.10	11.69	5.04	3.47	2.39	3.59
353	83.62	44.05	6.02	5.06	0.302	0.299	23.99	11.67	6.95	4.82	3.31	4.95
343	85.67	45.12	5.78	4.85	0.314	0.324	23.84	11.56	10.96	6.63	4.55	7.77
333	89.97	47.43	5.65	4.67	0.341	0.357	23.61	11.54	17.41	8.60	5.88	12.23

Table 4.1 Dispersion Parameters from Cole-Cole Analysis

ε_s – Static dielectric constant
ε_α – Optical Dielectric constant
α – Spreading Factor
ε'' – Dielectric Loss
τ_0 – Average Relaxation Time
τ – Molecular Relaxation Time

4.4 AC Conductivity Studies

The variation of ac conductivity with frequency and temperature is given in figure 4.16 (a-f). It is observed that initially the ac conductivity increases with frequency, reaches a maximum and then decreases. As the frequency of the applied field increases, hopping of charge carriers also increases thereby increasing the conductivity. But at higher frequencies, the hopping of charge carriers could not follow the applied field frequency and it lags behind the applied frequency resulting in a decrease in the ac conductivity values.

The increase of ac conductivity with frequency and temperature could also be explained on the basis of Koops model which assumes that ferrite samples act as a multilayer capacitor [7-8]. According to this model, at low frequencies, the conductivity is due to the grain boundaries, while the dispersion at higher frequencies is due to the conducting grains.

AC conductivity decreases with zinc concentration as in the case of dc conduction indicating decrease in the availability of charge carriers with increasing zinc content (figure 4.17). With increasing zinc content, there is a decrease in manganese ions (Mn^{3+}) and consequently the presence of Fe^{2+} ions in the octahedral sites is also reduced. Hence the number of Mn^{3+}-Mn^{2+} and Fe^{2+} - Fe^{3+} pairs available for hole and electron hopping will be less in number as the zinc content is increased. As a result, hopping decreases and charged species accumulate on the grain boundaries. Therefore the resistance of the grain boundary increases and hence the probability of charged species crossing over the grain boundaries decreases. This eventually reduces conductivity with increasing zinc substitution. So there is relatively large number of hopping pairs in manganese ferrite compared with the other compositions.
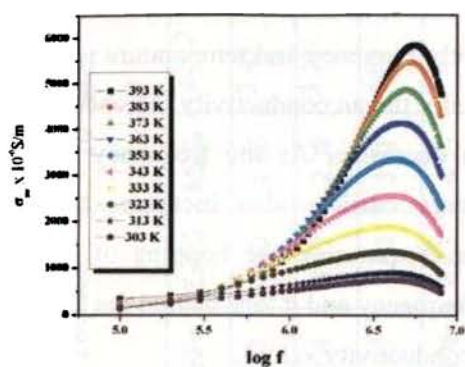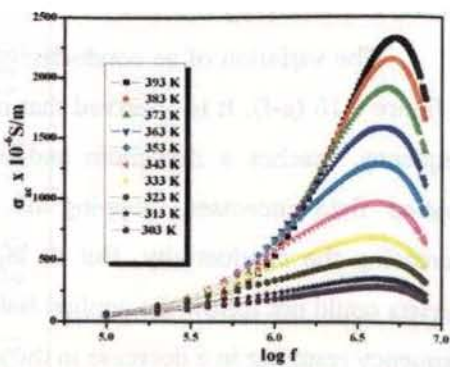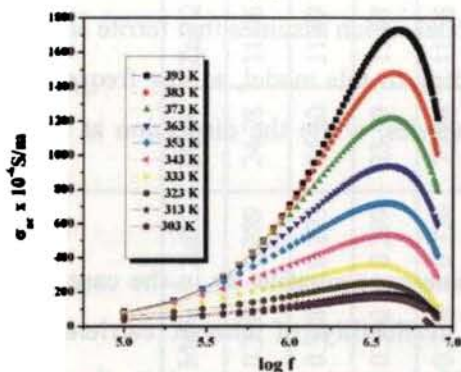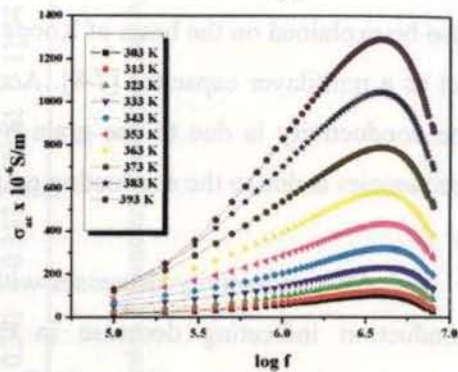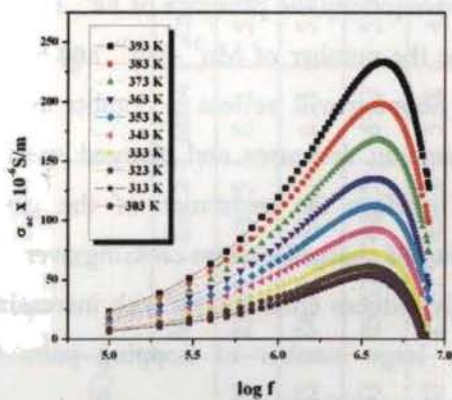
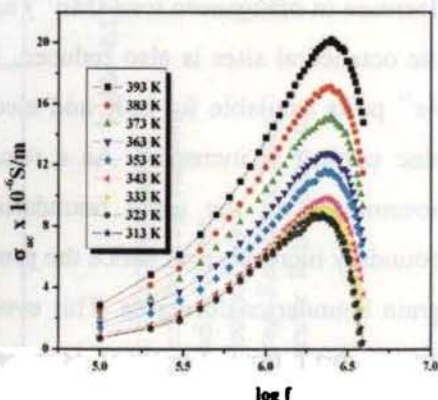**Figure 4.16** Variation of ac conductivity with frequency and temperature of
(a) $MnFe_2O_4$ (b) $Mn_{0.8}Zn_{0.2}Fe_2O_4$ (c) $Mn_{0.6}Zn_{0.4}Fe_2O_4$ (d) $Mn_{0.4}Zn_{0.6}Fe_2O_4$
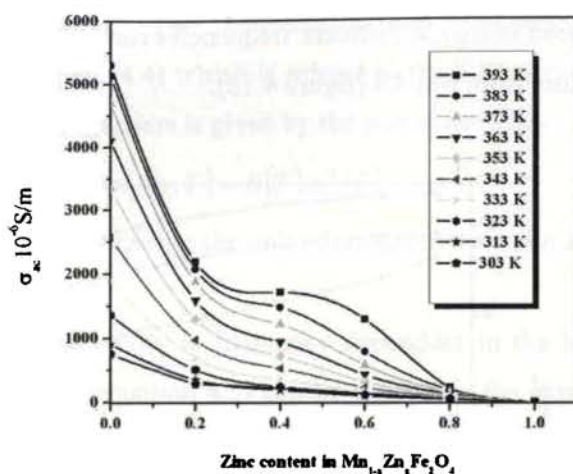(e) $Mn_{0.2}Zn_{0.8}Fe_2O_4$ (f) $ZnFe_2O_4$

Figure 4.17 Variation of σ_{ac} with zinc content in $Mn_{1-x}Zn_xFe_2O_4$ at 4MHz

In the case of zinc ferrite the presence of hopping pairs may be entirely due to the presence of zinc ions in the octahedral sites which give rise to electron hopping Fe^{2+}-Fe^{3+} pairs. It is interesting to see that (figure 4.16 (a-f)) in manganese rich compositions, the increase in ac conductivity with frequency and temperature in the kHz region is diminutive while in the case of zinc rich samples there is marked increase in conductivity with temperature and frequency in this regime. Hence different conduction mechanism can be expected in these compositions.

The real part of ac electrical conductivity consists of two terms [25]

$$\sigma = \sigma_1(T) + \sigma_2(\omega,T) \qquad (4.3)$$

The first term is the temperature dependent dc conductivity which is related to the drift of electric charge carriers and follows an Arrhenius relation given by

$$\sigma_1(T) = \sigma_0 \exp\left(-\frac{E_a}{k_B T}\right) \qquad (4.4)$$

119

where E_a is the activation energy for electric conduction. σ_0 the pre-exponential factor .The activation energy at different frequencies can be found out by plotting ln σ_{ac} vs temperature from eqn 4.4 (figure 4.18).
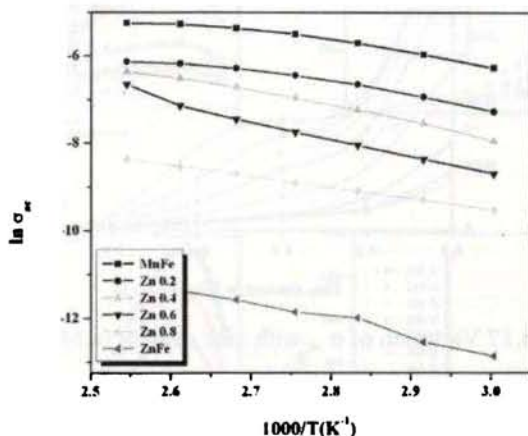

Figure 4.18 $ln\sigma_{ac}$ vs $1000/T$ $Mn_{1-x}Zn_xFe_2O_4$ at 4MHz

From the slope of the linear region of the graph, E_a for electrical conduction at 4MHz is determined. The variation of activation energy with zinc content indicates an increasing trend with increasing zinc content (figure 4.8). Since both hole hopping between Mn^{3+}- Mn^{2+} and Fe^{2+}-Fe^{3+} electron hopping can happen in these ferrites, the activation energy calculated can be taken as an average of the activation energies for the two hopping processes and should be less than 0.21eV [20]. The higher activation energies are associated with polaron conduction. In ferrites, the cations are surrounded by close packed oxygen anions and hence can be treated as isolated from each other. There will be little direct overlap of the charge clouds or orbitals. Hence a localized electron model is appropriate in the case of electrons. When the charge carriers are localized, charge transport take place via phonon assisted hopping between localized sites. Localization of the charge carriers may give rise to the formation of polarons and the charge transport may be considered between the nearest neighbour sites [10].

Hence polaron conduction can be expected in these ferrites as indicated by dielectric measurements. The temperature and frequency dependent ac conductivity in equation (4.4) which is related to the dielectric relaxation caused by the localized charge carriers is given by the power law [26].

$$\sigma_2(\omega, T) = B(T)\omega^n(T) \tag{4.5}$$

where B is the parameter having the unit of conductivity and n is a dimensionless parameter.

Since ac conductivity is frequency dependent in the lower temperature region, the power law (equation 4.5) can be applied to the experimental data by plotting the graph $\log\sigma_{ac}$ vs. $\log\omega$ for different compositions. This is done for the frequency region where σ_{ac} is exhibiting an increase with frequency. The value of n is estimated from the slope of the $\log\sigma_{ac}$ vs. $\log\omega$ graphs. The dependence of n with temperature is plotted and is shown in figure 4.19(a-f).
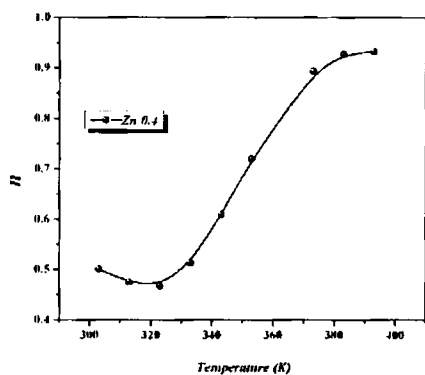
It is known that variation of n with temperature can throw light on the conduction mechanism [27, 28]. If n increases with temperature, small polaron tunneling is the predominant mechanism [29]. A minimum value of n followed by an increase suggests that the predominant conduction is by overlapping large polaron tunneling mechanism [30]. Under such circumstances n is temperature independent and quantum mechanical tunneling is the possibility [31]. The correlated barrier hopping [32] is usually associated with decrease of n with temperature. It can be seen that the behaviour of n is different in the manganese rich and zinc rich compositions. This observation indicated a different conduction mechanism in these compositions. In manganese rich compositions of the series $Mn_{1-x}Zn_xFe_2O_4$ for $x \leq 0.5$ the value of 'n' is found to be increasing with temperature (figure 4.19 (a-c)). This is characteristic of small polaron tunneling and can be explained based on small polaron tunneling model for ac conduction [29].
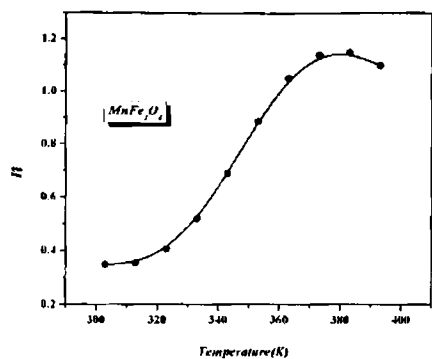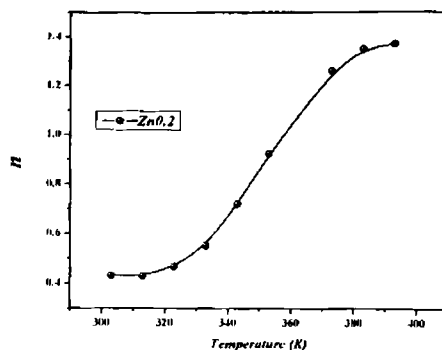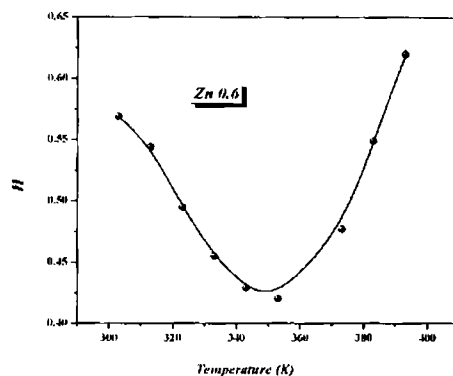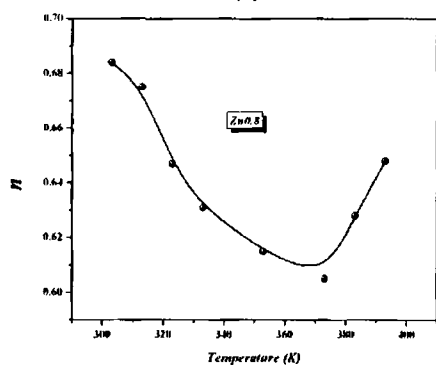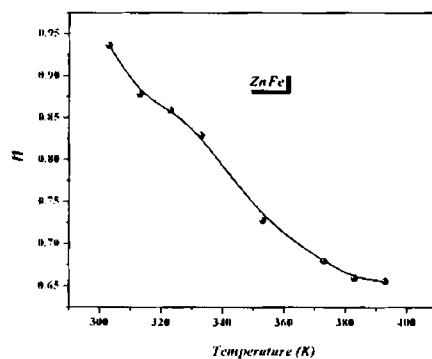
Figure 4.19 Variation of 'n' with temperature for (a) $MnFe_2O_4$ (b) $Mn_{0.8}Zn_{0.2}Fe_2O_4$ (c) $Mn_{0.6}Zn_{0.4}Fe_2O_4$ (d) $Mn_{0.4}Zn_{0.6}Fe_2O_4$ (e) $Mn_{0.2}Zn_{0.8}Fe_2O_4$ and (f) $ZnFe_2O_4$

The frequency exponent n based on this model is evaluated as,

$$n = 1 - \frac{4}{ln\left(\dfrac{1}{\omega \tau_0}\right) - \dfrac{W_H}{k_B T}} \tag{4.6}$$

where k_B is the Boltzmann's constant, T the temperature. W_H is the barrier height for infinite site separation, τ_0 the relaxation time and ω the angular frequency. According to this model, the ac conductivity is given by

$$\sigma(\omega) = \frac{\pi^4}{24} \frac{e^2 \, k_B T \, [N(E_F)]^2 \, \omega R_\omega^4}{\alpha} \tag{4.7}$$

where e is the electronic charge, k_B is the Boltzmann's constant, T the temperature and α is the spatial extent of polaron, N (E_f) the density of states at the Fermi level and R_w is the tunneling distance.

However in the case of zinc rich compositions of $Mn_{1-x}Zn_xFe_2O_4$ upto Zn=0.8 the variation of 'n' is found to be different (figure 4.19(d)-4.19(e)). The value of 'n' decreases with temperature, reaches a minimum and then increases .This behaviour is in accordance with the variation of 'n' in overlapping large polaron tunneling model (OLPT) of ac conduction [33].

The frequency exponent 'n' is given by the equation

$$n = 1 - \frac{8 \alpha R_\omega + 6 \beta W_{HO} \, r_p / R_\omega}{\left(2 \alpha R_\omega + \beta W_{HO} \, r_p / R_\omega \right)^2} \tag{4.8}$$

where β is $1/k_B T$, k_B is the Boltzmann's constant, T is the temperature in degree absolute, r_p is the polaron radius separation and W_{HO} is the barrier height for infinite site separation, α the spatial extent of the polaron, $N(E_f)$ the density of states at the Fermi level and R_w is the tunneling distance.

The ac conductivity for OLPT model is given by [30]

$$\sigma(\omega) = \frac{\pi^4 e^2 (k_B T)^2 [N(E_F)]^2 \omega R_\omega^4}{12 \left(2\alpha k_B T + \dfrac{W_{HO} \, r_p}{R_\omega^2} \right)} \tag{4.9}$$

The maximum resistivity is observed in the case of zinc ferrite where a decrease of 'n' with temperature is found (figure 4.19f). This variation of n with temperature is similar to that predicted by correlated barrier hopping conduction model using the equation, [32]

$$n = 1 - \frac{6k_B T}{W_M + k_B T \ln(\omega \tau_0)} \tag{4.10}$$

The correlated barrier hopping model predicts ac conductivity as

$$\sigma(\omega) = \frac{\pi^3}{24} [N(E_F)]^2 \varepsilon \varepsilon_0 \omega R_\omega^6 \tag{4.11}$$

Where $N(E_F)$ the density of states at the Fermi level , ε the dielectric permittivity of the medium ε_0 is the free space permittivity a nd R_ω the hopping distance.

It has been found that apparently the mechanism of ac conduction in nanostructured manganese zinc ferrites is found to be different for different compositions. The formation of small non overlapping polarons in the manganese rich compositions may be directly related to the availability of more hopping charge pairs in these ferrites. When there is a reduced number of hopping charges, the spatial extent of the polaron may extend to several inter atomic distances resulting in the formation of overlapping large polarons. Hence Overlapping Large Polaron Tunneling conduction is observed in the zinc rich compositions. Since pristine zinc ferrite is free of Mn^{2+}-Mn^{3+} pairs, it is to be expected that in $ZnFe_2O_4$, the conductivity is predominating because of Fe^{3+}- Fe^{2+} electron hopping in the lattice. But the formation of these hopping ion pairs depends on the occupancy of Zn^{2+} ions in the octahedral sites preferentially. So the observed conduction mechanism in zinc ferrite is correlated Barrier hopping conduction based on hopping of charge carriers between two sites over a barrier separating

them. A clear understanding of the conduction mechanism in nanostructu.
ferrites remain elusive unless and until the conductivity measurements are carried
out for a wide range of frequencies and over a wide temperature range.

4.5 DC Conductivity Studies

The dc conductivity values varied between 10^{-5} S/m to 10^{-9} S/m for
pristine manganese ferrite to pristine zinc ferrite. The variation of conductivity
with temperature indicates the semiconducting nature of the ferrites (figure 4.20).
But a localized electron model is more appropriate in the case of ferrites rather
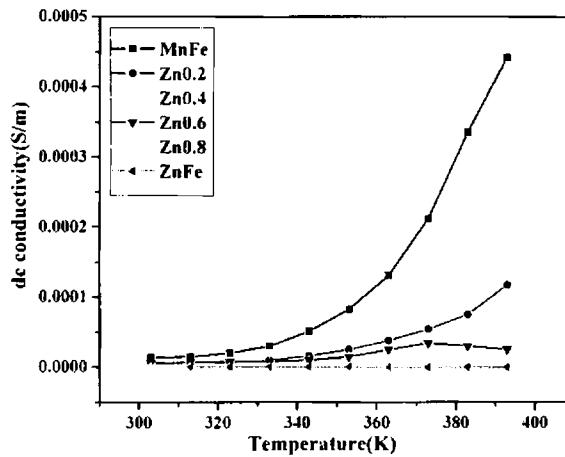than the collective electron band model (for semiconductors).

Figure 4.20 Variation σ_{dc} with temperature

Based on hopping model, electron hopping between $Fe^{2+} \leftrightarrow Fe^{3+}$ ions and
hole hopping between $Mn^{3-} \leftrightarrow {}^{\bullet}Mn^{2+}$ ions collectively contribute to the
conductivity in these ferrites. Hence the conductivity depends largely on the
availability of charge carriers and their mobility. The dc conductivity decreases
with increasing zinc content as in the case of ac conductivity and pure zinc ferrite
is found to possess very high resistivity values. The decrease in conductivity can
hence explained on the basis of decrease in hopping pairs. The activation energy

for dc conduction is evaluated from Arrhenius relationship and is given in Table 4.2. The activation energy for dc and ac conduction is found to be different. This may be due to the frequency and temperature dependence of ac conduction. But both the values exhibit a decrease with zinc content indicating an increase in resistivity.

Since the conductivity in ferrites directly depends on the mobility of charge carriers, the evaluation of the mobility values can throw light on the nature of charge carriers involved in conduction. The mobility μ of the charge carriers was calculated from the experimental values of the electrical conductivity (σ) and charge carrier concentration (n_c) using the expression [34] .

$$\mu = \frac{\sigma}{n_c e} \tag{4.12}$$

where e is electrical charge of the carrier.

The charge carrier concentration can be determined using the relation

$$n_c = \frac{N_a X_s P_{Fe}}{M} \tag{4.13}$$

where N_a is the Avogadro number, X_s the sintered density and P_{Fe} is the number of Fe atoms in one mol of the ferrite and M the molecular weight.

The mobility obtained for different samples and its variation with temperature is shown in figure (4.21). It can be noticed that the mobility increases with temperature and decreases with zinc concentration. The mobility is found to lie in the range 10^{-10} to 10^{-12} cm^2/V.sec. This mobility is found to be lower than that for electrons (10^{-4} cm^2/V.sec) and holes (10^{-8} cm^2/V.sec) [39]. These mobility values are found to be the same as that of the mobility of small polarons. So it is reasonable to assume that small polarons are involved in the conduction process in these ferrites.
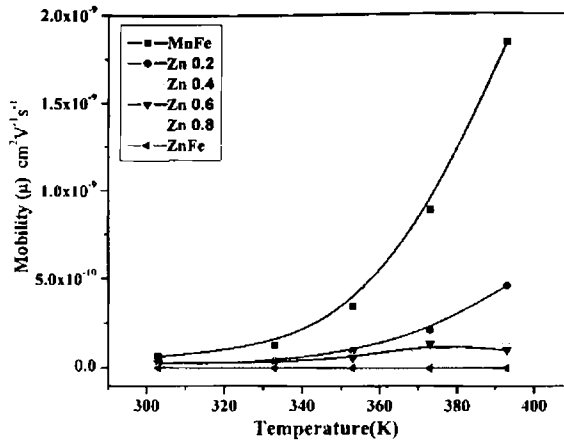
126

Figure 4.21 Variation of mobility with temperature

A small polaron is created when an electron gets trapped at a given site as a consequence of the displacement of adjacent atoms or ions. The entire defect then migrates by an activated hopping mechanism. Low value of mobility, temperature independent Seebeck co-efficient and thermally activated hopping are important characteristics of small polaron conduction.

The polaron radius (r_p) [35] for all the compositions was calculated by employing the relation

$$r_P = \frac{1}{2}\left[\frac{\pi}{6N}\right]^{\frac{1}{3}} \qquad (4.14)$$

where N is the number of interstitial sites per unit volume $(96/a^3)$. In spinel ferrites 64 octahedral (A) sites and 32 tetrahedral (B) sites are available per unit volume.

The calculated values of r_p for different zinc concentrations are found to be ~ 0.5 Å. Since the polaron radius is lower than the hopping distance (inter ionic distance between octahedral sites - 2.93Å). Small polaron hopping is a possibility in these compositions.

The expression for conductivity in small polaron conduction [36] is given by the equation

$$\sigma = \frac{A}{T}\exp(-E_A / k_B T) \qquad (4.15)$$

where T is temperature in degree absolute and E_A is the activation energy for conduction and A is a constant. The value of A is given by

$$A = \frac{\upsilon_{ph} N e^2 R^2 c(1-c)\exp(2\alpha R)}{k_B} \qquad (4.16)$$

where N is the number of ion sites per unit volume, R average intersite spacing, c is the fraction of sites occupied by polaron, α is the electron wave function decay constant, υ_{ph} is optical phonon frequency and k_B is the Boltzmann's constant.

Further, in order to check whether the conduction process obeys Small Polaron Hopping, a graph is plotted with log σT on the Y-axis and 1/T on the X-axis (figure 4.22).

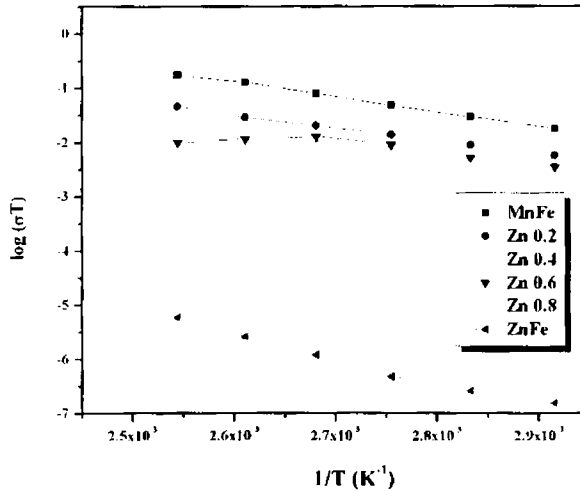**Figure 4.22** log σT vs 1/T

We obtained straight line graphs for different compositions which points to the possibility of small polaron assisted transport in these mixed ferrites [37]. The inferences arrived based on the above discussions are tabulated and are shown in table 4.2.

| Composition $Mn_{1-x}Zn_xFe_2O_4$ | Activation energy for | | AC Conduction Mechanism |
	DC Conduction (eV)	AC Conduction (eV)	
$MnFe_2O_4$	0.372	0.303	Small Polaron Tunnelling
$Mn_{0.8}Zn_{0.2}Fe_2O_4$	0.344	0.292	Small Polaron Tunnelling
$Mn_{0.6}Zn_{0.4}Fe_2O_{41}$	0.388	0.31	Small Polaron Tunnelling
$Mn_{0.4}Zn_{0.6}Fe_2O_4$	0.468	0.348	Overlapping Large Polaron Tunnelling
$Mn_{0.2}Zn_{0.8}Fe_2O_4$	0.473	0.358	Overlapping Large Polaron Tunnelling
$ZnFe_2O_4$	0.833	0.495	Correlated Barrier Hopping

Table 4.2 Activation energy and ac conduction mechanism in $Mn_{1-x}Zn_xFe_2O_4$

4.6 Conclusion

The frequency and temperature dependence of the dielectric parameters of $Mn_{1-x}Zn_xFe_2O_4$ nanoparticles were studied. The low frequency dielectric dispersion was explained in terms of Maxwell-Wagner theory of interfacial polarization .The effect of grains and grain interfaces were found to be enhanced in the nanoregime. The mechanism of dielectric polarization was found to be similar to that of conduction process involving the hopping /tunneling of charge carriers. The decrease in ε and $\varepsilon"$ with zinc substitution point to the decrease in availability of Mn^{2+}-Mn^{3+} and Fe^{2+}-Fe^{3+} pairs with increasing zinc. The $\tan\delta$ and $\varepsilon"$ exhibit strong relaxation peaks and relaxation time τ was estimated from these relaxations. The activation energy for dielectric relaxation determined from τ values suggested a conduction involving polaron hopping or tunneling. The presence of dielectric relaxation implies the existence of multiple relaxation

processes occurring in the system. Signatures corresponding to the existence of multiple relaxation times were evident from the Cole- Cole plot. Cole –Cole plots provide dispersion parameters and their temperature dependence was also studied. The transport behaviour of nanosized $Mn_{1-x}Zn_xFe_2O_4$ is evaluated by measuring the dc conductivity and ac conductivity. Both ac and dc conductivity are found to decrease with increasing zinc content. This was confirmed by the increase in activation energy with zinc substitution. The higher values of activation energy indicated a conduction mechanism involving hopping of polarons. The evaluation of drift mobility and polaron radius confirmed small polaron conduction as the conduction mechanism responsible for dc conductivity. The frequency dependent term of ac conductivity was analysed and the frequency parameter 'n' for the different compositions are evaluated. Based on the variation of n with temperature, appropriate conduction mechanisms are proposed for the different compositions. However scope exists for elaborate theoretical studies on this type of polaron conduction mechanisms in ferrites.

References

1. T. Thurn-Albrecht, J. Schotter, G. A. Ka¨stle, N. EmLey, T. Shibauchi,L. Krusin-Elbaum, K. Guarini, C. T. Black, M. T. Tuominen, and T. P.Russell, Science, 290, (2000), 2126.

2. D. A. Allwood, G. Xiong, M. D. Cooke, C. C. Faulkner, D. Atkinson,N. Vernier, and R. P. Cowburn, Science, 296, (2002), 2003.

3. J. I. Martı́n, J. Nogue´s, K. Liu, J. L. Vicent, and I. K. Schuller, J. Magn.Magn. Mater. 256, (2003), 449.

4. M Sugimoto, Journal of American Ceramic Society 82, (1999), 269.

5. B Gillot Eur.Phys., J: Appl.Phys. 91, (2002), 10.

6. Shigeyuki Somiya, Fritz Aldinger,Nils Claussen,Richard M Spriggs,Kenji Uchino, Kunihito Koumoto, Masayuki Kaneno 2003 *Handbook of advanced Ceramics* ,Vol.2, Academic Press ,London UK, 187.

7. K W Wagner, Ann. Physics, 40, (1913), 817

8. C G Koops Physical Review, 83, (1951), 121

9. T M Meaz, S M Attia, A M Abo El Ata, J. Magn. Mag. Mater. 257 (2003) 296

10. B Vishwanathan, V R K Moorthy, *Ferrite Materials :Science and Technology*, Springer Verlag 1990

11. Debye P *Polar molecules* Dover New York 1929

12. Cole K.S and Cole R.H, J. Chem. Phys., 9, (1941), 34.

13. A.M Abdeen, Journal of Magn.Mag.Mat, 192, (1999), 121.

14. D J Fatemi,V G Harris,M X Chen,S K Malik, W B Yelon G J Long A Mohan J. Appl. Phys., 85, (1999), 5172.

15. Razet A, Metrologia, 35, (1998), 143.

16. Hari Singh Nalwa, *Encyclopedia of Nanoscience and Nanotechnology*, American Scientific Publishers, Volume 2, (2004) 371

17. H Fang, B Chen, K Jiang, J Sha,Z Jiao, Q Zhang and L Zhang ,Phys Status Solidi B 192, (1995), K11.

18. Z   P A Miles, W B West Phal and A.Von Hippel , *Reviews of modern Physics*, 29, (1957), 279.

19. N Rezlescu, E. Rezlescu, Physica Status Solidi(a) 23, (1974), 575.

20. Mellisa. A Denecke, W Gun Ber, G Buxbaum, P Kuske, Materials Research Bulletin, 27, (1992), 507.

21. A M Abo El Ata and S M Attia, J. Magn. Mag. Mat, 257, (2003), 165.

22. H M Zaki, Physica B, 363, (2005), 232.

23. S A Mazen F Matawe and S F Mansour, Journal of Physics D: Applied Physics, 30, (1997), 1799.

24. M I Klinger, Journal of Physics C, 8, (1975), 3595.

25. M A Ahmed; M A El Hiti; M K El Nimr and M A Amer., J. Magn. Magn. Mater, 152,(1996) 391.

26. M A El Hiti. Journal of Physics D: Applied Physics, 29, (1996), 501.

27. S R Elliot. Advances in Physics, 36, (1987) 135.

28. M K Fayek ; M F Mostafa; F Sayedahmed; S S Ata Allah and M Kaiser, J. Mag. Mag. Mat, 210, (2000)189.

29. T M Meaz, S M Attia, A M Abo El Ata J. Magn. Magn. Mater, 257, (2003), 296.

30. Aswini Ghosh, Physical Review B, 42,(1990), 1388

31. I G Austin and N F Mott, Advances in Physics, 19, (1969), 41.

32. S R Elliot, Philos.Magn., 36, (1977), 12.

33. A R Long , Advances in Physics, 31, (1982), 553.

34. I H Gul; A Z Abbasi; F Amin; M Anis ur Rehman and A Maqsood . *J .Magn. Magn .Mate.r*, 311,(2007) 494

35. M A Ahmed; M K El Nimr and A A El-Hasab, Phys. Stat Sol (a), 123, (1991), 501.

36. A J Bosmon and H J Van Dall, Advances in Physics, 19 ,(1970), 1

37. G. J. Snyder; R. Hiskes; S. Di Carolis; M. R. Beasley and T. H. Geballe, Phys. Rev. B, 53, (1996), 14434.

Chapter 5

Structural, Magnetic and Electrical Properties of Sol-gel derived Cobalt Ferrite Nanoparticles

Nanoparticles of cobalt ferrite were synthesized by sol gel method. These particles were structurally characterized by using XRD, TEM and ICP and the results confirmed the formation of spherically shaped nanoparticles of cobalt ferrite having a size lying in the range of 13- 14 nm. The as prepared sample was sintered at 800°C and the structural, magnetic and dielectric properties were measured. The magnetic properties were examined considering the high magnetocrystalline anisotropy associated with cobalt ferrite. The dielectric properties were studied and analyzed as a function of temperature and frequency. The ac and dc conductivity studies were carried out to delve into the conduction mechanism involved. Existing models based on quantum mechanical tunneling was effectively employed to explain the frequency dependent conductivity.

Cobalt ferrite is an important member of the ferrite family and is characterized by its high coercivity, moderate magnetization and very high magnetocrystalline anisotropy. Cobalt ferrite finds innumerable applications in stress sensors, as precursors for making ferrofluids and also as magnetic refrigerants [1,2].Normally, ferrites become superparamagnetic at room temperature for nanoparticles below 10nm [3,4]. However, cobalt ferrite nanoparticles do not show superparamagnetic behaviour unless they are made significantly smaller [5]. The critical size for the transition to superparamagnetic state appears to be around 5nm .This is due to the large crystalline anisotropy associated with cobalt containing compounds. Strong electron coupling at Co^{2+} lattice sites leads to large magnetic anisotropy which in turn gives rise to such magnetic property [6, 7]. For bulk $CoFe_2O_4$, cubic anisotropy is known to dominate since the orbital contribution is not quenched by the lattice.

Bulk particles of cobalt ferrite exhibit an inverse spinel structure with one half of the Fe^{3+} ions in the A-sites and the remaining half of Fe^{3+} ions and Co^{2+} ions in the B sites and can be represented as $Fe^{3+}_A [Co^{2+}, Fe^{3+}]_B$ Nanocrystalline cobalt ferrite particles are found to be exhibiting interesting structural and magnetic properties as compared to their micron sized counterparts[8]. The presence of cobalt ions in the tetrahedral sites coupled with the existence of multiple oxidation states of cobalt (Co^{2+}/Co^{3+}) can give rise to altogether different structural and magnetic properties with respect to their bulk counterparts. It has been reported recently that spin disorder on the surface of the cobalt ferrite nanoparticles leads to interesting magnetic phenomena [9].The electrical properties exhibited by cobalt ferrite in the micron regime are normally characteristic of hopping of electrons or holes or polarons between cationic sites [10]. Thus the cation distributions as well as the oxidation states of the cations also determine the dielectric polarisation and electrical conduction. Jonker studied the electrical properties of a series of bulk $Co_{3-x} Fe_x O_4$ and observed that the conductivity is minimum for the composition corresponding to x= 2 and that is a

p-type conductor for x less than 2 and n-type conductivity for x greater than 2 [11]. The p-type behaviour was explained as due to the enhanced contribution of hole hopping between Co^{3+}/Co^{2+} ions in cobalt rich phase.

Though the magnetic properties of cobalt ferrite in the nanoregime has been extensively investigated, reports on the electrical properties of nanosized cobalt ferrite is not very abundant in the literature. The role of cations, the cation redistribution, if any in the nanoregime, the presence of more than one valence state for the cation states and their influence on the electrical properties are seldom understood when the particle sizes approach the nanometric dimensions. This is an area where there is scope for understanding the basic mechanism of conduction in cobalt ferrite in the nanoregime. Understanding of the mechanism of conduction both in the ac and dc regime will be abundantly useful in tailoring the properties of these materials for specific applications. Such a study on cobalt ferrite nanoparticles needs the synthesis of phase pure $CoFe_2O_4$. For this, pristine sample was prepared using sol-gel method and was thermally treated at 800°C in order to have phase pure compound. They were characterized both structurally and magnetically. The ac and dc conductivities were also measured and analyzed. The properties of the sintered as well as the as prepared samples are compared wherever needed.

5.1 Synthesis

Fine particles of Cobalt ferrite were synthesized by sol-gel combustion method. For this, cobalt nitrate and ferric nitrate of AR grade chemical precursors were used with ethylene glycol as the solvent. Cobalt nitrate and ferric nitrate were dissolved in ethylene glycol in the molar ratio of 1: 2 at 40°C to form the sol. This sol is then heated slowly at 60°C to obtain a wet gel. The gel was then dried at 90°C. This resulted in the self ignition of the gel producing a highly voluminous and fluffy product .The product is then ground to form fine powders

of cobalt ferrite and pelletised. They were sintered in the furnace at 800°C. The unsintered and sintered samples are designated as CP and C8.

5.2 Structural Properties

The XRD patterns of nanoparticles of pristine and sintered sample are depicted in figure 5.1 and are typical of a spinel structure. Additional peaks of α-Fe_2O_3 were found in the pristine sample. The average size of the crystallite, calculated using Debye Scherrer formula 13.8nm. The lattice parameter 'a' for the pristine sample was found to be 8.413 Å. It should be noted that the lattice parameter of the bulk cobalt ferrite is 8.391Å (ICDD–file No: 22-1086). A sharp increase in the crystalline nature of cobalt ferrite powder is observed as the firing temperature was increased to 800^0C which is recorded as a decrease in the broadening of the peaks in the diffraction pattern. This clearly indicates that the grain size has increased with sintering. The grain size of the heat treated sample was estimated to be 40 nm. The details are given in table 5.1.

The TEM micrographs of the pristine sample (figure 5.2(a) and (b)) show the formation of uniform spherical shaped ferrite nanoparticles. The mean particle size determined from TEM 13 nm and is in agreement with the grain size obtained using XRD analysis (13.8nm). The HRTEM image in figure 5.2 (b) clearly depicts the crystal planes corresponding to cobalt ferrite. The EDS spectrum (figure 5.3) of pristine cobalt ferrite sample indicate that Co: Fe ratio is 1: 2 and hence the loss of ferric or cobalt ion is ruled out. Scanning electron micrographs of the samples are depicted in figure (4.4). The grain growth at higher sintering temperature for C8 is clearly evident from the SEM images. The grains in the pristine sample can be viewed from the two dimensional and three dimensional AFM images of the pellet (figure 5.4(a) and (b))
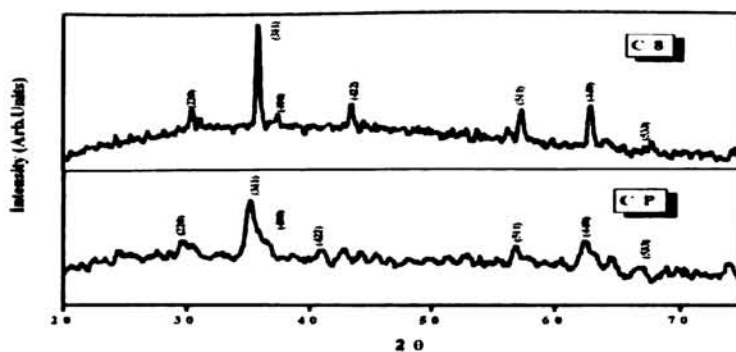
Figure 5.1 XRD diffraction patterns of cobalt ferrite: as prepared (CP) and sintered (C8)
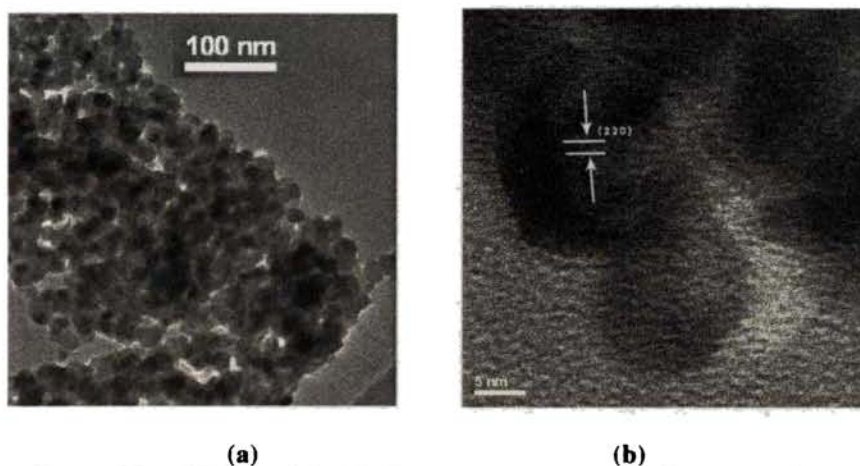

(a)

(b)

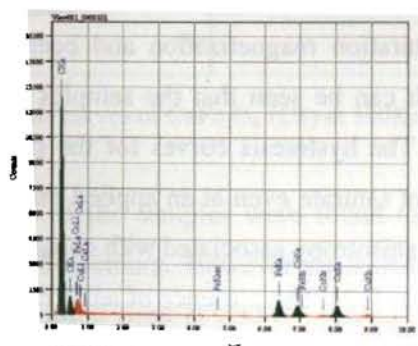**Figure 5.2 (a)** TEM and **(b)** HRTEM images of cobalt ferrite nanoparticles

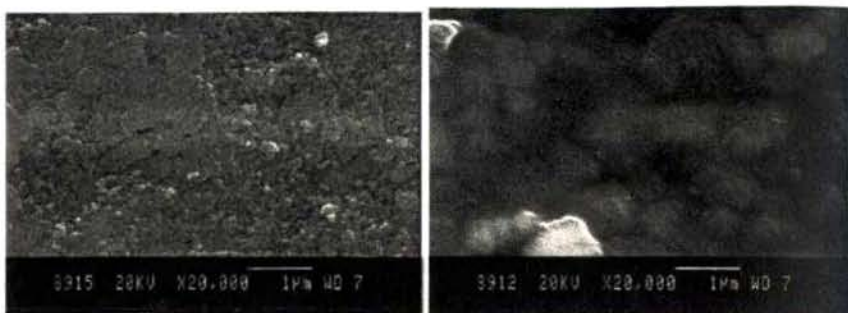**Figure 5.3** EDS pattern of pristine cobalt ferrite

137

Figure 5.4 SEM images of CP and C8
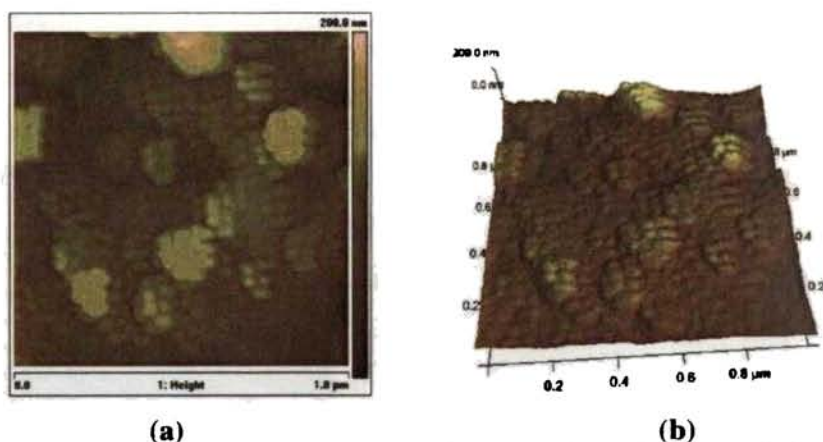

| (a) | (b) |

Figure 5.5 Surface morphology of cobalt ferrite nanoparticles (CP) from AFM
(a) 2D and **(b)** 3D image

5.3 Magnetic Properties

Figures 5.6 and 5.7 shows the hysteresis curves for the $CoFe_2O_4$ particles measured at room temperature (300K) and at low temperature (100K). The loop parameters like saturation magnetization and coercivity are estimated and are given in table 5.1.It can be seen that the samples are not superparamagnetic at room temperature. The hysteresis curves for the pristine samples (CP) at room temperature does not saturate even at an applied magnetic field of 13.5kOe. High magnetocrystalline anisotropy associated with cobalt ferrite will be contributing to this type of behaviour [12] .The presence of antiferromagnetic impurities will also

impede the sample from being saturated. The loop opened up at 100K and the coercivity was found to be increasing at low temperatures.
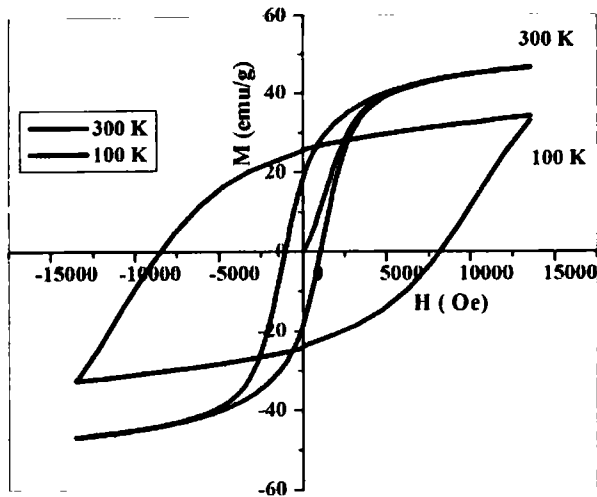

Figure 5. 6 Hysteresis curves of $CoFe_2O_4CP$ at 300Kand 100K
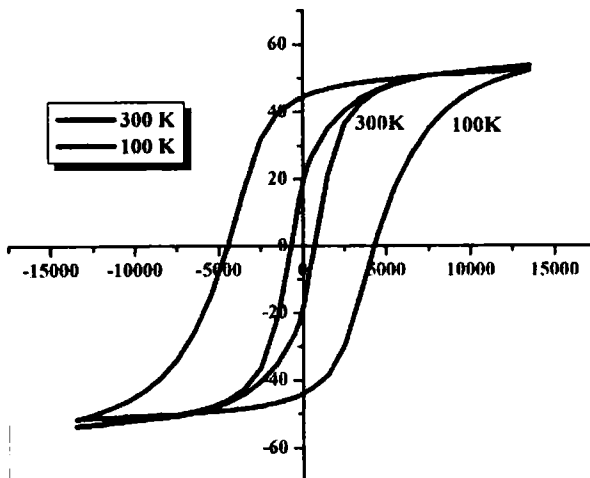

Figure 5.7 Hysteresis curves of $CoFe_2O_4$ (C8) at 300Kand 100K

Magnetisation values of the samples were found to be lower than the corresponding bulk value of 80.8emu/g. However an increase in magnetization (M_s) was observed for the sample fired at 800°C because of its monophasic nature. The coercivity observed in the case of sintered sample was around 700Oe

at 300K which is less than that of pristine sample. The variation of H_c with particle size can be explained on the basis of domain structure, critical diameter and the anisotropy of the crystal. The decrease in coercivity with increase in particle size is attributed to its change from the single domain characteristics to to multidomain nature. The ratio of M_r/M_s throws light on the exchange interactions and magnetocrystalline anisotropy associated with the ferrite nanoparticles [13]. According to Stoner Wohlfarth model [14], a theoretical value of M_r/Ms is 0.5 for non interacting uniaxial single domain particles with the easy axis being randomly oriented. M_r/M_s value observed is found to be 0.41 for the pristine samples.

CoFe₂O₄	Grain size (nm)	Porosity %	Ms at 300K (emu/g)	Mr/Ms at 300K	Mr/Ms at 100K (emu/g)	Hc at 300K (Oe)	Hc at 100K (Oe)	Tc K
CP	14	31	48	0.41	0.66	1080	8500	771
C8	40	9	56	0.33	0.82	700	4500	808

Table 5.1 Structural and magnetic parameters of Cobalt Ferrite Samples

Hence CP exhibit uniaxial anisotropy. However the squareness ratio at room temperature decreases in the case of C8 indicating the formation of multidomain particles. There is an increase in M_r/M_s values measured at 100K with firing temperature. This points towards the increase in magnetocrystalline anisotropy associated with decreased temperature. The maximum M_r/M_s value is found to be 0.82 indicating the enhanced contribution from cubic anisotropy (higher order terms of magnetocrystalline anisotropy) at lower temperature. Hence a large coercivity can be expected at lower temperatures.

The T_c values of the samples of cobalt ferrite were evaluated from M-T curves (figure 5.8) and are listed in table. The T_c values are found to be similar to that of bulk cobalt ferrite (790K).However a decrease in T_c is obtained with decrease in particle size. This observation is consistent with the reported studies on the finite size effect on T_c in ferrite nanoparticles. A broad transition at around 150-350K is clearly visible from the M-T curve of pristine sample.
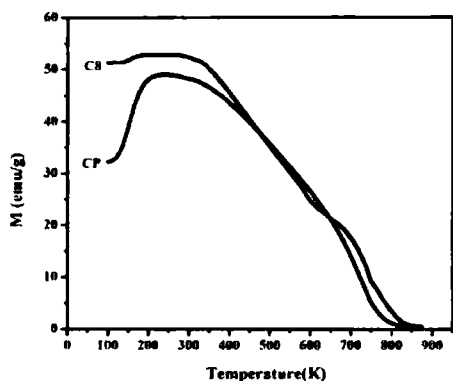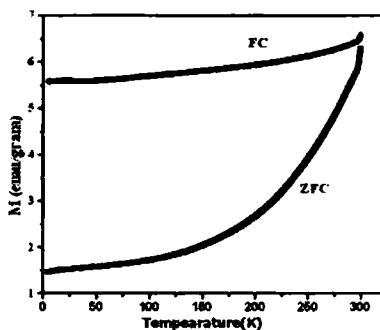

Figure 5.8 M-T curves for CP and C8

Figure 5.9 FC-ZFC curve for CoFe$_2$O$_4$ (CP)

The FC –ZFC curve for the pristine powder is shown in figure 5.9. However the blocking temperature of cobalt ferrite nanoparticles seems to be above room temperature.

The relatively larger blocking temperature can also be due to large anisotropy contributions in cobalt ferrite nanoparticles. The TEM measurements reveal the nearly spherical nature of the cobalt ferrite nanoparticles. Hence the contribution from surface and shape anisotropy cannot be expected in this case while the presence of uniaxial anisotropy is obvious from the squareness ratio. The shape of the FC branch is rather flat showing a temperature independence which results as a result of sizable interaction or aggregation effects resulting from dipolar interactions. Subsequently the presence of uniaxial anisotropy and strong dipolar interactions directly influences the magnetic characteristics of cobalt ferrite.

5.4 Electrical Properties

5.4.1 Dielectric Properties

The variation of dielectric permittivity with frequency is depicted in figure 5.10 (a-b). It can also be seen that the dielectric permittivity decreases continuously with increasing frequency as expected. The greater the polarisability of the molecules, the higher is the permittivity of the material. The dispersion occurring in the lower frequency regime is attributed to interfacial polarization since the electronic and atomic polarizations remain by and large unchanged at these frequencies. As the size of the particle decreases to the nanometric dimensions, interfacial polarization plays a major role in determining the dielectric properties of the material [15]. In the high frequency regime the decrease in the value of dielectric permittivity is very small. Any mechanism of polarization contributing to polarisability is observed to show a lagging with the applied field at these frequencies. This can result in reduced polarization leading to diminished ε' values at higher frequencies. The dielectric dispersion can be explained satisfactorily on the basis of Maxwell Wagner theory of interfacial polarization [16,17] in consonance with the Koops Phenomenological theory as in the case of manganese zinc mixed ferrites[chapter 4].

If one invokes the Rezlescue Model [18], the polarization can be explained based on conduction process which involves the electron hopping between Fe^{2+}-Fe^{3+} pairs and hole hopping between Co^{2+}-Co^{3+} in the octahedral sites. At higher frequencies, the frequency of electron / hole exchange will not be able to follow the applied electric field thus resulting in a decrease in polarization. Consequently the dielectric permittivity attains a constant value at higher frequencies. It has been reported that the conductivity of a polycrystalline material in general increases with increasing particle size. Smaller grains imply smaller

142

grain to grain surface contact area and therefore a reduced electron flow [19]. Thus the observed increase in dielectric permittivity   of sintered sample can be attributed to the increase in particle size with respect to the as prepared sample.
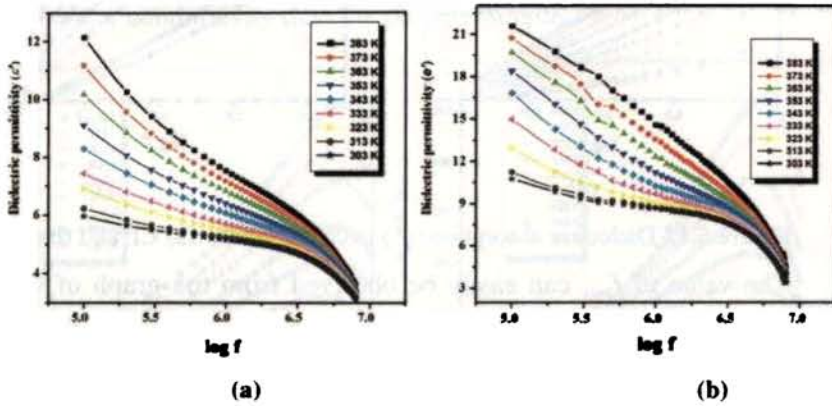

(a)   (b)

Figure 5.10 Dielectric dispersion in cobalt ferrite (a) CP and C8

The variation of tan δ and ε" are depicted in figure 5.11(a-b) and figure 5.12(a-b). It can be seen that although a relaxation is obtained in the tanδ values a relaxation in the dielectric absorption is seldom seen. But the relaxation is found to broader than that observed in manganese zinc ferrites. From the relaxation peaks for tanδ the activation energy for relaxation can be evaluated.

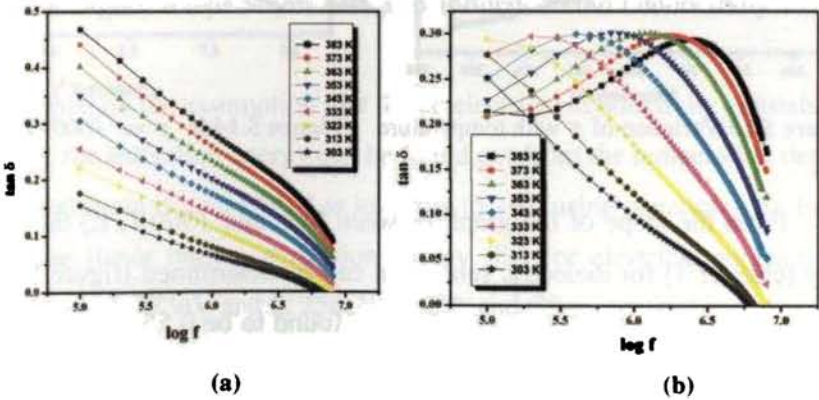(a)   (b)

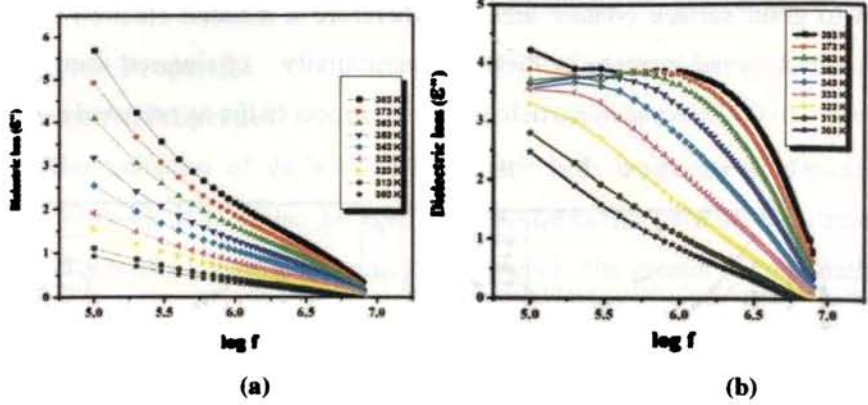**Figure 5.11** Variation of tan δ with frequency (a) CP and C8

Figure 5.12 Dielectric absorption (ε") in cobalt ferrite (a) CP and (b) C8

The value of f_{max} can easily be observed from the graph of C8 and the relaxation time τ can be determined from equation (4.2). The variation of τ with temperature is shown in figure (5.13).
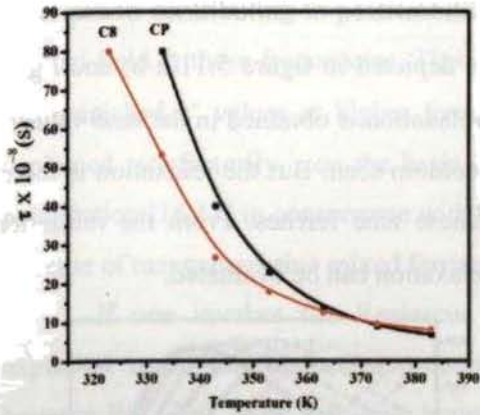

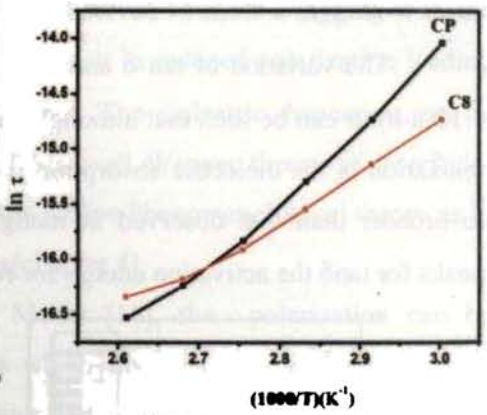**Figure 5.13** Variation of τ with temperature   **Figure 5.14** ln τ vs $1000/T$

From the slope of the graph between $ln\tau$ and $1000/T$, E_d the activation energy [chapter 4] for dielectric relaxation can be determined (figure 5.14). The activation energy for dielectric relaxation is found to be 0.55eV for C6 and 0.37 eV for C8.

5.4.2 AC conductivity Studies

The variation of ac conductivity with frequency and temperature is depicted in figure 5.15(a-b). It is observed that the ac conductivity first increases with frequency, reaches a maximum and then decreases. The sintered samples exhibited higher conductivity than the pristine sample.
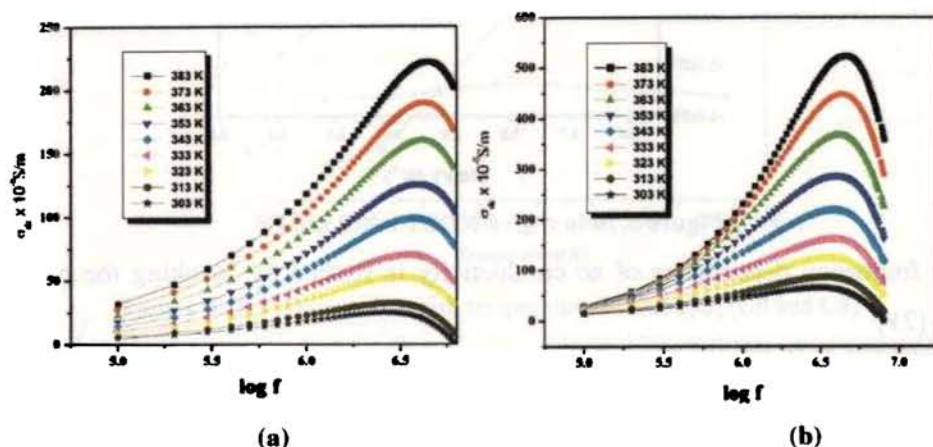

Figure 5.15 σ_{ac} variation with frequency and temperature (a) CP and (b) C8

When the grain size increases, intergranular porosity decreases, eventually resulting in an increase in conductivity as observed in the case of sintered sample. However heat treatment yielded chemical homogeneity which may also influence the transport properties. The formation of Co^{3+} ions during sintering at higher temperatures can also influence the conductivity to a great extent.

Based on the assumption that the ac electrical conductivity consists of two terms [20], the activation energy can be found out from the temperature dependent term by plotting ln σ_{ac} vs 1000/T as in figure (5.16) (using equation 4.3). From the slope of the linear region, activation energy (E_a) for electrical conduction was estimated to be 0.273eV and 0. 256eV for CP and C8 respectively.
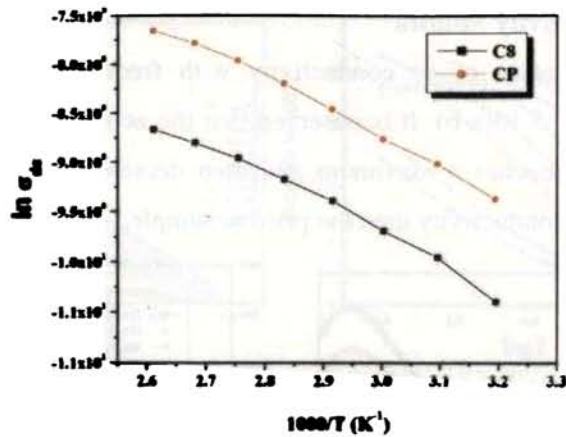
Figure 5.16 ln σ_{dc} vs 1000/T in CP and C8

The frequency dependence of ac conductivity is studied by invoking the power law [21]

$$\sigma_2(\omega,T) = B(T)\omega^n(T) \tag{5.1}$$

The *log σ_{ac} vs log ω* plots of CP and C8 are given in figure 5.17 (a-b). It can be found that the parallel straight lines where obtained for CP while the slope increases with temperature in C8. For CP the frequency exponent '*n*' is found to be almost temperature dependent and lies around 0.6 while for the other two sample it varied between 0.5 -0.98 for the temperature variation (figure 5.18).
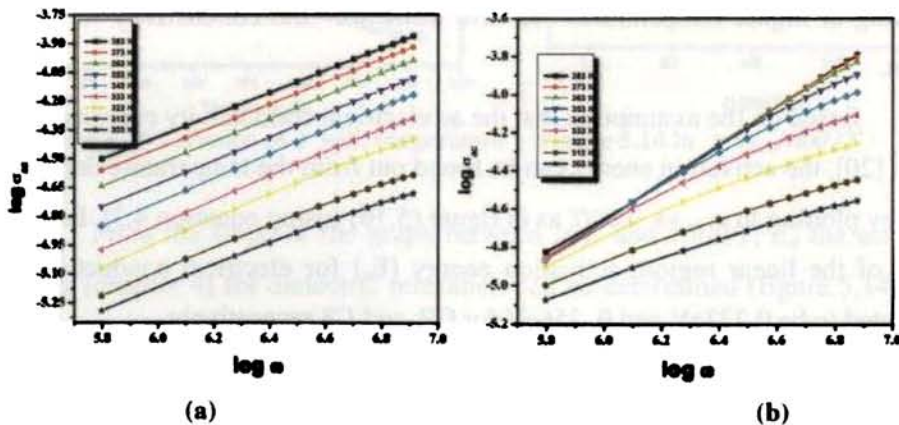

(a)   (b)

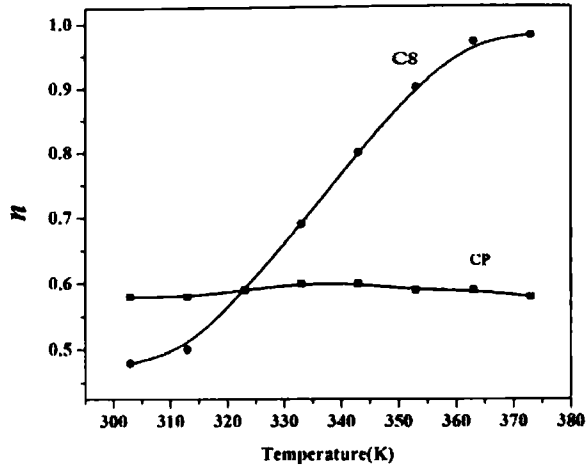**Figure 5.17** log σ_{ac} vs logω in (a) CP and (b) (C8)

Figure 5.18 Variation of n with temperature in $CoFe_2O_4$ (CP and C8)

Depending on the variation of n with temperature the mechanism of ac conduction in the ferrite samples Cp and C8 are modeled [22,23]. In that case where n is temperature independent, quantum mechanical tunneling is expected. That is we can propose quantum mechanical tunnelling in the pristine sample[24]. By simple quantum mechanical tunneling model, the expression for n is given by the equation [25]

$$n = 1 - \frac{4}{\ln\left(\dfrac{1}{\omega\tau}\right)} \tag{5.2}$$

This equation gives a temperature independent value for n. Hence Quantum mechanical tunneling is the most probable mechanism in the pristine sample where we have observed a temperature independent behaviour of n.

In the case of sintered sample we have got a temperature dependent n .A temperature dependent frequency component n can be obtained within the frame work of quantum mechanical tunneling model in the pair approximation by assuming that the charge carriers are non overlapping small polarons. The model predicts a temperature dependent frequency component is given by equation (4.5)

147

[26] and n increases with increasing temperature. This type of behaviour is obtained for samples sintered at higher temperatures. The formation of small polaron may be due to the defect levels or oxygen vacancies created during sintering. According to the model, the ac conductivity is given by equation (4.6) [27].Thus the conduction mechanisms in the two samples are explained based on the quantum mechanical tunneling models. Quantum mechanical tunneling is found suitable for the pristine sample while small polaron conduction is the proposed mechanism in the sintered sample.

5.4.3 DC Conductivity Studies

The temperature dependence of dc conductivity in cobalt ferrite is studied for different grain sizes. The dc conductivity for the pristine sample was found to be 10^{-6} S/m while that of C8 was 10^{-5} S/m from CP to C8.The variation of conductivity with temperature shows the semiconducting nature of the ferrites (figure 5.19).
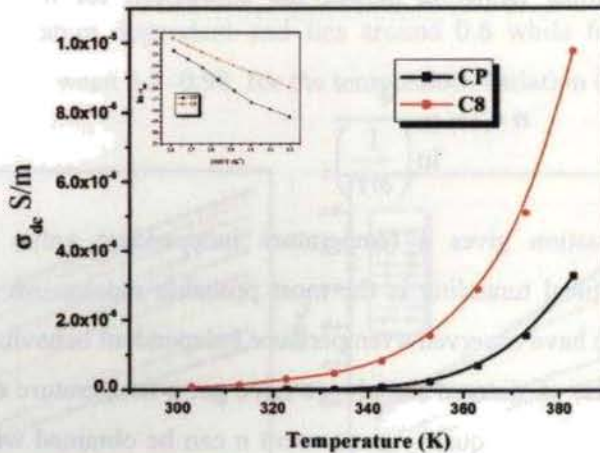

Figure 5.19 σ_{dc} vs temperature (log σ_{dc} vs 1/T given as inset)
of CoFe$_2$O$_4$ samples (CP and C8)

The conductivity in cobalt ferrite is found to be smaller than that observed in $MnFe_2O_4$. By the electron hopping model, it is presumed that the conductivity is mainly due to the hopping of electrons between Fe^{2+} and Fe^{3+} ions present at octahedral B sites[28]. In addition to this the presence of Co^{3+} ions if any at B sites may also initiate hole hopping between Co^{3+} and Co^{2+} ions and thus may have small contribution to conductivity. Since Fe^{2+} and Co^{3+} ions have a strong preference for B sites, they can produce n-type and p-type conductivity respectively. Hence the conductivity will depend on the availability of charge carriers and their mobility. However not much increase is obtained in our sample with sintering. This may be due to unavailability of charge carriers for conduction and also due to reduced mobility of the charge carriers. The activation energy for conduction calculated from the Arrhenius plot (inset of figure 5.19) is found to be very high 0.9eV for pristine sample and 0.63eV for the sintered one indicating the high resistive nature of cobalt ferrite. Large values of activation energy points towards a polaron conduction [29].
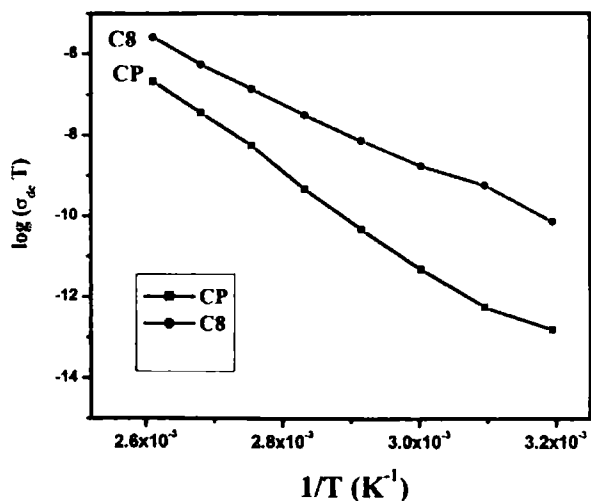

Figure 5.20 $log\sigma_{dc}T$ vs $1/T$ $CoFe_2O_4$ Samples (CP and C8)

The mobility μ of the charge carriers was calculated from the experimental values of the electrical resistivity and carrier concentration using the same approach used in chapter 4 .The mobility is found to be in the range 10^{-10} cm^2/V.s. which is comparable to the mobility of polarons.

Further, in order to check whether the conduction process obeys Small Polaron Hopping, a graph is plotted with log σT on the Y-axis and 1/T on the X-axis (figure 5.20).We obtained straight lines confirming the small polaron conduction nature of cobalt ferrite.

5.5 Conclusion

The structural, magnetic and electrical properties of sol-gel derived cobalt ferrite nanoparticles are presented. The temperature variation of dc conductivity indicated the semiconducting behaviour of the ferrite .The variation in the dielectric properties as a function of temperature and frequency has been explained on the basis of Maxwell Wagner theory of interfacial polarization and also by Rezlescue model. Activation energies were calculated from the temperature dependence of ac conductivity and the frequency component 'n' is estimated from the relation $\sigma_{ac}=B\,\omega^n$. The variation of 'n' with temperature suggests a quantum mechanical tunneling conduction for pristine sample. The theory of small polaron tunneling which is a modification of Quantum mechanical tunneling was found to be suitable for explaining the ac conductivity in samples sintered at higher temperature. Hence it can be concluded that the reduced number of hopping charge carriers and reduced mobility of the localized charge carriers in nanosized cobalt ferrite resulted in tunneling conduction.

References

1. S .Kückelhaus, . A. C Tedesco, D. M Oliveira, P. C. Morais, G. R Boaventura, Z. G. M Lacava, . J. App. Physics, 97, (2005)10Q910 .

2. Srikanth Hariharan , James Gass, Rev. Adv. Mater. Sci. 10, (2005) 398.

3. Joong-Hee Nam, Won Ki Kim Sang Jin Park, Phys. Status Solidi (a) ,201,(2004) 1838

4. Chao Liu , , Z John Zhang, Chemistry of Materials, 13 (2001) 2092.

5. Qing Song , Z. John Zhang, J. Phys Chem. B,110 (2006) 11205

6. Adam J Rondinone , Anna C S Samia , Z John Zhang, J. Phys.Chem.B , 103(1999)6876

7. L. D. Tung, V. Kolesnichenko, D. Caruntu, N. H Chou, C. J. O'Connor, L.Spinu , J. Appl. Physics 93(2003) 7325.

8. N. Sivakumar, A. Narayanasamy, K Shinoda,   C. N Chinnasamy, B Jeyadevan, J.M Greneche,. J.App. Phy. 102, (2007) 013916

9. C. T. Hsieh and J. T. Lue Physics Letters A 316, 2003, 329

10. A.J. Bosmann , C. C.Creve, Phys. Rev. 144 (1966)763.

11. G. H. Jonker, J. Phys. Chem. Solids., 9(1959) 165.

12. B. G.Toksha, Sagar .E .Shrisath, S.M. Patange and K.M. Jadhav ,Solid State Communications 147 (2008) 479

13. CN Chinnasamy, B Jeyadevan, K Shinoda, K Tohji, DJ Djayaprawira, M Takahashi, Appl. Phy. Let. 83(2003) 2862

14. E. C. Stoner , E. P. Wohlfarth, Philos. Trans. R. Soc. A 240, (1948) 599

15. Mathew George, Swapna S Nair, K.A Malini, P. A Joy and M. R Anantharaman Journal of Physics D: Applied Physics,,40(2007) 1593.

16. K.W. Wagner, Ann. Physics , 40(1913) 817.

17. C.G. Koops Physical Review,83(1951) 121.

18. N Rezlescu, E. Rezlescu . Physica Status Solidi(a), 23 (1974) 575.

19. G. P. Kramar Ya. I. Panova, V .V. Passynkov Phys Stat Sol (a) ,76(1983)95

20. M.A. Ahmed, M .A .El Hiti, M.K. El Nimr, M .A. Amer J. Mag. Mag. Mat. 152 (1996) 391.

21. M.A. El Hiti, Journal of Physics D: Applied Physics 29 (1996)501.

22. M K Fayek ,M F Mostafa, F Sayedahmed, S S AtaAllah, M Kaiser, Journal of magnetism and Magnetic Materials 210 (2000) 189.

23. S.R. Elliot, Advances in Physics 36 (1987)135

24. I .G. Austin ,N. F. Mott, Advances in Physics 19 (1969) 41.

25. T.M. Meaz,, S. M. Attia, A. M. Abo El Ata , Journal of magnetism and Magnetic Materials 257 (2003)296.

26. K K Som ,B K Chaudari, Phy.Rev.B,41(1990) 1581.

27. S Bhattacharya ,A Ghosh,Phy.Rev.B,68(2003) 224202.

28. Matthieu Jamet, Wolfgang Wernsdorfer, Christophe Thirion, Véronique Dupuis, Patrice Mélinon Alain Pérez , Dominique Mailly, Phys. Rev. B ,69 (2004) 24401

29. E Veena Gopalan ; K A Malini; S Saravanan, D Sakthi Kumar; Yasuhiko Yoshida and M R Anantharaman., Journal of Physics D: Applied Physics, 41(2008)185005

Chapter 6

Template Assisted Synthesis and Characterization of Self protected Nickel/Iron Nanoparticles *via* Ion-Exchange Method

Self protected nickel and iron nanoparticles were synthesized by a novel method of ion-exchange reduction in two different polymer matrices namely strongly acidic cation exchange resin and weakly acidic cation exchange resin. The composites were cycled repeating the loading reduction cycle involved in the synthesis procedure. The X-Ray Diffraction, Scanning Electron Microscopy and Transmission Electron microscopy were effectively utilized to investigate the different structural properties of the nanocomposites. The elemental analysis was conducted using Energy Dispersive Spectrum and Inductively Coupled Plasma Analysis. The hysteresis loop parameters namely saturation magnetization, remnant magnetisation and coercivity were measured using Vibrating Sample Magnetometer. The thermomagnetisation study was also conducted to evaluate the Curie temperature values of the composites. The effect of cycling on the structural and magnetic characteristics of the two composites are dealt in detail. A comparison between the different characteristics of the two nanocomposites is also provided. It is possible to tune the properties of these composites for possible applications.

Metal nanoparticles are of great interest because they exhibit interesting optical, electronic, magnetic and chemical properties. They find potential applications in various optoelectronic devices, as catalysts in chemical reactions and also as biosensors [1-4]. Synthesis of metal nanoparticles either in the form of independent entities or in matrices then assume significance and are of interest to chemists and physicists alike. Preparation of nanoparticles of Fe/Ni/Co is not very easy and hence novel methods and alternate routes are normally scouted for. The large surface area of unprotected nanoparticle is prone to oxidation and thus conventional methods for the synthesis of metal nanoparticles are not feasible. Self protected metal particles embedded in host matrices are thus a viable alternative. Stabilization of metal nanoparticles by employing capping agents or coating with surfactants are usually adopted [5,6]. The fabrication of polymer stabilized metal nanopartcles is a promising solution to the metal nanoparticle instability and thus they attract the attention of material scientists and technologists [7-8]. The areas of practical applications of metal – polymer composite are in spin polarized devices, sensors [9], carriers for drug delivery [10] and in catalysis [11].

Nickel /Iron nanoparticles embedded in a polymer matrix are important not only from a commercial point of view but they are also important from a fundamental perspective. They are ideal templates for studying the size effects on the magnetic properties. The optical properties of these particles at the nanolevel also assume significance. The interaction between metal nanoparticles embedded in a polymer matrix can also be an interesting topic of investigation. The method of ion exchange has been employed for the incorporation of metal oxide nanoparticles in the host matrix. Sulfonated polystyrene was employed by Ziolo *etal.* [12-13] for the preparation of $\gamma-Fe_2O_3$ way back in 1992. However reports employing the method of ion exchange for the preparation of passivated metal particles are not very common.

A wide variety of methods are adopted for the fabrication of metal polymer composites which include both physical and chemical techniques. Examples of physical methods are cryo-chemical deposition of metals on polymeric supports and simultaneous plasma induced polymerization and metal evaporation techniques [14]. The chemical methods mainly include the reduction of metal inside the polymer *i.e.*, the intermatrix synthesis of these composites [15].

Mesoporous ion exchange resins were employed to prepare polystyrene γ-Fe_2O_3 nanocomposites with magnetic functionality [12-13]. The size of the magnetic oxide can be predetermined depending on the choice of the particular resin which is again graded according to the channels in the porous resin .Then a judicious choice of the polymer matrix determines the size of the oxide particle. This work caught the imagination of many researchers and various metal oxide polymer nanocomposites were prepared [16-18]. The availability of various ion exchange resins commercially were an added attraction to these researchers. However, for the fabrication of metal- polymer composites, a different route has to be adopted. For example, mesoporous ion exchange resins can be a template matrix where suitable metal ions are anchored to the functional resins followed by their subsequent reduction inside the polymer network. This method is generally known as the ion exchange reduction process.

Ion exchange resins have been classified based on the charge on the exchangeable counterion (cation –exchanger or anion exchanger) and the ionic strength of the bound ion (weak and strong) .Ion exchange resins are manufactured in two physical structures, gel or microporous [19]. Gel type resins are homogenous, have no discrete pores, the channels act as pores while macroporous resins are referred to as fixed pore resins. In the present investigation we report the synthesis of nickel and Iron nanoparticles inside strongly acidic gel type and weakly acidic macroporous ion exchange resins.

Metal polymer nanocomposites containing nickel and iron nanoparticles can be synthesized by the method of reduction using two different templates namely, strongly acidic cation exchange resin and weakly acidic cation exchange resins. Since both strong and weak resins are characterized by their channels and pores respectively, the overall properties of the composite need not be identical *vis a vis* the nature of the embedded nano metal inside the matrix, the impurity phase etc. This investigation is an attempt to synthesize nickel nanocomposites using two different matrices having different functional groups and different structures and to study their structural and magnetic properties with a view to optimizing the method of synthesis by cycling to increase the net magnetization of the nanocomposite. The exact determination of the amount of nickel on the composite is also important. So compositional analysis using techniques like Inductively Coupled Plasma Analysis (ICP) /Energy Dispersive X-ray Spectrum Analysis (EDS) enables one to determine the exact composition of nickel in the synthesized nanocomposites. The morphological and structural aspects were investigated using X-Ray diffraction, Transmission Electron Microscopy and Scanning Electron Microscopy. The effect of cycling on the magnetic properties of these composites form another objective. Hence a complete study on the nanocomposites is undertaken in the present investigation.

The motivation of the present study is not only to synthesize self protected Nickel/Iron nanoparticles in a porous network having two structures, but also to investigate how the structural and magnetic properties differ in these two matrices. Well separated nickel/iron nanoparticles are a subject of intense interest to physicists because they mimic the characteristics of a non interacting magnetic system. So an ensemble of noninteracting magnetic metal nanoparticles is of importance from a basic research perspective. From an applied standpoint, they are potential materials for various applications like catalysis, magnetic recording, giant magnetoresistance and magnetic refrigeration.

6.1. Synthesis of metal polystyrene nanocomposites

The ion exchange resins in the form of beads are basically functionalized polystyrene which are cross linked with divinyl benzene having a three dimensional porous polymer matrix. The strongly acidic resins (gel type) are functionalized with sulfonic acid group while the weakly acidic resins (macroporous) are functionalized using carboxylic acid groups (figure 6. 1 and figure 6.2) .Both these resins are 8% cross linked polymer of polystyrene and divinyl benzene, which have exchangeable H^+ ions associated with their respective functional groups.
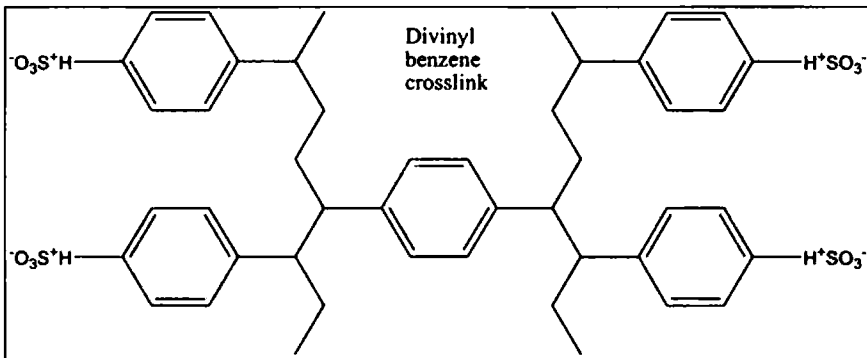

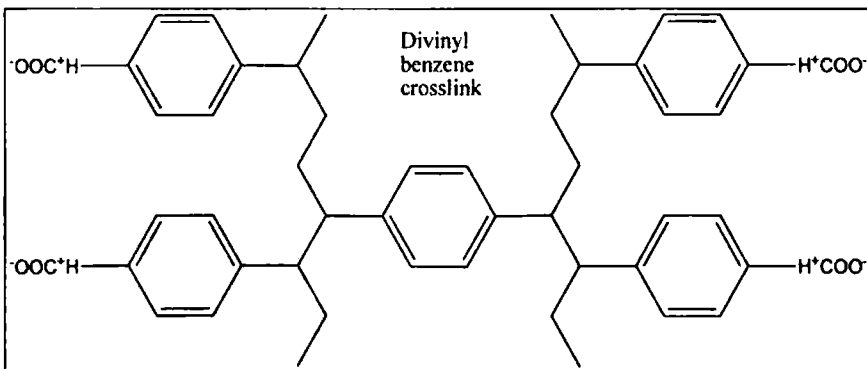**Figure 6.1** Strongly Acidic Cation (SAC) exchange resin

Figure 6.2 Weakly Acidic Cation (WAC) exchange resin

The presence of functional groups in the polymer matrix permits us to load them with metal cations by using conventional ion exchange mechanism. For

the preparation of nickel polystyrene nanocomposites, SRC-120 (Amberlite IRC-120), WRC-50 (Amberlite IRC-150) were initially soaked for 24 hours in distilled water so that they are swollen. A saturated solution of 1M $NiSO_4$ (Merck) is filled in a reaction column along with soaked resin for about 24 hours. The ion exchange process is initiated at this stage. The Ni^{2+} ions are exchanged with the H^+ ions in the resin. Further reduction of Ni^{2+} ions to Ni inside the polymer matrix occur with the addition of $NaBH_4$. Dilute solution of $NaBH_4$ is added drop wise to the resin. Nickel ions are reduced to metallic nickel particles by the following reaction

$$2Ni^{2+}+4BH^{4-}+9H_2O \rightarrow Ni_2B +12H_2+3B(OH)_3$$
$$4Ni_2B+3O_2 \rightarrow 8Ni+2B_2O_3$$
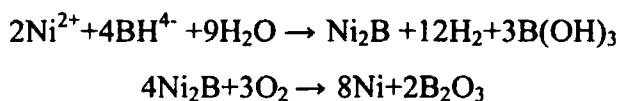
The resins are then washed several times with distilled water to remove the by-products of the reaction. Thus nanosized Ni particles are expected to be trapped within the interstitial channels of polymer beads. The schematic of the synthesis is depicted in figure 6.3. A similar procedure using WAC was adopted for the incorporation of nano nickel inside the matrix except that SO^{3-} H^+ is replaced by COO-H^+ in WAC. The metal–loading reduction cycle can be repeated to increase the metal content in the composites. Hence an increased loading is achieved by cycling the samples. The samples are cycled several times and are labeled as SAC-Ni2 to SAC-Ni6 and WAC-Ni2 to WAC-Ni10. The physical appearance of the pure ion exchange resin and that of SAC nickel composites are depicted in figure 6.4 (a) and (b).
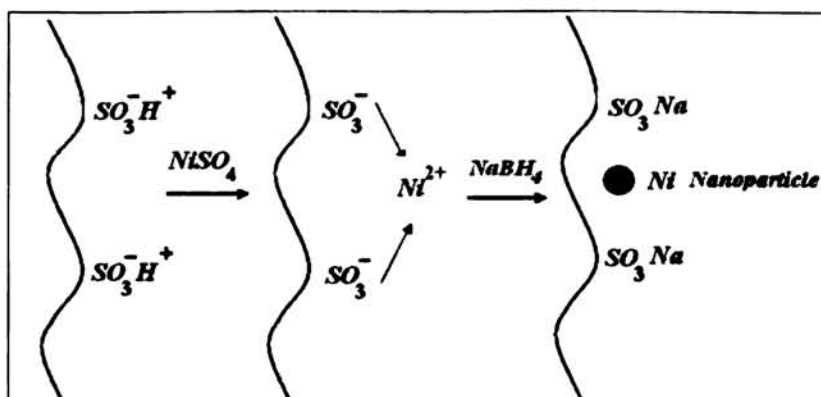
Figure 6.3 Schematic of synthesis of Nickel-polystyrene nanocomposites

(a)   **(b)**

Figure 6.4 Photographs of (a) Polystyrene beads (SAC) (b) SAC-Ni nanocomposites

The same approach was adopted for the synthesis of Iron –Polystyrene nanocomposites. In this case the nanoparticles were prepared using sodium borohydride as the key reductant. $NaBH_4$ (3M) is added to $FeCl_3.6H_2O$ (4M) in the 1:1 volume ratio. Ferric iron nanoparticles were precipitated according to the following reaction.

$$4Fe^{3+}+3BH_4^-+9H_2O \rightarrow 4Fe^0\downarrow+3H_2BO_3^-+6H_2+12H^+$$
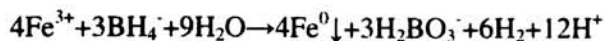
The reaction was carried out in these two templates namely SAC and WAC and cycling was conducted. The samples are labeled SAC-Fe2 to SAC-Fe12 and WAC-Fe2 toWAC-Fe10.

159

6.2. Nickel- Polymer Nanocomposites

6.2.1 Structural Properties

The X-ray diffraction patterns of the SAC-Ni and WAC-Ni nanocomposites are shown in figure 6.5 and figure 6.6. The patterns are characteristic of an fcc lattice consisting of nickel nanoparticles without any detectable traces of any impurity. No peaks corresponding to nickel oxide were observed in the case of samples on SAC-Ni. However in the case of samples on WAC-Ni, the XRD pattern consists of characteristic peaks of nickel and nickel oxide. The appearance of a kink in the main peak at 44 ^{0} indicates the presence two phases, one that of nickel ($44.5°$ – (111)) and the other corresponding to nickel oxide ($43.3°$ – (200) plane) in the composite. The two peaks almost overlap and hence the difficulty in distinguishing one from the other. Due to the macroporous nature of WAC, compared to the gel type nature of SAC, the chances of formation of oxide is more in the case of WAC-Ni than SAC-Ni.
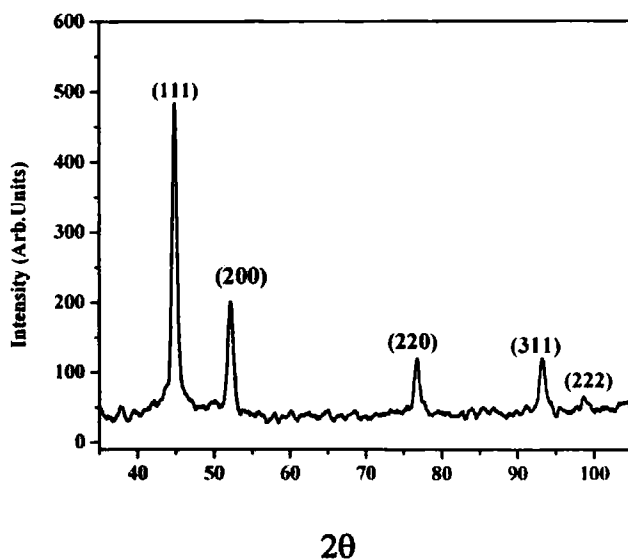

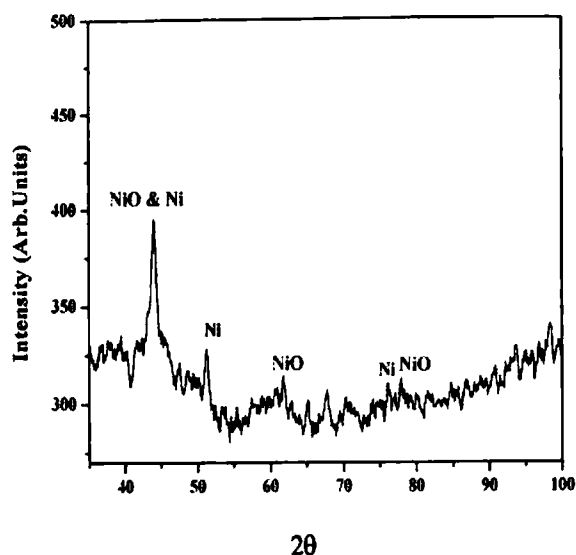Figure 6.5 XRD pattern of Nickel Polymer composite SAC-Ni16

Figure 6.6 XRD pattern of Nickel Polymer composite WAC-Ni10

In SAC-Ni16 the particle size was found to be ~13 nm. The lattice parameter values are found to be 3.522 Å for SAC-Ni and 3.561 Å for WAC-Ni. The lattice parameter of bulk nickel is 3.523 Å (ICDD No. 04-1027) and of nickel oxide is 4.117 Å (ICDD No. 02-7440). The expansion of the lattice in WAC-Ni can be attributed to the interfacial stress that originates from the lattice mismatch between nickel and nickel oxide [20, 21].

The effect of cycling on the structural parameters of nickel composites is depicted in figure 6.7 and figure 6.8. The XRD of these samples indicates that the formation of crystalline nickel particles occurs after two cycles of reduction. With cycling, the crystallinity of the sample is found to be increasing due to the addition of more and more nickel nanoparticles after each metal loading – reduction cycle. The variation in intensity of the peaks reveals the increased number of crystalline particles in the matrix. The average particle size for all the cycled (from SAC-Ni4 to SAC-Ni16) samples was found to be around 13 nm.
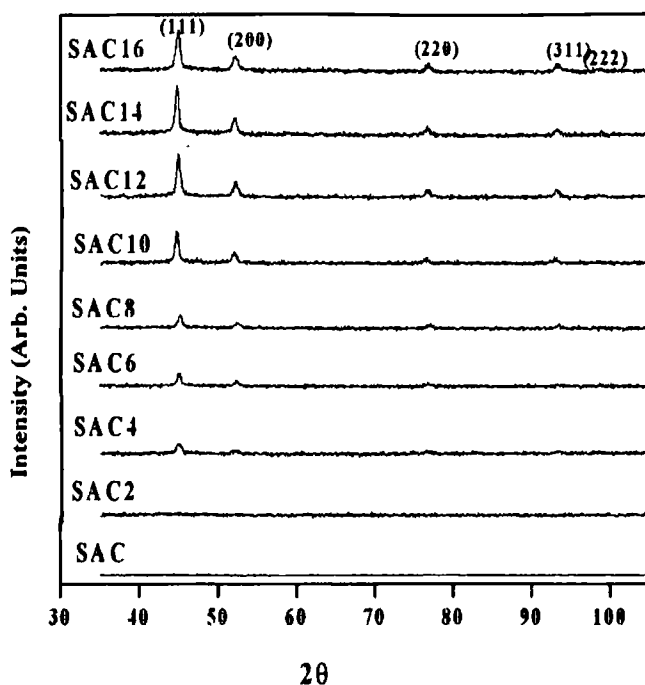
Figure 6.7 XRD patterns of the composites from SAC to SAC-Ni16

Although there is an increase in the crystalline behaviour of the composites (SAC-Ni), the particle size of the nanoparticles incorporated in the matrix do not undergo any change with cycling. Hence it is to be presumed that the nickel nanoparticles are trapped in the polymer matrix as soon as they are formed and further growth of nanoparticles is inhibited. After each cycle, it is the concentration of nickel nanoparticles in the matrix which is increasing. The improved crystallinity of the composites is manifested in the XRD pattern. The absence of any oxide phase in all the cycled samples of SAC confirms the formation of self protected metal nanoparticles. On the other hand the presence of nickel oxide in WAC-Ni composites points towards the existence of nickel oxide layer on the nickel particles.
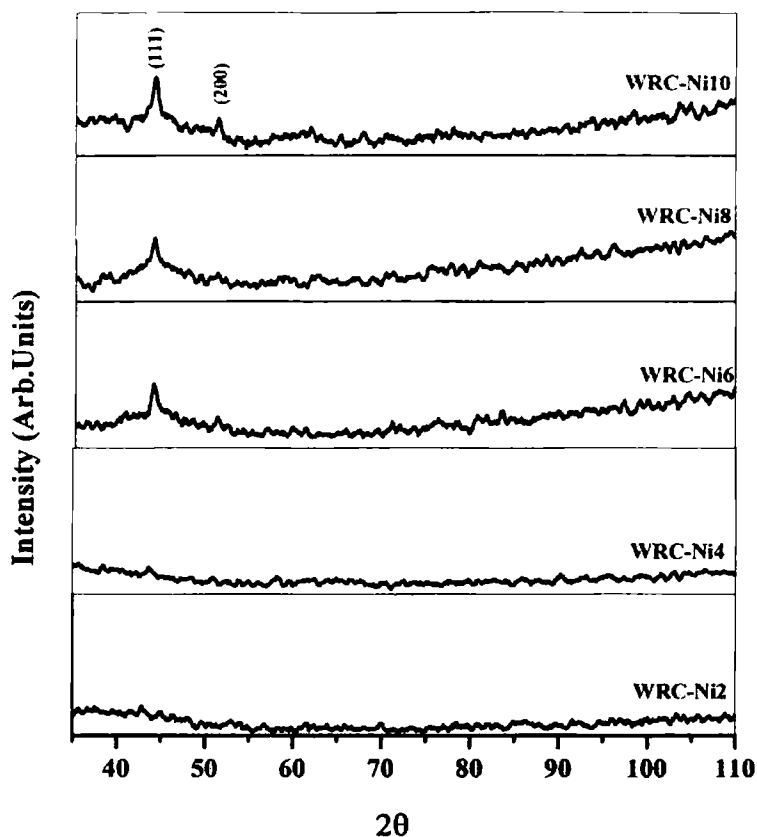
Figure 6.8 XRD patterns of the composites from WAC-Ni2 to WAC-Ni10 (WRC-Ni)

From ICP measurements the nickel content in the composite is estimated and the percentage of nickel in the composite is found to be increasing with cycling and is shown in figure 6.9. For SAC-Ni16, a maximum loading of 21% is obtained which is consistent with our earlier studies on polystyrene nanocomposites [18]. For the maximum cycled WAC resin 16% of nickel by weight was obtained.
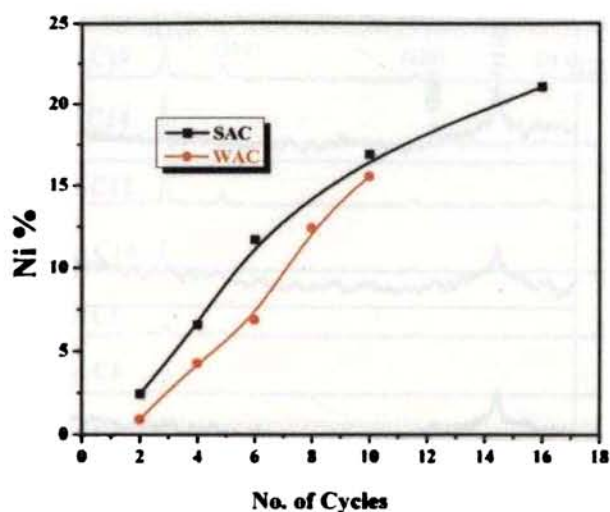
Figure 6.9 ICP Analysis of SAC-Ni and WAC-Ni composites

The scanning electron micrographs of SAC-Ni12 and WAC-Ni8 are shown in figure 6.10(a) and (b). The dense channeled structure of SAC is quite evident from the micrograph while the porous character of WAC is apparent from the images. Some of the anchored nickel particles in the channels can be noticed in SAC-Ni12.

(a)   (b)

Figure 6.10 SEM image (a) SAC-Ni12 and (b) WAC-Ni 8

Representative TEM micrographs of ball milled samples are shown in figure 6.11(a) and (b). The particle size is estimated to be 19nm for the Nickel in SAC (Ni) composite. Discrete pores of the WAC resins with sizes in the range 60-70nm along with embedded nickel nanoparticles are clearly seen in the TEM. But the nanoparticles are found to have larger size (around 40nm) in the weak resin. This may be due to the agglomeration of the nanoparticles within the pore.

(a)   (b)

Figure 6.11 TEM images of (a) SAC-Ni6 (b) WAC-Ni8

(a)   (b)

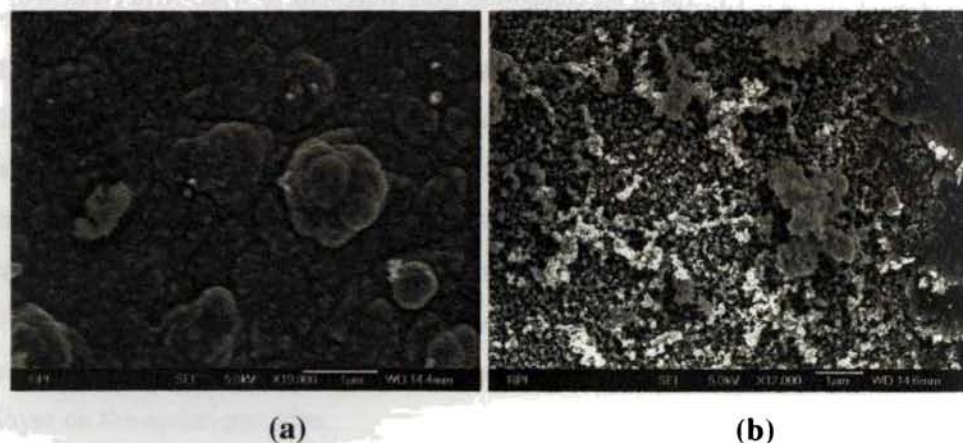**Figure 6.12** EDS pattern of (a) SAC-Ni16 and   12(b) WAC-Ni8

EDS patterns of the composites confirm the presence of nickel in the polystyrene matrix. (Figure 6.12(a-b))

6.2.2 Magnetic Properties

Room temperature hysteresis curve of the two set of composites are shown in figure 6.13 and figure 6.14. The hysteresis curves of SAC-Ni composites are typical of ferromagnetic nanoparticles. The nature of the M-H curve in WAC-Ni is indicative of the presence of an antiferromagnetic component. The antiferromagnetic nature of the nickel oxide layer in the WAC composite may be contributing to this feature .So the WAC-Ni composites may contain nickel-nickel oxide core –shell nanostructures. An exchange bias coupling can occur between the two phases [22]. The non saturating nature of magnetization curves of WAC-Ni composites supports this argument.
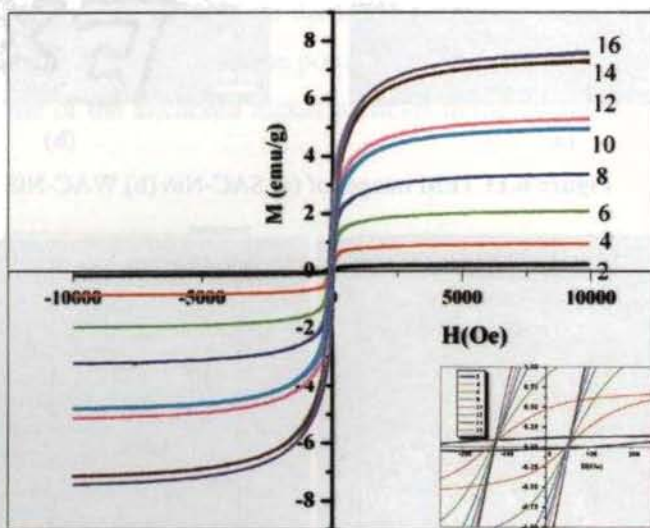

Figure 6.13 Room temperature Magnetization curves for SAC-Ni nanocomposites
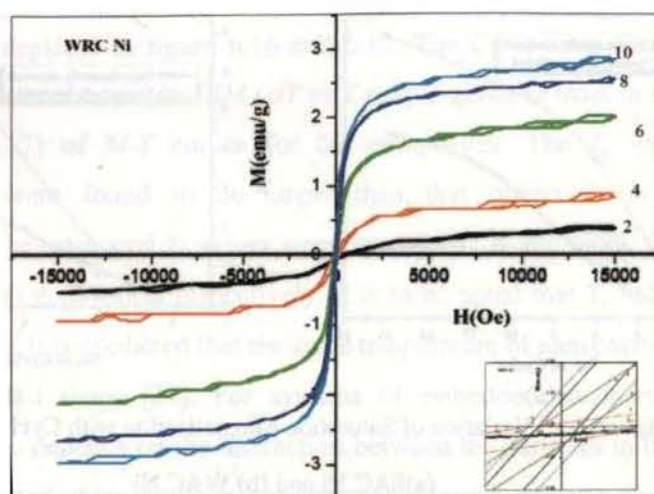
Figure 6.14 Room temperature Magnetization curves for WAC Ni nanocomposites

In both the composites, the cycling enhances the magnetization values. The magnetization value of the composite is entirely due to the magnetic nickel nanoparticles in the matrix and is shown in figure 6.15(a, b). The expected value of M_s is estimated from the bulk M_s values [55emu/g] and percentage of Nickel content as estimated from ICP analysis. The observed Ms values of the nanoparticles of these composites are lower than that of the theoretically expected values. The decrease in Ms might be due to the decrease in particle size and the accompanied increase in surface area. The presence of nickel oxide along with nickel also could be a contributing factor [20]. Reduction in M_s in nickel nanoparticles may be due to the presence of amorphous nickel and the non magnetic or weakly magnetic interfaces [23].
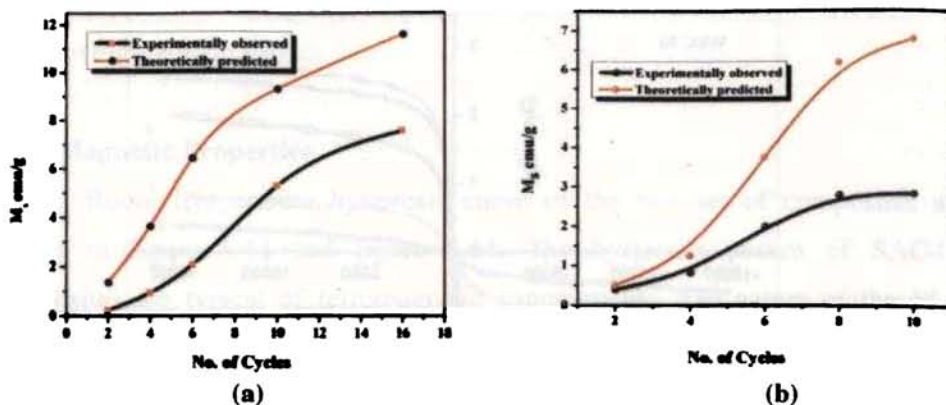
Figure 6.15 Variation of Saturation Magnetization with Cycling in

(a)SAC Ni and (b) WAC Ni

These composites exhibit saturation tendencies even after the second cycle. This reaffirms the formation of pure elemental nickel at the 2nd cycling itself. With cycling, the saturation magnetization increases. It is the increase in metal loading after each cycling that result in the increased M_s values. The increase in M_s is found to be slow at higher cycles in both the composites. The coercivity values of the composites are found to be around 100 Oe (table 6.1). The coercivity values show a little variation after the second cycle in SAC-Ni composites while a clear variation is observed in WAC-Ni composite (inset of figure 6.13 and 6.14). Accordingly the formation of self protected elementary nanoparticles of nickel can be assured in the samples on SAC-Ni .In the case of WAC-Ni composites the formation of an oxide layer over the nanoparticles is expected.

	Ms emu/g (300K)	Ms emu/g (100K)	H_c Oe (300K)	H_c Oe (100K)	Tc K
SAC Ni-16	7.6	10	80	120	707
WAC Ni-8	2.06	3.03	35	90	689

Table 6.1 Comparison of Magnetic parameters in SAC-Ni and WAC-Ni

The temperature dependence of magnetization (*M* vs. *T*) for the two composites is depicted in figure 6.16 and 6.17. The Curie temperature (T_c) was estimated by derivative graphs (dM / dT vs *T* graph -given as inset in figure (6.16) and figure (6.17) of *M-T* curves for the composites. The T_c values of the nanoparticles were found to be larger than that observed for their bulk counterparts. The estimated T_c values were around 707 K and 689K for the SAC-Ni and WAC-Ni composites respectively. It is to be noted that T_c values for bulk Nickel is 631 K. It is predicted that the curie temperature of nanoparticles depends on both size and shape [24]. For systems of embedded nanoparticles, Curie temperature also depends on the interaction between the particles in the matrix. It has been reported that there exists different degrees of spin-pin interaction between inner and surface atoms in the nanoparticles [25,26].These interaction could contribute to the enhancement of T_c in nanocomposites. The magnetic transition in the WAC-Ni composites around 560K points towards the antiferromagnetic transition of nickel oxide [27]. Accordingly the SAC-Ni metal composites were found to have superior magnetic characteristics compared to the WAC-Ni composites.
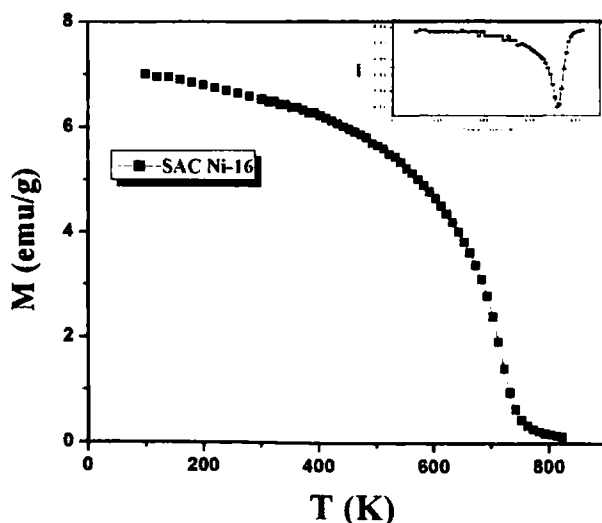

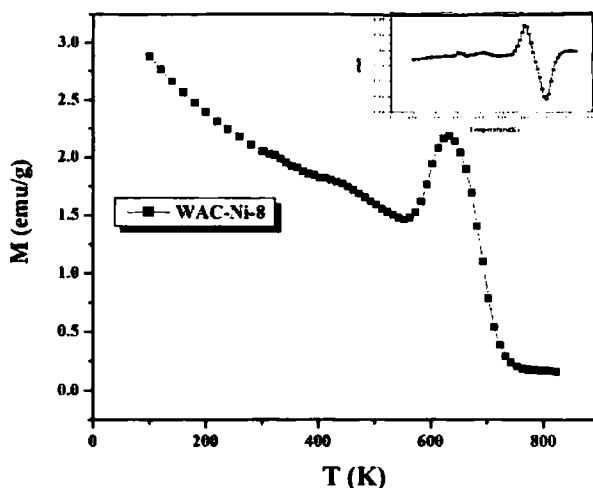**Figure 6.16** M-T curve for SAC-Ni16 (Inset dM/dT vs *T* curve)

Figure 6.17 M-T curve for WAC-Ni10 (Inset $\frac{dM}{dT}$ vs T curve)

Iron-polystyrene composites are also prepared. Now we discuss the synthesis and properties of iron-polystyrene nanocomposites in the ensuing section.

6.3 Iron Polystyrene Nanocomposites

Two types of iron-polystyrene nanocomposites were prepared by the method of ion exchange as described in the synthesis section 6.1. The loading reduction cycle was repeated and the samples are labeled as SAC-Fe2 to SAC-Fe12 and WAC-Fe2 to WAC-Fe10.

6.3.1 Structural Analysis

The XRD patterns of SAC-Fe and WAC-Fe samples were taken. But even for the maximum cycled samples (SAC-Fe12) and WAC-Fe10 no peaks corresponding to α-Fe was obtained in the X-ray diffraction pattern for SAC sample containing Iron. The presence of amorphous phase of iron [28] together with the polystyrene coating may be the reasons for the absence of XRD peaks. The XRD pattern of the powdered samples were recorded and attempt to figure

out any diffraction peaks corresponding to iron were in vain. However, some peaks corresponding to the oxide phase of iron was found in WAC-Fe10. This oxide formation may be due to the macroporous nature of the WAC resin as observed in the case of Nickel composites. The XRD pattern is shown in figure 6.18.
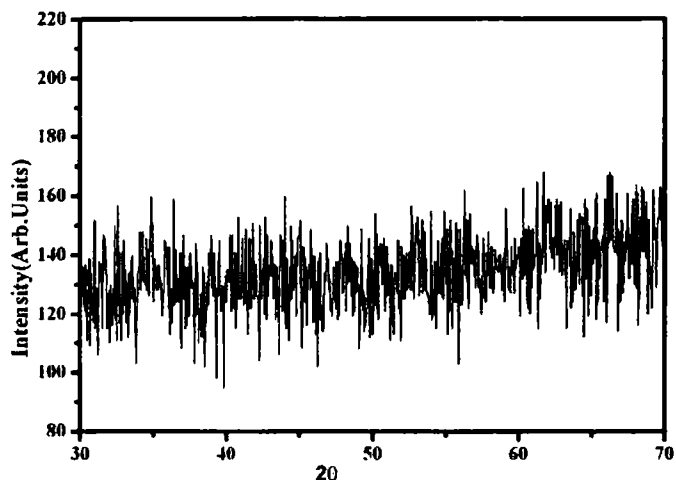

Figure 6.18 XRD pattern of Iron incorporated in WAC-Fe8

The absence of any clear peak corresponding to α-Fe in the X-ray diffraction pattern prompted us to reproduce the experiment of reduction using NaBH$_4$ and employing oleic acid as a surfactant. The synthesis procedure was carried out in the absence of the matrix so as to ensure the formation of iron nanoparticles by the reduction process outside the matrix and under ambient condition. But it was found that the particles immediately transformed to the nonmagnetic oxide of iron as soon as they were exposed to air. Hence a coating was necessary. The iron particles were then coated with oleic acid immediately after precipitation. On heating these samples at 200°C exhibited clear diffraction pattern and are shown in figure 6.19. It can be noticed that this method of ion-exchange reduction has resulted in α-Fe like the reduction procedure carried out within the matrix.
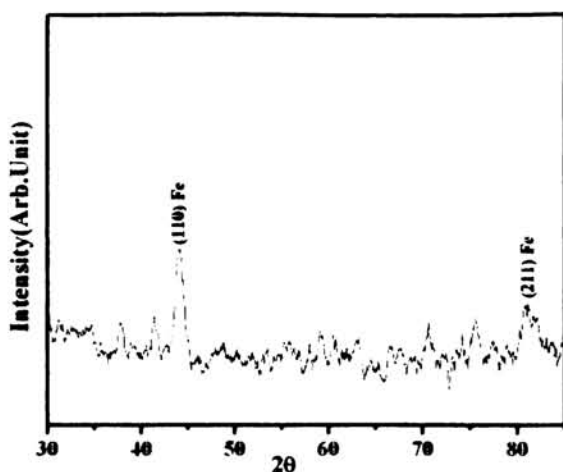
Figure 6.19 XRD pattern of oleic acid coated iron nanoparticles

The particle size and lattice parameters of the sample was found to be 17.14 nm and 2.907Å (2.886 Å for bulk iron) respectively. Electron diffraction and X-Ray diffraction of these samples confirmed the presence of pure elemental Iron (Figure 6.20(a-b)). The particle size was found to be 30nm which is not consistent with the XRD measurements.
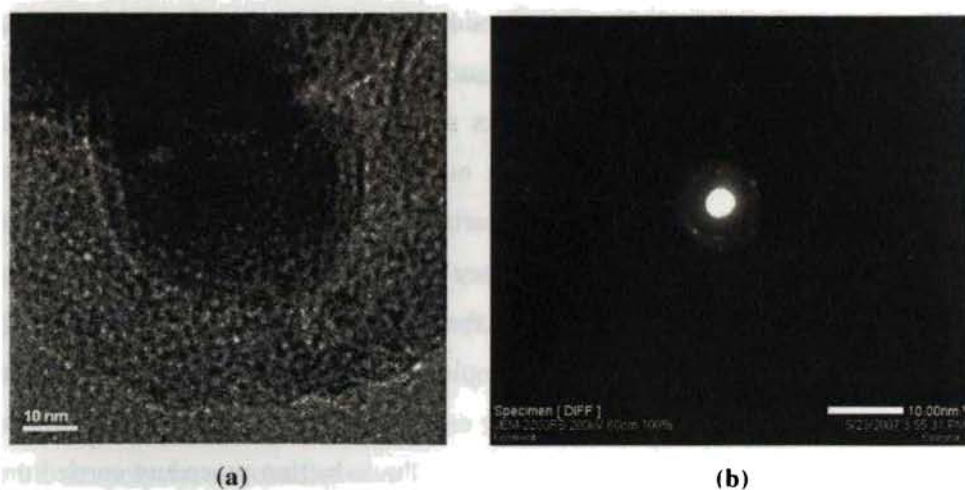
Figure 6.20 (a) TEM image and (b) Diffraction patterns of oleic acid coated Fe nanoparticles

The SEM pictures of the SAC composites are given in the figure 6.21 (a-b). Some of the anchored iron nanoparticles are seen on the surface of the resins.

(a)   (b)
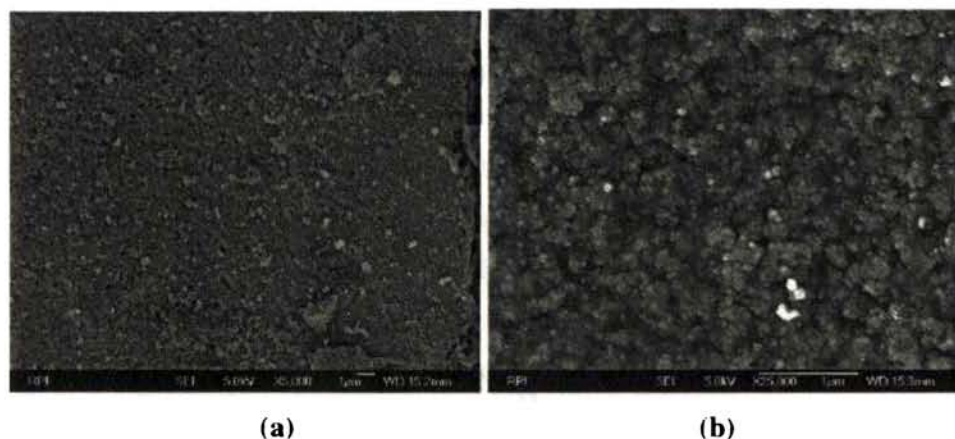
Figure 6.21 SEM images of (a) SAC-Fe 8 and (b) WAC- Fe 8

The iron content estimation was done by ICP measurements. The Fe content in the oleic acid coated sample was found to be 25.86%. The iron content in the composite was found to be increasing with cycling. The variation of iron content with cycling in SAC-Fe and WAC-Fe is depicted in figure 6.22.
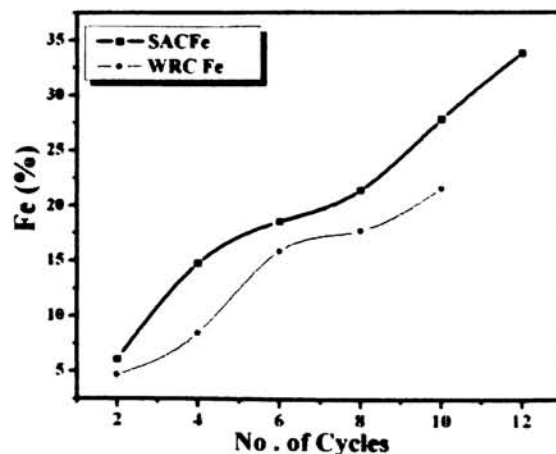
Figure 6.22 ICP analysis of Iron content in the SAC-Fe and WAC-Fe (WRC) composites

6.3.2. Magnetic Properties

The hysteresis loop for the oleic acid coated iron nanoparticles is depicted in figure 6.23.

Figure 6.23 Hysteresis loop for the oleic acid coated iron nanoparticles

The hysteresis curves of the SAC-Fe nanocomposites are given in figure (6.24).
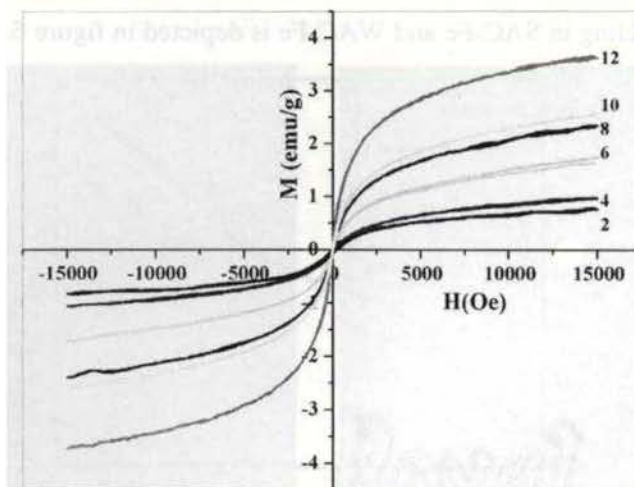
Figure 6.24 Hysteresis loops for the SAC-Fe nanocomposites

The saturation magnetization was found to be 29.8 emu/g. The effective magnetization of the iron nanoparticles can be estimated to be 112.3emu/g .This information also confirm the presence of formation of iron nanoparticles. The lower 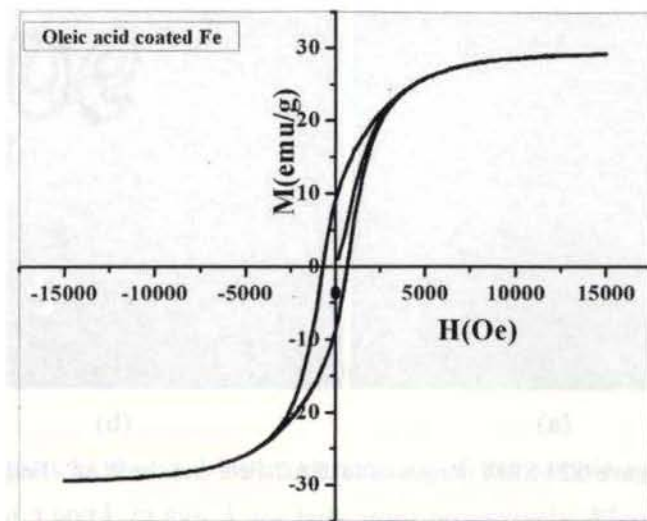magnetization of the nanoparticles can be attributed to an increase in the surface anisotropy induced by chemisorption of oleic acid [29].

It can be found that the magnetization do not saturate even at a field of 15kOe.The non saturating nature of magnetization may be due to the amorphous nature of iron. The hysteresis curves at 300K and 100 K are compared and shown in figure (6.25). The coercivity is found to be very low or the particles are exhibiting nearly a superparamagnetic nature.
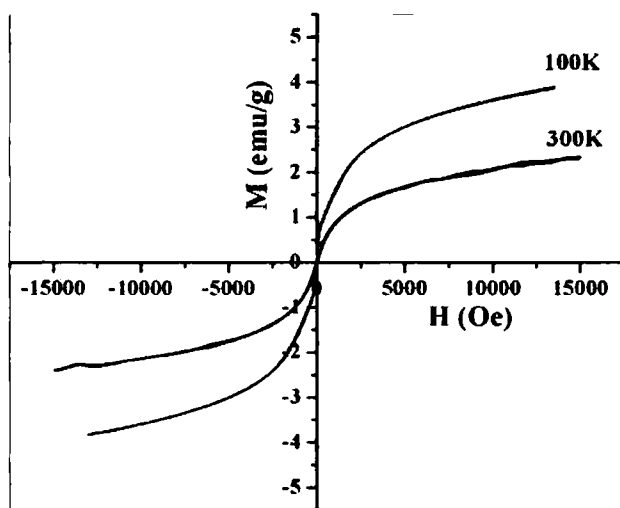
Figure 6.25 Hysteresis curve of the SAC-Fe composite at 300K and 100K

For the samples that did not saturate at the highest applied field, the saturation magnetization was calculated by extrapolating the M vs. 1/H curve for $\frac{1}{H} \to 0$. The maximum magnetization of nickel nanoparticles contained in the composite is estimated to be 10.66 emu/g. The saturation in a nanoparticle system

is generally lower than that of the bulk material and is strongly influenced by the supporting matrix. A possible feature in nanocomposite material is the difference in spin ordering at the surface of particle over that in the bulk, setting up a magnetic core shell configuration. There is also a chance of formation of oxide layer of iron oxide (FeO or α-Fe$_2$O$_3$ or γ-Fe$_2$O$_3$) over the iron nanoparticles as the reactivity of iron nanoparticles are very high. FeO and α-Fe$_2$O$_3$ are antiferromagnetic while γ-Fe$_2$O$_3$ and Fe$_3$O$_4$ are ferromagnetic. Also the presence of unstable phase of iron [30] with a paramagnetic nature can contribute to this feature. However the behaviour of the hysteresis curve showed the presence of an antiferromagnetic component. An increase in coercivity associated with exchange coupling of antiferromagnetic - ferromagnetic (AFM-FM) layers is found to be absent here. Surface spin disorder, spin canting or asperomagnetic nature of amorphous iron (as a random collinear spin structure with non-zero net moment) may also reduce the magnetisation [31,32]. Further investigations are needed to determine the exact role of the interparticle interaction in the polymer matrix in deciding the magnetic properties of the composites.
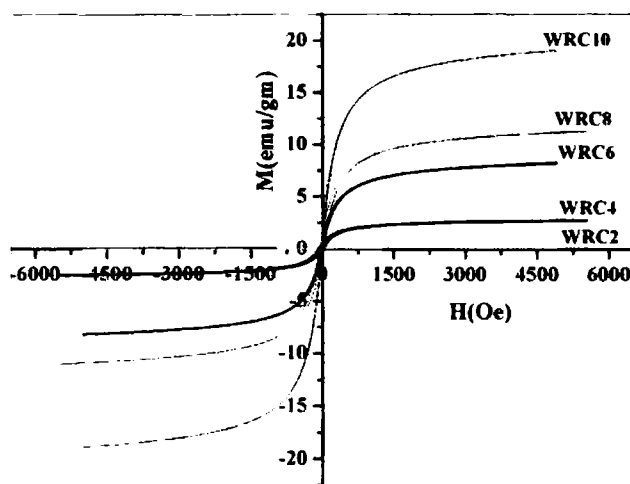

Figure 6.26 Hysteresis curves of the WAC-Fe (WRC) composites

The magnetisation curves of WAC-Fe composites (figure 6.26) were found to be quite interesting when compared to the SAC composites. All the M-H curves showed saturation with fairly high magnetization values. These observations were contradicting the results obtained in SAC-Ni and WAC-Ni nanocomposites. In the case of composite containing nickel (WAC-Ni composite) it was found to be antiferromagnetic and exhibited reduced magnetization. Probably this may be due to the presence of Nickel oxide in detectable amounts. The micro porous nature of WAC-Fe was found to be prone to easy oxidation and agglomeration of nanoparticles in discrete pores were also expected. The presence of a ferrimagnetic spinel oxide layer on the ferromagnetic iron core may have resulted in strong interaction between the core and shell which is evident as increased magnetisation values of WAC-Fe compared with the SAC-Fe composites.

6.4 Conclusion

Nickel–polystyrene and iron-polystyrene nanocomposites are synthesized by the intermatrix ion exchange synthesis where we have used strongly acidic cationic exchange resin (SAC) and weakly acidic cationic exchange resin (WAC) with cationic exchange sites as the parent matrices. The sequential loading of the cationic exchange sites with metal ions and their subsequent reduction using Sodium borohydride resulted in Ni/Fe-polystyrene nanocomposites. The crystallainty and magnetic characteristics are modified by repeating the loading-reduction cycle. The effect of cycling on the structural and magnetic properties of the composites is also investigated. The XRD patterns of the cycled samples confirmed that the there is no particle growth with cycling. These investigations indicate that SAC-Ni composite contain phase pure nickel nanoparticle trapped in the interstitial channels of the polystyrene matrix and their further growth is inhibited. On the other hand, WAC-Ni composites contain two distinct phases of nickel and nickel oxide. Comparison of the structural and magnetic properties of

the two types of composites showed that the SAC-Ni composite is better suited structurally and magnetically for applications when compared to nickel composites of WAC.

In the case of polystyrene beads embedded with Fe nanoparticles, the Fe nanoparticles are found to possess an amorphous nature. However presence of magnetic iron oxide was identified in the WAC-Fe nanocomposites. SAC-Fe nanocomposites exhibit hysteresis curves with lower magnetization and with a non saturating behaviour while higher magnetization and saturation was observed in the case of WAC-Fe nanocomposites. The enhancement of magnetization in WAC-Fe can be attributed to the formation of oxide phase of the metal nanoparticles in the porous matrix as observed in the case of WAC-Ni composites. The oxide formed is magnetic in nature resulting in higher magnetization. Strongly acidic cation exchange resin is the appropriate template for the preparation of passivated metal nanoparticle. These interesting attributes of the magnetic nanocomposites can be tailored for promising applications. Moreover optical and electrical characterization of these composites can be promising areas of research for device applications.

References

1. Gleiter, H. Progress in Materials Science, 33, (1990), 223.

2. Klabunde. K. J; C. Mohs. *Chemistry of Advanced Materials: an Overview*, Interrante. L. V; Hampden-Smith. M. J; Wiley-VCH. New York, (1998), 271.

3. Miller. M.M; Prinz.G.A; Cheng. S.F; Bounnak. S. Appl. Phys. Lett. 81, (2002), 2211.

4. Torok. G; Lebedev. V. T; Cser. L; Kali. G; Zrinyi. M; Phys. B 40 (2001), 297,.

5. Yu Lu; Xianmao Lu; Brian Mayers. T; Thurston Herricks; Younan Xia.; J Solid State Chem. 181, (2008), 1530.

6. Don Keun Lee; Young Hwan Kim; Xiao-Li Zhang. ; Young Soo Kang. Current Appl. Phys. 6, (2006), 786.

7. Pomogailo. A.D; Dzhardimalieva. G.I; Rozenberg. A.S; Muraviev. D. J Nanopart Res. 5, (2003), 497.

8. Santini.O; Mosca. D.H; Schreiner. W.H; Marangoni. R.; Guimaraes. J.L; Wypych. F; A.J.A. Oliveira . J. Phys. D: Appl. Phys.36,(2002), 428.

9. Leite. E.R; Carreño. N.L.V; Longo. E; Valentini. A; Probst. L.F.D. Journal of Nanoscience and Nanotechnology 2, (2002), 89.

10. Huang. Z.P. ; Wang. D.Z. ; Wen. J.G. ; Sennett. M. ; Gibson. H; Ren. Z.F. Applied Physics A 74, (2002), 387.

11. Levy. L; Sahoo. Y; Kim. K. S; Bergey. E; Prasad. P. N; *Chem.* Mater.14, (2002) 3715.

12. Ziolo. R.F; Giannelis. E.P; Weinstein. B.A; O'Horo. M.P; Ganguly.B.N; Mehrotra. V; Russell. M.W; Huffman. D.R; Science 257, (1992), , 219.

13. Shull.R.D; Bennett. L.H; Nanostruct. Mater., 1,(1992), 83.

14. Kickelbick. G. Progress in Polymer Science, 28, (2003), 83.

15. Muraviev.D.N. Chem. Scripta. 29,(1989), 9.

16. Mu.Li Wang; Chun Hong Wang; Wei Wang; Material Chemistry and Physics. 104, (2007), 162.

17. Malini K.A; Anantharaman. M.R; Sindhu. S; Chinnasamy. C.N.; Ponpandian. N; Narayanasamy. A; Balachandran. B; Shivasankarapillai. V.N. Journal of Material Science 36, (2001), 821.

18. Swapna Nair S; Mercy Mathews; Joy, P.A; Kulkarni. S.D; Anantharaman.M.R; J. Magn. Magn. Mater. 283, (2004), 344.

19. http://www.sigmaaldrich.com/aldrich/brochure/al_pp_ionx.pdf

20. Rellinghaus. B; Stappert, S; Wassermann. E. F; Sauer. H; Spliethoff. B. Eur. Phys. J. D,16, (2001), 249.

21. Hofmeister. H; Huisken. F; Kohn. B. Eur. Phys. J. D. 9,(1999), 137.

22. Seto.T; Akinaga. H; Takano. F; Koga. K; Orii.T; Hirasawa. M. J. Phys. Chem. B. 109, (2005), 13403.

23. Turek. I. ; Hafner; J; Phys.Rev.B: 46, (1992), 247.

24. Evans.R; Nowak.U; Dorfbauer. F; Shrefl. T; Mryasov. O; Chantrell. R. W; Grochola. G. J. Appl. Phys. 99, (2006), 08G703.

25. Cole. D. H; Shull. K. R; Rehi. L. E;Saucer. Baldo; P. Phys.Rev Lett. 78, (1997), 5006

26. Lang, X. Y; Zhang, W. T;Jiang, Q. Phys.Review B , 73, (2006), 2244.

27. Magnetic oxides, Part1, Craik. D .J. ; John Wiley & Sons, (1997).

28. Mark W Grinstaff,Myron B Salamon,Kenneth S Suslik, Phys.Rev.B 48 (1993) 269

29. Ling Zhang,Rong He,Hong Chen Gu,Applied Surface Science 253 (2006) 2611

30. I Turek , J Hafner, Phys.Rev.B, 46,(1992), 247

31. Kataby G,Cojoearu M,Prozorov R,Gedanken A,Langmuir 15, (1999),1703

32. M Leibs,K Hammler,M Fahnle, Phys.Rev.B,51, (1995), 8664

Chapter 7

Magnetocaloric Effect in Cobalt Ferrite Nanoparticles and Nickel Nanocomposites: Estimation of Isothermal Magnetic Entropy Change

Magnetocaloric effect (MCE) forms the basis for magnetic refrigeration technology. The characteristic magnetocaloric parameters, namely, isothermal magnetic entropy change, ΔS_m and adiabatic temperature change ΔT_{ad} determine the usefulness of a magnetic material as a magnetic refrigerant. Magnetocaloric properties of nanomagnetic materials of ferrites and metal nanoparticles are seldom investigated. In this chapter an attempt is made to estimate the magnetocaloric properties of cobalt ferrite nanoparticles and nickel polystyrene nanocomposites by estimating the isothermal magnetic entropy change from magnetization isotherms. It has been found that nanosized cobalt ferrite exhibits reasonable MCE values and an inverse magnetocaloric effect.

The search for eco-friendly alternatives to Chloro Fluoro Carbon (CFC) based refrigeration has been going on for over two decades. The ozone depletion is quite alarming and this has prompted new legislations the world over for curbing the usage of ozone depleting chemicals. As a result, scientists and engineers have been searching for possible alternatives. This search resulted in identifying magnetic refrigeration as a viable alternative to CFC based refrigeration [1-2]. The onus of providing alternate technologies has fallen on magnetic materials, more precisely on nanocrystalline magnetic materials. In that ferro and ferrimagnetic materials are promising candidates for these applications.

Ferrites and other metal particles when prepared in nanodimensions exhibit interesting critical phenomena like superparamagnetic and spin glass behaviour characterized by ordering temperatures, namely, T_B and T_g, the blocking temperature and glass transition temperature respectively [3-4]. Therefore nanocrystalline materials which exhibit these critical phenomena and whose T_B/T_g can be tuned are ideal materials and are promising candidates for magnetic refrigeration applications. Magnetic refrigeration is based on the principle of magnetocaloric effect (MCE), which is the heating and cooling of a magnetic material in the presence and absence of a magnetic field. Nanocrystalline ferrites and nanocomposites based on metals like nickel are thought to be potential magnetic refrigerants since they are expected to become superparamagnetic or exhibit spin glass behaviour when their size is reduced below a critical size. Cobalt ferrite in the nanoregime exhibit interesting magnetic properties so is nano nickel embedded in a matrix. This was evident from a study conducted on the properties of these materials and is already described in chapter 5 (cobalt ferrite) and chapter 6 (Ni nanocomposites).

The vital parameters that determine the performance characteristics of a magnetic refrigerant are the critical temperature at which the material transforms from ferromagnet to paramagnet (T_c) or ferromagnet to superparamagnet (T_B) or ferromagnet to spin glass (T_g). Since this is the operating temperature of the

refrigerator where one expects maximum entropy change, this is a crucial parameter as far as applications are concerned. Also the prerequisite of a good refrigerant is that the applied magnetic field at which the entropy change is maximum should be as low as possible. Normally applied magnetic field has to be moderate since the magnetic refrigerator should work under normal applied field. For room temperature magnetic refrigeration the ordering temperature of the magnetic refrigerant should be around 293K.

Having investigated the magnetic properties of nanosized cobalt ferrites and nickel nanocomposites it was thought that the MCE properties of these materials would be interesting. This was carried out with a view to finding out the potential of these materials as magnetic refrigerants. The magnetic entropy change ΔS_m was estimated indirectly from magnetization isotherms of the magnetic nanoparticles.

7.1 Estimation of ΔS_m in $CoFe_2O_4$ Nanoparticles

Cobalt ferrite, because of its large magnetocrystalline anisotropy, is expected to exhibit nonzero coercivity even at very small particle sizes of the order of 5nm and is a promising candidate for many applications [5-6]. Decreased particle size leads to decreased H_c and T_c but an increased anisotropy at the nanodimensions results in increased T_B in cobalt ferrite nanoparticles. Hence the blocking temperature T_B of cobalt ferrite nanoparticles can be suitably tuned to room temperature by exploiting the anisotropy factor. Since blocking temperature corresponds to a magnetic transition, one can expect enhanced entropy change around this ordering temperature. Also the field required for enhanced magnetic entropy change in the case of nanoparticles is relatively small. This would increase the efficiency of the refrigerator as well as reduce its size due to the reduction in cooling requirements. Thus nanosized cobalt ferrite is of interest as far as its magnetocaloric properties are concerned. The ability to tailor the ordering temperature by tuning the size of the crystallite is an added advantage as

far as the choice of the operating temperature of the refrigeration system is concerned.

Nanoparticles of cobalt ferrite were synthesized using sol-gel combustion technique. The synthesis procedure and complete characterisation of the pristine sample is described in chapter 5. Magnetization values of the samples were found to be lower than that of its bulk counterpart. However a decrease in magnetization is found at 100K and is unusual. This may be due to some magnetic phase transition occurring at this temperature region. A detailed picture can be elucidated from the thermomagnetisation curves of the different samples.
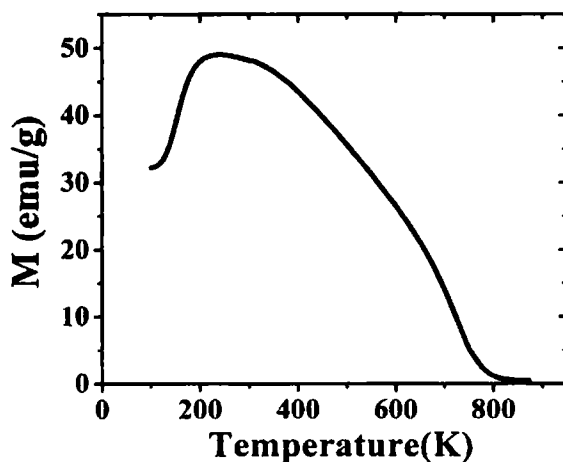
Figure 7.1 M-T Curve at 10kOe

For the estimation of the temperature range at which maximum cooling is produced, the M-T curve of cobalt ferrite at 10kOe is recorded and is shown in figure 7.1. A broad transition at around 150-350K is clearly visible from the figure. This transition assumes significance since a magnetic transition is always associated with a change in magnetization with temperature. Further the M-H curves (figure7.2) for cobalt ferrite nanoparticles over a magnetic field range of 0-13kOe at 10K temperature intervals from 173K to 323 K were measured.

The indirect technique of measuring MCE from magnetization data involves the numerical integration given of equation 2.23. If the magnetization as a function of field at various temperatures, then ΔS_m can be approximated as follows

$$\Delta S_m = \frac{1}{\Delta T}\left[\int_0^H M(T+\Delta T,H)dH - \int_0^H M(T,H)dH\right] \quad (7.1)$$

Thus the area encompassed by the two magnetization curves at two temperatures was divided by the temperature difference ΔT gives the magnetic entropy change ΔS_m at the average temperature [7].
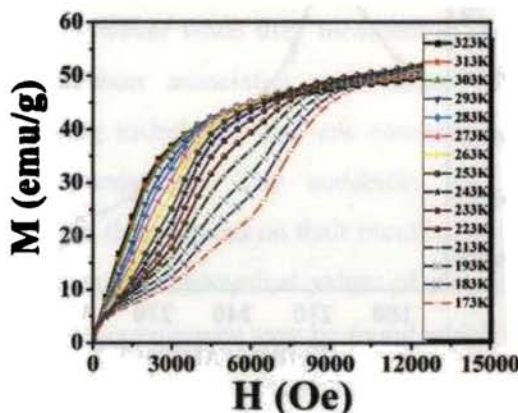
Figure 7. 2 Isothermal magnetization curves of cobalt ferrite nanoparticles

7.2 Inverse MCE in Cobalt ferrite Nanoparticles

The MCE characteristic value (ΔS_m,), the magnetic entropy change, was estimated from the M-H curves by employing the equation 7.1. Normally we observe an increase in magnetization with decrease in temperature and expect a negative entropy change and accordingly termed as characteristic MCE. However in this case, since there is a decrease in magnetization associated with the transition at this temperature range, the magnetic entropy change was found to be positive. Hence this can be termed as an inverse MCE. There are reports where in giant inverse MCE has been reported in alloys like NiMnSb Heusler alloys [8].

Usually positive entropy change is associated with antiferromagnetic transition. Hence a contribution from antiferromagnetic components like CoO and α-Fe$_2$O$_3$ cannot be ruled out here in the case of cobalt ferrite which could not be detected using XRD. Positive entropy change has been recently reported in zinc ferrite nanoparticles [9]. However the occurrence of an inverse MCE in nanosized Cobalt Ferrite is presumably reported for the first time.

The variation of magnetic entropy change with temperature is shown in figure 7.3.
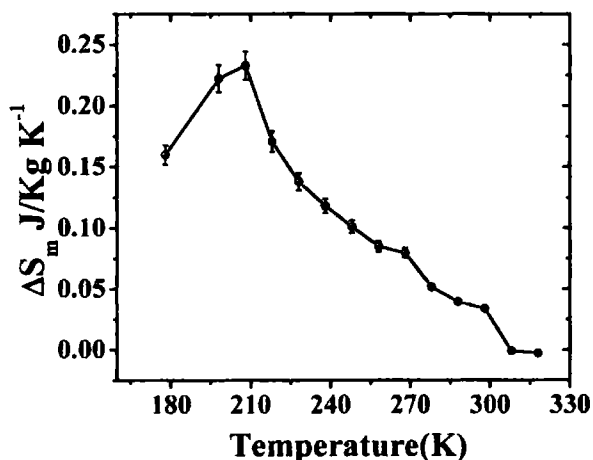
Figure 7. 3 Magnetic entropy change (ΔS$_m$) vs. Temperature in
cobalt ferrite nanoparticles

A maximum value of 0.233 J/kg K^{-1} is observed at 213K for an applied field of 13kOe. Thereafter a sharp decrease is obtained. For 5nm sized cobalt ferrite nanoparticles prepared by co-precipitation technique the maximum MCE value reported was 0.14 J/kg K^{-1} at an applied field of 35kOe [10]. Hence the magnitude of the maximum MCE value in our case is higher than that was reported for different ferrite nanoparticles like zinc ferrite, manganese zinc ferrite and nickel ferrite [9-12]. It may be noted that the ΔS$_m$ values become negative at 308K and is -0.07 mJ /kg K^{-1} which is also reasonable compared to MCE values reported in co-precipitated cobalt ferrite nanoparticles [10]. The change in the sign

of ΔS_m around room temperature may be indicative of a blocking near these temperatures for the nanoparticles. In order to delve more into this phenomenon, FC/ZFC curves were plotted and shown in figure 5.9 in chapter 5. But the blocking phenomenon which is above 300K could not be observed as it lies outside the measured temperature range. Hence a detailed study is needed for tuning the material for room temperature applications.

7.3 Estimation of ΔS_m in Nickel- Polystyrene Nanocomposites

Elemental iron, cobalt and Nickel are considered not very useful for magnetic refrigeration since in their micron regime, their curie temperatures are found to be very high. However when they incarnate in the nanoform there are various critical phenomenon associated with finite size effects and the nanocomposites containing nickel and iron are considered promising materials from a fundamental perspective. The suitability of such materials for magnetocaloric application then depend on their blocking temperature T_B or glass transition temperature T_g and the numerical values of magnetocaloric effect, that is, ΔS_m or ΔT_{ad}. Thus, a nanocomposite may be found which will allow the use of permanent magnets rather than superconducting magnets in a magnetic refrigerator since in the nano composites ΔS_m enhancement is largest at low fields [13]. This would increase the efficiency of the refrigerator as well as reduce its size due to the reduction in cooling requirements. The temperature dependence of MCE is also broader in temperature in nanocomposites than for either paramagnets or ferromagnets. This feature may be desirable in future refrigeration designs. R D Shull *et al.* reported an MCE value of 1.78 µJ / kg for a field change ΔH of 0.9T in superparamagnetic 11% Fe + silica gel nanocomposites [14].

The magnetocaloric properties of the nickel polymer nanocomposites are explored for possible applications. Nickel polystyrene nanocomposites are synthesized by a novel method of ion exchange reduction. The synthesis

techniques and the structural and magnetic properties are discussed in chapter 6. The ZFC curve for the composite is shown in the figure 7.4. It can be seen that a broad transition is found around 280K. However the change in magnetization around the temperature range is very low. This broad transition can be similar to the blocking phenomenon in nanoparticles. Since there is a magnetic transition around 280K, it may be quite interesting to delve into the magnetocaloric properties of these nanocomposites in this temperature regime.
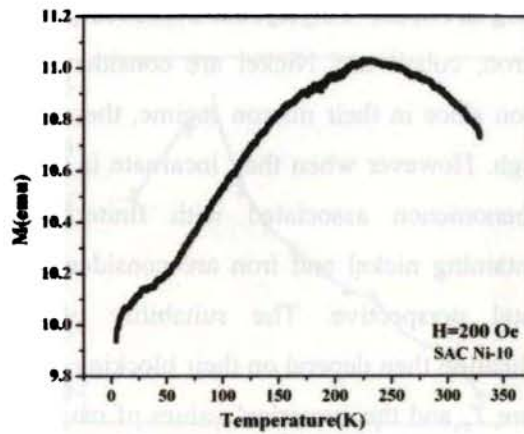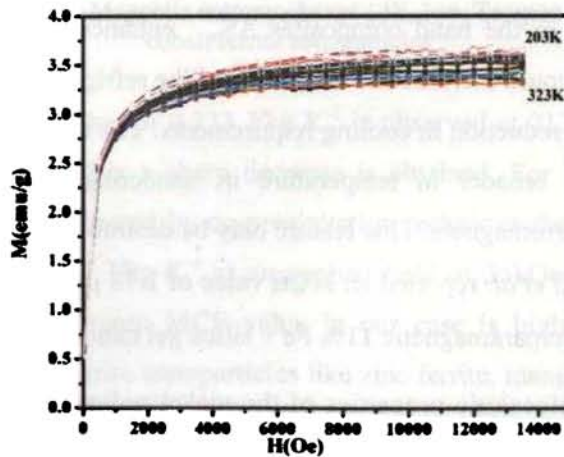

Figure 7.4 ZFC curve of SAC-Ni10

Figure 7.5 Magnetization isotherms of SAC-Ni

The isothermal magnetization data for the composites were measured between 0 and 13kOe at successively decreasing temperature between 203K and 323K at 10K intervals (figure 7.5). The isothermal magnetic entropy change can be estimated from these curves employing the equation 7.1.

7.4 MCE in Nickel-Polystyrene Nanocomposites

The variation of the estimated ΔS_m with temperature is depicted in figure 7.6. The ΔS_m value is showing a maximum value of 4.1mJ/kg K^{-1} at 288 K around which we observe a broad transition in the ZFC curve. The magnetic entropy change is found to be smaller than the MCE values estimated for cobalt ferrite nanoparticles.
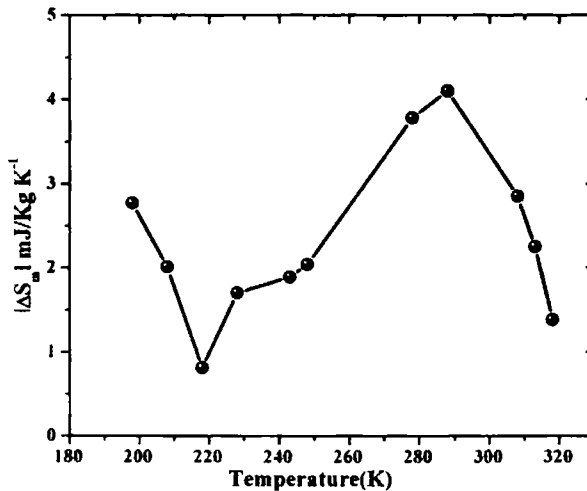
Figure 7.6 ΔS_m vs Temperature in Ni Polystyrene Nanocomposites

Although the magnitudes of the MCE values for these composites are very small, it is comparable to that estimated in other nanocomposite systems [13-14]. However the existence of MCE near to room temperature is really promising on account of the possible room temperature refrigeration applications. By properly tailoring the matrix, size of metal nanoparticles and matrix particle

interactions, the ordering temperature can be tuned. Also a peak transition instead of a broad one can yield larger MCE values.

7.5 Conclusion

The magnetocaloric properties of cobalt ferrite nanoparticles and nickel-polystyrene nanocomposites are indirectly estimated from magnetization isotherms are presented here. The maximum calculated ΔS_m corresponding to an inverse MCE and is 0.233 J/kg K^{-1} which was obtained at 213 K for an applied field of 13.5kOe. Field is relatively large when compared to the reported values. The inverse MCE values at around 308 K is suggestive of a transition at this region which can be a blocking phenomenon occurring in these nanoparticles. The observation of inverse and large MCE values in cobalt ferrite nanoparticles proclaims the potential of cobalt ferrite for cooling and heating applications. The magnetocaloric properties of nickel polystyrene nanocomposites are also really promising. The composites exhibited a maximum $-\Delta S_m$ value of 4.1mJ/kg K^{-1} at 288K. The values are comparable with those reported in other magnetic composite systems. The evaluation of the MCE properties in the system is found to be quite promising since maximum value is exhibited close to room temperature. However the values are found to be smaller when compared to the cobalt ferrite nanoparticles.

References

1. K. A. Gschneidner, Jr., V. K. Pecharsky, C. B. Zimm, *Proceedings of the 50th Annual International appliance Technical conference,* West Lafayette, Indiana, 144 (1999).

2. C. Zimm, A. Jastrab, A. Sternberg, V. Pecharsky, K. Gschneidner, M. Osborne, I. Anderson, Adv .Cryog. Eng. 43 (1998) 1759.

3. R. D. K Misra, S. Gubbala, A. Kale, W. F. Egelhoff, J. Mat. Sci. and Eng. B 111(2004) 164.

4. R. V. Upadhyay, Kinnari Parekh, R. V. Mehta, Phys. Rev. B 68 (2003) 224434.

5. F. Figueiredo, A. C. Tedesco, P. C. Morais, J. Appl. Phys. 93 (2003) 6707.

6. C. Vázquez, M. Lovelle, C. Mateo, M. A. López-Quintela, M. C. Buján-Núñez, D. Serantes, D. Baldomir, J. Rivas, Physica Status Solidi : A 205 (2008) 1358.

7. K. A. Gschneidner, V. K. Pecharsky, Mater. Sci. Eng. A 287 (2000) 301.

8. A. K. Nayak, K. G. Suresh, A. K. Nigam, J. Phys. D: Appl. Phys. 42 (2009) 035009.

9. J. Gass, H. Srikanth, N. Kislov, S. S. Srinivasan, Y. Emirov J. Appl. Phys. 103 (2008) 07B309.

10. S. Hariharan, J. Gass, *Rev.* Adv. Mater. Sci. 10 (2005) 398.

11. P. Poddar, J. Gass, D. Rebar, S. Srinath, H. Srikanth, S. A. Morrison, E. E. Carpenter, J. Mag. Mag. Mat. 307 (2006) 227.

12. J. Gass, N. A. Frey, M. B. Morales, M. J. Miner, S. Srinath, H. Srikanth, Mat. Res. Soc. Symp. Proc. 962 (2005) P05.

13. R. D. Shull, L. J. Swartzendruber, L. H. Bennet, Proceedings of the 6th International Cryocoolers Conference DTRC 91/002 Annapolis MD (1991) 231.

14. *Magnetocaloric effect in fine magnetic particle systems*, R D Shull, R D McMichael, L J Swartzendruber, L H Bennet North Holland Publ. Co. (Amsterdam) (1992) Chapter 16.*Magnetic properties of fine particles*, J. L. Dormann, D. Fiorani, North Holland Publ. Co. (Amsterdam) (1992) 161.

Chapter 8

Conclusion

The salient results of this investigation and the scope for further work is spelt out in this chapter...

The birth of nanoscience augurs very well for material science. This brand new discipline is all set to integrate various other disciplines of science particularly physics, chemistry, biology and material science. With the advent of nanoscience and nanotechnology the thin barrier between these disciplines is slowly melting in to thin air resulting in a synergy. This synergy is a real boost to material science and hence this journey of science to make life more humane is an eternal process. Every researcher aspires to contribute to his/her might to this noble cause and thus enable himself to serve humanity at large. This work carried out in the frontier area of nanoscience and nanotechnology has also been carried out with the primary motive of contributing my might to the cause of science at large. In the course of these investigations some of the objectives were intended and could be realized. However there were lacunae and much more needs to be carried out. This is being spelt out in this chapter along with the conclusions drawn out of these investigations on nanocrystalline magnetic materials.

Any investigation in the realm of material science necessitates that the materials are synthesized appropriately using simple techniques which can be carried out an ordinary physics laboratory. This is considered a prerequisite because the history of the sample preparation is very crucial for the proper interpretation of the results. Phase pure nanocrystalline samples are often difficult to synthesize and hence the preparative conditions have to be worked out by trial and error. The focal theme of this particular thesis was on nanocrystalline ferrites and passivated metal nanoparticles. Conventional ceramic techniques for the preparation of ferrites are well known. However preparation of nanocrystalline ferrites demands new techniques using cold precipitation or sol-gel. Phase pure nanocrystalline mixed ferrites belonging to the series $Mn_{1-x}Zn_xFe_2O_4$ could easily be synthesized using the method of   co-precipitation. The preparative conditions were optimized and standardized with precise control over stoichiometry. The size of the particle could also be controlled to a certain extent. The size of the particles lie in the range 7-29nm. This technique produced good yield and ensured

complete homogenity. Hence this process could be scaled up for bulk synthesis. Ferrofluids based on manganese zinc mixed ferrites could be synthesized by a modified process mentioned above. The advantage of employing this method for the preparation of mixed ferrite manganese zinc ferrite is that the magnetic property of the ferrofluid can be tuned by varrying the concentration of zinc or size of the particles. This is quite promising because ferrofluids based on manganese zinc ferrite nanoparticles can be quite useful as nanofluids for various mechanical engineering applications. Non linear optical properties of ferrofluids based on manganese zinc ferrites could be useful for optical limiting applications.

The method of sol-gel was utilized to synthesize nanosized cobalt ferrite. This method also yielded phase pure pristine nanoparticles of $CoFe_2O_4$. The conditions were optimised and standardized. Preparation of metallic nanostructures based on 3d transition metals like Ni/Fe/Co is quite challenging. Because at nanodimensions, metallic nanoparticles of iron and nickel are prone to oxidation and become useless as magnetic materials. Hence new synthesis techniques by novel template assisted method have to be adopted. A new method involving polystyyrene matrices and ion exchange reduction to synthesize passivated nanoparticles was worked out. The total magnetisaton of the composites could be controlled by cycling the processs of reduction, there by increasing the concentration of Ni/Fe nanoparticles in the matrix. If this method can be suitably modified and reaction carried out insitu on a polymer film, nanostructured metallic thin films could easily be prepared. This might have wide ranging applications in the form of sensors.

Structural studies carried out on $Mn_{1-x}Zn_xFe_2O_4$ reveal them to be phase pure. The magnetization measurements revealed that they become superparamagnetic for compositions greater than x = 0.2. The critical ordering temperatures (T_c) at which these materials transform into paramagnetic phase also differ substantially with respect to their bulk counter parts. The structural studies also revealed that these compositons exhibit a metastable cation distribution

totally different from their micronsized cousins. However this inference is only tentative. An elaborate investigation employing Mossbauer spectroscopy and neutron scattering is necessary for arriving at a definite conclusion.The role of Mn^{2+}/Mn^{3+} in these compostions is also a matter of uncertainty because the valence state of Mn is to be ascertained by techniques like X-ray photoelectron spectroscopy (XPS). This could not be carried out in this investigation. So there is further room for investigation in the compositions to ascertain the occupancy of these cations *vis a vis* the octahedral or the tetrahedral sites. Such a study will enable to establish the cation distribution and thus correlate the observed magnetic properties. These investigations could not be conducted for lack of time and availability of instruments.

The electrical properties of nanocrystalline ferrites assume significance because in a series like $Mn_{1-x}Zn_xFe_2O_4$, and if the electrical properties can be tuned by varying x, a wide variety of applications based on these materials can thus be envisaged. A study on the dc, ac and dielectric properties over a wide range of radio frequencies revealed interesting observations. It was found that the electrical properties of these nanocrystalline ferrites were quite different when compared to their micron sized counterpart. It was also found that there occurred dielectric dispersion in the lower frequency regime and the dielectric permittivity decreased with the increase in zinc concentration. Strong dielectric relaxations were also exhibited by manganese rich compositions. In order to elucidate the mechanism of conduction in these nanocrystalline ferrites, Cole –Cole analysis were simultaneously carried out. The Cole-Cole analysis resulted in the estimation of the limiting values of permittivity (ϵ_0 and ϵ_α) and the dispersion parameters. The activation energy values calculated from different electrical properties suggested a polaron based conduction in these ferrites. Overlapping polaron conduction was observed in manganese rich compositions and small polaron hopping in the zinc rich compositions. In the case of zinc ferrite, where there is minimum number of hopping pairs, we observed a correlated barrier hopping

conduction. The presence of localized electrons and Jahn-Teller ions like Mn^{3+} contribute to the polaron to the polaron assisted conduction process.

Though a mechanism for ac and dc conduction could be proposed based on polaron hopping ,further studies on these compositions would shed more light on the nature of the mechanism at or near critical temperatures namely T_C (curie temperature) or T_B (blocking temperature). Furthermore, these studies could be extended to the microwave frequency regime. The dielectric permittivity as well as the magnetic permeability of these compositions over a wide range of temperature and frequency are of interest from an application point of view since manganese zinc ferrite are components of various devices for low frequency applications. Further, if impedance spectroscopy experiments can be carried out on these compositions, definite conclusions based on the grain-grain boundary characteristics of these materials could be brought out. This is very essential since these materials crystallize in the nanostructured form. These could be carried as an extension of this work. Cobalt ferrite nanoparticles are found to exhibit interesting magnetic properties on account of their high magnetocrystalline anisotropy. In the nanoregime, the anisotropy in cobalt ferrite is an interesting property which can be controlled by varying the size, shape and distribution of the nanosystem. Ferrofluids based on these ferrites are being investigated because they are biocompatible like magnetite based Ferrofluids. The electrical properties of cobalt ferrite also confirmed a polaron conduction assisted process in nanocrystalline cobalt ferrite.

Experiments carried out on nanocomposites based on iron/nickel revealed that both weakly acidic cation exchange resin (WAC) and strongly acidic cation exchange resin (SAC) can be employed to synthesize these composites. The magnetic properties of the composite could be tuned by embedding the right amount of nickel/iron in the matrix. Composites prepared by weakly acidic cation exchange resin and strongly acidic cation exchange resin behaved quite differently. Cycling of the reduction process did not allow the particle to grow

197

and at the same time contributed to the total magnetization. The synthesis techniques can be optimized for different preparative conditions to tune its properties. A detailed magnetic characterisation using FC-ZFC measurements can provide a clear picture of the different matrix – particle, particle- particle interactions in the interfaces of these nanocomposites. Ferrofluid can be prepared based on these nanocomposites for possible applications. The optical and electrical properties of these nanocomposites are likely to be interesting.

Nanocrystalline materials exhibit altogether different critical phenomenon when their size is reduced. So the magnetocaloric properties of these materials are important. The isothermal magnetic entropy change, ΔS_m was estimated from magnetization isotherms for representative samples of cobalt ferrite and Nickel polystyrene (SAC-Ni) nanocomposites .It was found that nanocrystalline cobalt ferrite exhibited an inverse MCE with reasonably large values of ΔS_m. Nanocomposites based on nickel also showed reasonable ΔS_m .Initial investigations reveal that this nanocrystalline materials could be used as magnetic refrigerant for specific applications. For this the critical temperature namely T_B/T_c as the case may be must be tuned either by reducing the size or by manipulating the composition. Such an experiment will be a futuristic proposition and which can be pursued in the near future.

This thesis is a small drop in the large ocean of science. My contribution through this investigation may be considered as a small drop in the large ocean of science, however as the adage goes "little drops of water makes a mighty ocean", my humble efforts towards this endeavour is a very much 'nano' in the realm of 'giga' nanoscience.

Journal Papers

1. Evidence for polaron conduction in nanostructured manganese ferrite; **E Veena Gopalan**, K A Malini, S Saravanan, D Sakthi Kumar, Yasuhiko Yoshida, and M R Anantharaman, J. Phys. D: Appl. Phys. 41(2008), 185005.

2. Impact of zinc substitution on the structural and magnetic properties of chemically derived nanosized manganese zinc mixed ferrites; Journal of Magnetism and Magnetic Materials; **E Veena Gopalan**, I.A.Al-Omari K A Malini, D Sakthi Kumar, Yasuhiko Yoshida, P.A.Joy and M R Anantharaman , 321(2009) 1092.

3. On the dielectric dispersion and absorption in nanosized Manganese Zinc Mixed ferrites; **E Veena Gopalan**, K A Malini, S Saravanan, D Sakthi Kumar, Yasuhiko Yoshida, I.A.Al-Omari and M R Anantharaman, Journal of Physics : Condens. Matter, 21 (2009) 146006

4. On the Structural, Magnetic and Electrical properties of Sol-gel Derived Nanosized Cobalt ferrite. **E. Veena Gopalan**, I. A. Al-Omari D Sakthi Kumar, Yasuhiko Yoshida, P.A.Joy and M R Anantharaman ,Journal of Alloys and Compounds (accepted June 2009)

5. Elucidation of the Mechanism of ac Conduction in Nanostructured Manganese Zinc Mixed Ferrites. **E Veena Gopalan**. *et. al.* (Under review in Journal of Physics: D)

6. Template assisted synthesis of passivated nickel nanoparticles: their structural and magnetic properties. **E. Veena Gopalan** *et. al.* (Under review in Nanoscale, Royal Society of Chemistry)

7. Inverse magnetocaloric effect in cobalt ferrite nanoparticles: **E. Veena Gopalan** *et. al.* (Under review in J. Magn. Mag. Mater.)

8. Effect of zinc substitution on the dc conductivity behaviour of Nanostructured Manganese Zinc Mixed Ferrites . **E. Veena Gopalan** *et. al.* (Ready for communication).

9. Synthesis and characterisation of Fe nanoparticles embedded in Polystyrene Resinous Beads **E. Veena Gopalan** *et. al.* (Ready for communication).

10. Magnetocaloric properties of Iron-polystyrene nanocomposites **E. Veena Gopalan** *et. al.* (Ready for communication).

Conference Papers

1. Synthesis and structural properties of nanocomposites containing elemental nickel. **E Veena Gopalan**, K A Malini and M R Anantharaman, International conference on materials for the millennium (MatCon 2007), March 1st-3rd 2007, CUSAT, Kochi, India.

2. Structural and dielectric properties of co-precipitated manganese ferrite nanoparticles. **E. Veena Gopalan**, K A Malini, D Sakthi Kumar, Yasuhiko Yoshida and M R Anantharaman, International Conference on Smart Electroceramics (NCSE), 8th - 9th March, 2007, Thrissur, Kerala, India.

3. Anomalous magnetic behaviour in sol-gel synthesized zinc ferrite nanopowders, **E Veena Gopalan**, K A Malini, P A Joy and M R Anantharaman National Conference on Current Trends in Materials Science (CTMS-07) March 25th - 27th 2007, Chengannur, Kerala, India. **(Oral presentation)**

4. Magnetocaloric Measurements in Nanosized Cobalt Ferrite, Second International **E Veena Gopalan** K A Malini, I.A.Al-Omari and M R Anantharaman Conference on Frontiers in Nanotechnology and Nanoscience,(COCHIN NANO-2009),Cochin, India, January 3rd-6th, 2009 (*Won the Best poster award*)